



HAL
open science

Final Moments II: Observational Properties and Physical Modeling of CSM-Interacting Type II Supernovae

W.V Jacobson-Galán, L Dessart, K.W Davis, C.D Kilpatrick, R Margutti, R.J Foley, R Chornock, G Terreran, D Hiramatsu, M Newsome, et al.

► **To cite this version:**

W.V Jacobson-Galán, L Dessart, K.W Davis, C.D Kilpatrick, R Margutti, et al.. Final Moments II: Observational Properties and Physical Modeling of CSM-Interacting Type II Supernovae. The Astrophysical Journal, 2024, 970 (2), pp.189. 10.3847/1538-4357/ad4a2a . hal-04531972

HAL Id: hal-04531972

<https://hal.science/hal-04531972v1>

Submitted on 28 Oct 2024

HAL is a multi-disciplinary open access archive for the deposit and dissemination of scientific research documents, whether they are published or not. The documents may come from teaching and research institutions in France or abroad, or from public or private research centers.

L'archive ouverte pluridisciplinaire **HAL**, est destinée au dépôt et à la diffusion de documents scientifiques de niveau recherche, publiés ou non, émanant des établissements d'enseignement et de recherche français ou étrangers, des laboratoires publics ou privés.



Distributed under a Creative Commons Attribution 4.0 International License



Final Moments. II. Observational Properties and Physical Modeling of Circumstellar-material-interacting Type II Supernovae

W. V. Jacobson-Galán¹ , L. Dessart² , K. W. Davis³ , C. D. Kilpatrick^{4,5} , R. Margutti^{1,6} , R. J. Foley³ , R. Chornock¹ , G. Terreran⁷ , D. Hiramatsu^{8,9} , M. Newsome^{7,10} , E. Padilla Gonzalez^{7,10} , C. Pellegrino¹¹ , D. A. Howell^{7,10} , A. V. Filippenko¹ , J. P. Anderson^{12,13} , C. R. Angus^{14,15} , K. Auchettl^{3,16} , K. A. Bostroem^{17,38} , T. G. Brink¹ , R. Cartier¹⁸ , D. A. Coulter¹⁹ , T. de Boer²⁰ , M. R. Drout²¹ , N. Earl²² , K. Ertini^{23,24} , J. R. Farah^{7,10} , D. Farias¹⁴ , C. Gall¹⁴ , H. Gao²⁰ , M. A. Gerlach²⁵ , F. Guo²⁶ , A. Haynie^{27,28} , G. Hosseinzadeh¹⁷ , A. L. Ibik²¹ , S. W. Jha²⁹ , D. O. Jones³⁰ , D. Langeroodi¹⁴ , N. LeBaron¹ , E. A. Magnier²⁰ , A. L. Piro²⁷ , S. I. Raimundo^{14,31} , A. Rest^{19,32} , S. Rest³² , R. Michael Rich³³ , C. Rojas-Bravo³ , H. Sears^{4,5} , K. Taggart³ , V. A. Villar⁸ , R. J. Wainscoat²⁰ , X-F. Wang²⁶ , A. R. Wasserman^{34,35} , S. Yan²⁶ , Y. Yang¹ , J. Zhang^{36,37} , and W. Zheng¹

¹ Department of Astronomy, University of California, Berkeley, CA 94720-3411, USA; wynnjg@berkeley.edu

² Institut d'Astrophysique de Paris, CNRS-Sorbonne Université, 98 bis boulevard Arago, F-75014 Paris, France

³ Department of Astronomy and Astrophysics, University of California, Santa Cruz, CA 95064, USA

⁴ Center for Interdisciplinary Exploration and Research in Astrophysics (CIERA), Northwestern University, Evanston, IL 60202, USA

⁵ Department of Physics and Astronomy, Northwestern University, Evanston, IL 60208, USA

⁶ Department of Physics, University of California, Berkeley, CA 94720-7300, USA

⁷ Las Cumbres Observatory, 6740 Cortona Drive Suite 102, Goleta, CA 93117, USA

⁸ Center for Astrophysics | Harvard & Smithsonian, 60 Garden Street, Cambridge, MA 02138-1516, USA

⁹ The NSF AI Institute for Artificial Intelligence and Fundamental Interactions, USA

¹⁰ Department of Physics, University of California, Santa Barbara, Santa Barbara, CA, 93111, USA

¹¹ Department of Astronomy, University of Virginia, Charlottesville, VA 22904, USA

¹² European Southern Observatory, Alonso de Córdova 3107, Casilla 19, Santiago, Chile

¹³ Millennium Institute of Astrophysics MAS, Nuncio Monsenor Sotero Sanz 100, Off. 104, Providencia, Santiago, Chile

¹⁴ DARK, Niels Bohr Institute, University of Copenhagen, Jagtvej 128, 2200 Copenhagen, Denmark

¹⁵ Astrophysics Research Centre, School of Mathematics and Physics, Queen's University Belfast, Belfast BT7 1NN, UK

¹⁶ School of Physics, The University of Melbourne, VIC 3010, Australia

¹⁷ Steward Observatory, University of Arizona, 933 North Cherry Avenue, Tucson, AZ 85721-0065, USA

¹⁸ Gemini Observatory, NSF's National Optical-Infrared Astronomy Research Laboratory, Casilla 603, La Serena, Chile

¹⁹ Space Telescope Science Institute, Baltimore, MD 21218, USA

²⁰ Institute for Astronomy, University of Hawaii, 2680 Woodlawn Drive, Honolulu, HI 96822, USA

²¹ David A. Dunlap Department of Astronomy and Astrophysics, University of Toronto, 50 St. George Street, Toronto, Ontario, M5S 3H4, Canada

²² Department of Astronomy, University of Illinois at Urbana-Champaign, 1002 W. Green Street, Urbana, IL 61801, USA

²³ Facultad de Ciencias Astronómicas y Geofísicas, Universidad Nacional de La Plata, Paseo del Bosque S/N, B1900FWA, La Plata, Argentina

²⁴ Instituto de Astrofísica de La Plata (IALP), CCT-CONICET-UNLP, Paseo del Bosque S/N, B1900FWA, La Plata, Argentina

²⁵ Department of Astrophysics, Pontificia Universidad Católica de Chile, Santiago, Chile

²⁶ Department of Physics, Tsinghua University, Shuangqing Road, Beijing, People's Republic of China

²⁷ The Observatories of the Carnegie Institute for Science, 813 Santa Barbara Street, Pasadena, CA 91101, USA

²⁸ Department of Physics & Astronomy, University of Southern California, Los Angeles, CA 90089, USA

²⁹ Department of Physics and Astronomy, Rutgers, the State University of New Jersey, 136 Frelinghuysen Road, Piscataway, NJ 08854, USA

³⁰ Institute for Astronomy, University of Hawai'i, 640 N. A'ohoku Pl., Hilo, HI 96720, USA

³¹ Department of Physics and Astronomy, University of Southampton, Highfield, Southampton SO17 1BJ, UK

³² Department of Physics and Astronomy, The Johns Hopkins University, Baltimore, MD 21218, USA

³³ Department Physics and Astronomy, University of California, Los Angeles, Los Angeles, CA 90095-1547, USA

³⁴ Department of Astronomy, University of Illinois at Urbana-Champaign, 1002 W. Green Street, IL 61801, USA

³⁵ Center for Astrophysical Surveys, National Center for Supercomputing Applications, Urbana, IL 61801, USA

³⁶ Yunnan Observatories (YNAO), Chinese Academy of Sciences, Kunming 650216, People's Republic of China

³⁷ Key Laboratory for the Structure and Evolution of Celestial Objects, CAS, Kunming, 650216, People's Republic of China

Received 2024 March 4; revised 2024 April 22; accepted 2024 April 25; published 2024 July 31

Abstract

We present ultraviolet/optical/near-infrared observations and modeling of Type II supernovae (SNe II) whose early time ($\delta t < 2$ days) spectra show transient, narrow emission lines from shock ionization of confined ($r < 10^{15}$ cm) circumstellar material (CSM). The observed electron-scattering broadened line profiles (i.e., IIn-like) of H I, He I/II, C IV, and N III/IV/V from the CSM persist on a characteristic timescale (t_{In}) that marks a transition to a lower-density CSM and the emergence of Doppler-broadened features from the fast-moving SN ejecta. Our sample, the largest to date, consists of 39 SNe with early time IIn-like features in addition to 35 “comparison” SNe with no evidence of early time IIn-like features, all with ultraviolet observations. The total sample includes 50 unpublished objects with a total of 474 previously unpublished spectra and 50 multiband light curves, collected

³⁸ LSST-DA Catalyst Fellow.

primarily through the Young Supernova Experiment and Global Supernova Project collaborations. For all sample objects, we find a significant correlation between peak ultraviolet brightness and both t_{In} and the rise time, as well as evidence for enhanced peak luminosities in SNe II with IIn-like features. We quantify mass-loss rates and CSM density for the sample through the matching of peak multiband absolute magnitudes, rise times, t_{In} , and optical SN spectra with a grid of radiation hydrodynamics and non-local thermodynamic equilibrium radiative-transfer simulations. For our grid of models, all with the same underlying explosion, there is a trend between the duration of the electron-scattering broadened line profiles and inferred mass-loss rate: $t_{\text{In}} \approx 3.8[\dot{M}/(0.01 M_{\odot} \text{ yr}^{-1})]$ days.

Unified Astronomy Thesaurus concepts: Type II supernovae (1731); Shocks (2086); Circumstellar gas (238); Ultraviolet astronomy (1736)

Materials only available in the online version of record: machine-readable table

1. Introduction

The shock breakout (SBO) from a red supergiant (RSG) premieres as a burst of luminous ultraviolet (UV) and X-ray radiation that lasts several hours (Waxman & Katz 2017; Goldberg et al. 2022). The breakout photons escape from a characteristic optical depth ($\tau \approx c/v_{\text{sh}}$, where c is the speed of light, and v_{sh} is the shock velocity), which could occur either in the outer RSG envelope or inside of high-density circumstellar material (CSM) surrounding the star at the time of first light (Chevalier & Irwin 2011; Haynie & Piro 2021). Following first light at the characteristic optical depth, the photons emitted at SBO will “flash ionize” the CSM, leading to narrow emission lines in the early time spectra of highly ionized elements such as He II, C IV, O VI, and N III/IV/V. However, without the presence of a continuous ionizing source in the CSM after SBO, the CSM will quickly recombine, and the “flash ionization” phase will conclude within minutes to hours after SBO ($t_{\text{rec}} \propto 1/n_e$, where n_e is number density of free electrons) given the densities typical of RSG environments (e.g., $n \approx 10^7\text{--}10^{10} \text{ cm}^{-3}$, $\rho \approx 10^{-14} - 10^{-17} \text{ g cm}^{-3}$ at $r < 2R_{\star}$).

For Type II supernovae (SNe II) propagating in a low-density environment ($\rho < 10^{-15} \text{ g cm}^{-3}$ at $r \approx 10^{14\text{--}15} \text{ cm}$), the fast-moving SN ejecta will then sweep up low-density, optically thin CSM, and the Doppler-broadened spectral features of SN ejecta will be visible within hours to days after first light. For higher densities associated with some SN II environments (e.g., $\rho \gtrsim 10^{-14} \text{ g cm}^{-3}$), radiative cooling of the shocked regions will result in the formation of a cold dense shell (CDS) even at early times (Chevalier & Fransson 1994; Fransson 2017). Consequently, SNe II in dense CSM ($\rho \gtrsim 10^{-14} \text{ g cm}^{-3}$ at $r \approx 10^{14\text{--}15} \text{ cm}$) present a unique opportunity to probe more extreme RSG mass-loss histories through ultrarapid (“flash”) spectroscopy during the explosion’s first days (Gal-Yam et al. 2014; Khazov et al. 2016; Yaron et al. 2017; Terreran et al. 2022; Jacobson-Galán et al. 2023).

Following SN ejecta–CSM interaction, the forward-shock kinetic luminosity goes as $L_{\text{sh}} = \dot{M}v_{\text{sh}}^3/2v_w$, where v_{sh} is the shock velocity, v_w is the wind velocity, and \dot{M} is the mass-loss rate (e.g., $\dot{M} = 4\pi\rho r^2v_w$). Consequently, in high-density CSM, the SN shock power is quite high ($>10^{41} \text{ erg s}^{-1}$ for $\dot{M} > 10^{-4} M_{\odot} \text{ yr}^{-1}$, $v_{\text{sh}} \approx 10^4 \text{ km s}^{-1}$), and for typical postshock temperatures ($T_{\text{sh}} \approx 10^{5\text{--}8} \text{ K}$), the gas will cool primarily via free–free emission, as well as line emission (Fransson 2017). High-energy photons emitted at the shock front will continue to ionize the intervening CSM, prolonging the formation of high-ionization recombination lines present during the “flash ionization” phase. During this “photoionization” phase, recombination photons inside the CSM will encounter a large number density of free electrons and consequently participate in multiple scatterings before they exit the

CSM. Observationally, this manifests as spectral line profiles that contain a combination of a narrow core and Lorentzian wings (i.e., IIn-like), the former tracing the expansion velocities in the wind/CSM while the latter results from the photon’s frequency shift following electron scattering (Chugai 2001; Dessart et al. 2009; Huang & Chevalier 2018). In the single-scattering limit, the observed emission line will map the thermal velocity of the free electrons ($v_e \approx 10^3(T/10^{4.5} \text{ K})^{1/2} \text{ km s}^{-1}$), but with sufficiently large electron-scattering optical depths ($\tau \approx 3\text{--}10$), the resulting line profiles can extend to thousands of kilometers per second. However, as the shock samples lower-density CSM at large radii (assuming a wind-like profile or CSM shell), these electron-scattering profiles will vanish within days to weeks of first light, with the SN photosphere then revealing the CDS, if present, and subsequently the fast-moving SN ejecta (Dessart et al. 2017). However, departures from CSM spherical symmetry and/or homogeneous density may blur the transition between these three phases; for example, Doppler-broadened line profiles can appear while spectral signatures of unshocked optically thick CSM are still present in the early time spectra.

Given the transient nature of these spectral features, high-cadence “flash” spectroscopy during the first days post-SBO is essential to map the densities, kinematics, and progenitor chemical composition in the preexplosion environment at radii of $r < 10^{15} \text{ cm}$. Consequently, such observations provide a window into the largely unconstrained stages of stellar evolution in the final years to months before core collapse. Enabled by the advent of high-cadence surveys in the past decade, the study of SNe II with such photoionization spectral features has revealed enhanced, late-stage mass-loss rates in RSG progenitor systems. Interestingly, one of the first records of this phenomenon was in SN 1983K (Niemela et al. 1985), but garnered the most attention through observations of SN 1998S (Fassia et al. 2000; Leonard et al. 2000), which showed high-ionization features at early times ($\delta t < 7$ days) and then transitioned to a Type IIL supernova (SN IIL) at later phases ($\delta t > 7$ days) as the IIn-like features disappeared. Spectroscopic and photometric modeling of SN 1998S suggested significant mass loss of $\dot{M} \approx 10^{-2} M_{\odot} \text{ yr}^{-1}$ for $v_w \approx 50\text{--}100 \text{ km s}^{-1}$ (Shivvers et al. 2015; Dessart et al. 2016), capable of producing transient IIn-like features and an overluminous light curve, placing it as extreme compared to normal SNe II, but not quite placing it in the Type IIn SN subclass.

Since SN 1998S, a number of SNe II have been discovered with photoionization spectral features from SN ejecta–CSM interaction at early times. Modeling of the photoionized spectra continues to point toward confined ($r < 10^{15} \text{ cm}$), high-density ($\dot{M} \approx 10^{-3}\text{--}10^{-2} M_{\odot} \text{ yr}^{-1}$, $v_w \approx 50\text{--}100 \text{ km s}^{-1}$) CSM created in the final years before explosion (e.g., PTF11iqb, Smith et al. 2015;

SN 2013fs, Yaron et al. 2017; Dessart et al. 2017; SN 2014G, Terreran et al. 2016; SN 2016bkv, Hosseinzadeh et al. 2018; Nakaoka et al. 2018; SN 2017ahn, Tartaglia et al. 2021; SN 2018zd, Zhang et al. 2020; Hiramatsu et al. 2021; SN 2020pni, Terreran et al. 2022; SN 2020tlf, Jacobson-Galán et al. 2022; SN 2023ixf, Jacobson-Galán et al. 2023; Bostroem et al. 2023; Smith et al. 2023; Zimmerman et al. 2024; Figure 11 of Brethauer et al. 2022). Sample studies have sought to uncover the rates of such events, the most recent estimate being $>40\%$ for all SN II discovered within 2 days of first light (Bruch et al. 2021b, 2023). Intriguingly, mass-loss rates derived for individual explosions stand in contradiction with observations of weak, steady-state mass loss (e.g., $10^{-6} M_{\odot} \text{yr}^{-1}$) in observed RSGs (Beasor et al. 2020) as well as the quiescent behavior of SN II progenitor stars in preexplosion imaging (Kochanek et al. 2017). However, this could be related to the preexplosion timescales that each method is probing. Furthermore, beyond H-rich SNe, “flash spectroscopy” has aided in significant breakthroughs in our understanding of H-poor SN progenitor identity and late-stage evolution, e.g., Type IIb, Type Ibc, and calcium rich (e.g., Gal-Yam et al. 2014; Pastorello et al. 2015; Jacobson-Galán et al. 2020; Chugai 2022; Davis et al. 2023; Wang et al. 2024). However, it is also evident that some massive stars undergo enhanced mass loss even before their final years (e.g., $t \approx 10\text{--}1000$ yr), and therefore, X-ray/radio observations as well as long-term UV/optical monitoring are essential to reconstruct a more complete mass-loss history (e.g., Chevalier 1998; Fransson et al. 1996; Chevalier et al. 2006; Weiler et al. 2002; Wellons et al. 2012; Milisavljevic et al. 2015; Fransson 2017; Margutti et al. 2017; Brethauer et al. 2022; DeMarchi et al. 2022; Stroh et al. 2021; Dessart et al. 2023; Shahbandeh et al. 2023; Grefenstette et al. 2023; Berger et al. 2023; Panjkov et al. 2023).

In this study, we present observations and modeling of the largest sample to date of SNe II with early time ($\delta t < 2$ days) spectroscopic signatures of CSM interaction. This sample consists of 27 unpublished SNe with photoionization emission features, which includes 293 new spectra as well as 27 UV/optical/near-infrared (NIR) light curves. In Section 2, we define the sample and present the spectroscopic and photometric observations. Section 3 presents an analysis of the bolometric and multiband light curves as well as early time and photospheric-phase spectra. In Section 4, we present the HERACLES/CMFGEN model grid and the derived mass-loss rates and CSM densities based on model comparisons to the sample data. Our results are discussed in Section 5, and our conclusions are in Section 6.

All phases reported in this paper are with respect to the adopted time of first light (Table A1) and are in rest-frame days. The time of first light (δt) and its uncertainty are calculated from the average phase between the last deep nondetection and the first detection using forced photometry from the survey that initially imaged the SN (e.g., the Zwicky Transient Facility, hereafter ZTF; ATLAS; the Young Supernova Experiment, hereafter YSE; DLT40). However, we note that the first-light phase could be earlier in some instances given a shallow depth of the last nondetection limit. Furthermore, “first light” in this case only refers to when photons are first detected from the SN, which is unlikely to reflect the first emission from the explosion. When available for a given sample object, we adopt the time of first light reported in a previously published study and confirm that this phase is consistent with first detection and last nondetection using

forced photometry. When possible, we use redshift-independent host-galaxy distances and adopt standard Λ CDM cosmology ($H_0 = 70 \text{ km s}^{-1} \text{ Mpc}^{-1}$, $\Omega_M = 0.27$, $\Omega_{\Lambda} = 0.73$) if only redshift information is available for a given object.

2. Observations

2.1. Sample Definition

Our total sample consists of 74 SNe II, 39 of which show spectroscopic evidence for CSM interaction at early times ($\delta t < 10$ days) through the detection of transient IIn-like features. Gold-sample objects have a spectrum obtained at $\delta t < 2$ days while silver-sample objects only have spectra obtained at $\delta t > 2$ days. Additionally, we include 35 SNe II with “flash spectroscopy” (i.e., spectra at $\delta t < 2$ days) but no detection of IIn-like features (the comparison sample). For the gold and comparison samples, we require that the uncertainty in the time of first light be < 1 day. To construct the total sample, we first query the Transient Name Server (TNS)³⁹ for every transient discovered between 2004 November 20 and 2022 August 1 and then select only objects with Type II-like classification (e.g., SN II, SN IIP, SN IIL, SN IIn, SN II-pec) at redshifts $z < 0.05$, which returns 1697 SNe. For those SNe II, we keep objects having spectra within 3 days of discovery, which returns 428 objects. Next, we query the Swift Ultraviolet Optical Telescope (UVOT) data archive and record how many total observations of the SN location exist within 10 days of discovery. We then keep objects with > 2 Swift-UVOT observations at < 10 day postdiscovery, which returns 114 total objects, after cutting SNe IIn. This exercise is repeated using the Weizmann Interactive Supernova Data Repository (WiSeREP),⁴⁰ finding 48 total objects, both with and without IAU names, that meet the sample selection criteria listed above. We are then left with 137 total SNe II after removing duplicate objects. Lastly, we cut all SNe II with no IIn-like features that do not have a spectrum at $\delta t < 2$ days and/or uncertainty in the time of first light of > 1 day. Furthermore, we cut all objects that do not have $\Delta m > 1$ mag between last nondetection and first detection, in the same filter, and/or $\Delta M > 3$ mag between first detection and peak brightness. Consequently, our total sample contains 74 objects: 20 gold-, 19 silver-, and 35 comparison-sample SNe II. In this data release, we also include multicolor light curves and spectra of five additional SNe II with IIn-like features: 2018cvn, 2018khh, 2019ofc, 2019nyk, 2021ulv. These objects are not used in our analysis given the lack of UV photometry.

The gold/silver samples contain 12 previously published objects with a total of 208 spectra and 12 UV/optical light curves, in addition to 27 unpublished objects with a total of 293 spectra and 27 UV/optical light curves. The comparison sample contains 12 previously published and 23 unpublished objects, with a total of 464 spectra. As shown in Figure A5 in the Appendix, the peak absolute magnitude as a function of SN distance reveals a trend consistent with a Malmquist bias, i.e., only higher luminosity objects can be detected at farther distances. An examination of peak apparent magnitude before extinction corrections are applied shows that the sample extends to low luminosities, with the majority of nearby ($D < 20$ Mpc) events being in the comparison sample. The lack

³⁹ <https://www.wis-tns.org/>

⁴⁰ <https://www.wiserep.org/>

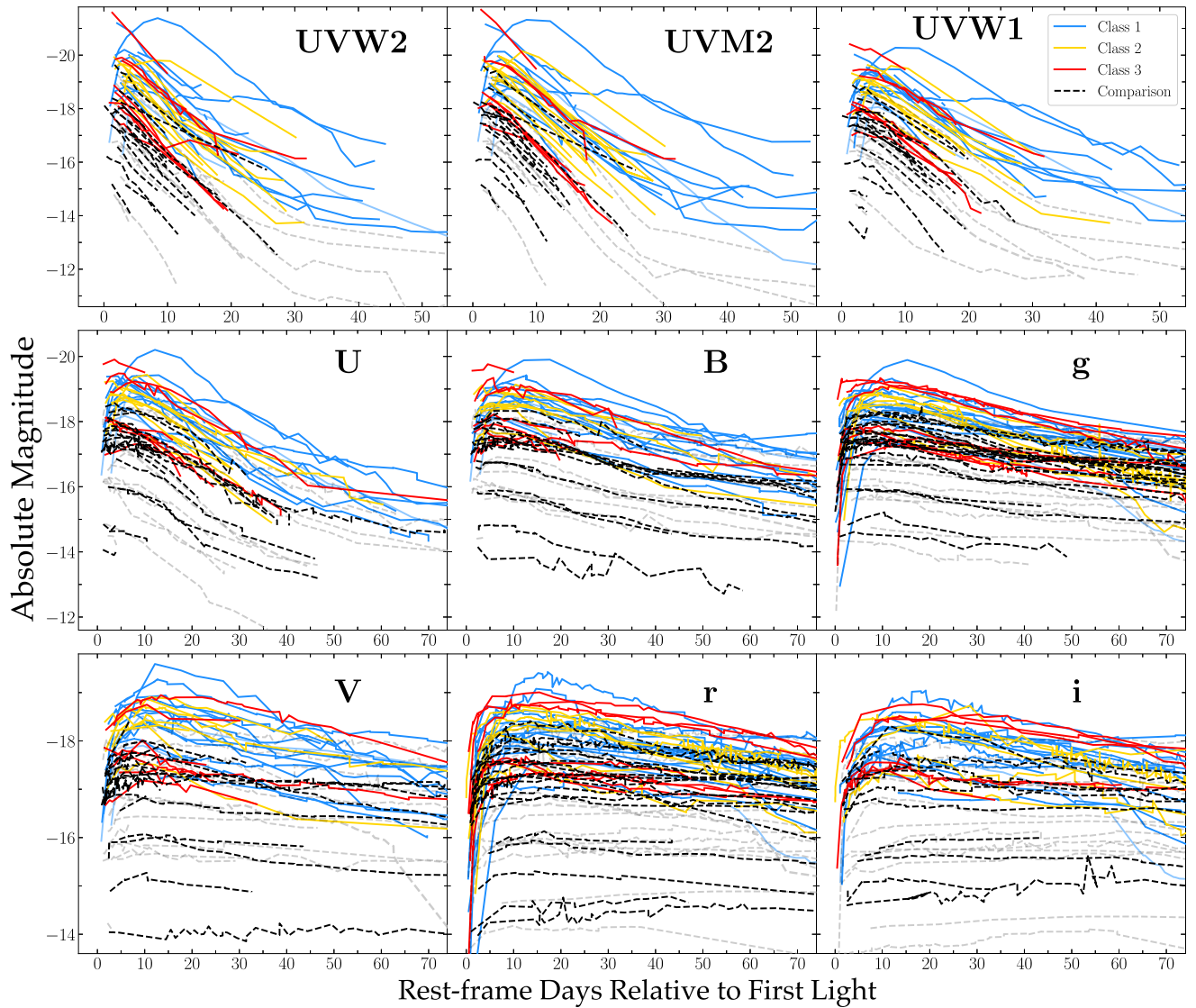


Figure 1. Left to right, top to bottom: Early time, extinction corrected $w2$ -, $m2$ -, $w1$ -, U/u -, B/b -, V/v -, g -, r -, and i -band light curves of SNe II with IIn-like profiles in their early spectra. No K-corrections have been applied. Gold and silver samples shown in blue, yellow, and red; comparison sample plotted as black dashed lines. Solid colored curves represent the subsample of objects at $D > 40$ Mpc. Compared to SNe II without IIn-like features (i.e., comparison sample), objects with confirmed IIn-like signatures have notably more luminous and longer-lasting UV emission at early times. Furthermore, Class 1 objects that show longer-lived IIn-like profiles of He II and N III are typically brighter than other gold-sample objects with shorter-lived IIn-like features. The variance of the total sample decreases with increasing wavelength, with the least luminous objects being those in the comparison sample.

of nearby gold/silver-sample objects may be the result of selection effects and/or the intrinsic rarity of SNe II with IIn-like features. Furthermore, the difference in redshift distribution (top left panel of Figure A5) implies that the gold and comparison samples may not arise from the same parent distribution. We account for this difference by applying a distance cut in our comparison of observables in each subsample in Section 3.1. Additionally, we note the lack of highly reddened SNe ($A_V > 3$ mag; Jencson et al. 2019) in our sample, which represents a selection effect in our sample because these objects are unlikely to have associated Swift-UVOT observations.

Within both subsamples, the color delineation (e.g., Figures 1 and 3) is as follows: at phases of $t \approx 2$ day post-first-light, blue-colored objects (“Class 1”) show high-ionization emission lines of N III, He II, and C IV (e.g., SNe 1998S, 2017ahn, 2018zd, 2020pni, 2020tlf), yellow-colored objects (“Class 2”) have no N III emission but do show He II and C IV

(e.g., SNe 2014G, 2022jox), and red-colored objects (“Class 3”) only show weaker, narrow He II emission superimposed with a blueshifted, Doppler-broadened He II (e.g., SN 2013fs, 2020xua). However, it should be noted that high-ionization lines of O V/VI, C V, and N IV are also present in SN 2013fs at $t < 1$ day owing to a more compact CSM than other CSM-interacting SNe II (Yaron et al. 2017; Dessart et al. 2017); thus, the color delineation is epoch dependent.

All targets were selected from private collaborations/surveys as well as all public/published studies on SNe II with prominent or potential IIn-like features in their early time spectra (Table A1). We emphasize that, while the SNe in our sample may show IIn-like line profiles at early times, they are not prototypical SNe IIn that show relatively narrow line profiles from CSM interaction for weeks to months following explosion (e.g., SNe 2005ip, 2010jl; Smith et al. 2009; Taddia et al. 2013; Gall et al. 2014; Fransson et al. 2014; Dessart et al. 2015). The IIn-like profiles in our sample objects fade within

days to a week after first light, and the explosion proceeds to evolve photometrically and spectroscopically as a standard RSG explosion—a light-curve plateau or linear (in magnitudes) decline where hydrogen recombination mitigates the release of stored radiative energy, and the photospheric spectra are dominated by P Cygni profiles formed from H, He, and Fe-group elements in the SN ejecta.

2.2. Photometric Observations

All gold-, silver-, and comparison-sample objects were observed during their evolution with UVOT (Romig et al. 2005) on board the Neil Gehrels Swift Observatory (Gehrels et al. 2004). We performed aperture photometry with a $5''$ region radius with `uvotsource` within HEASoft v6.26,⁴¹ following the standard guidelines from Brown et al. (2014).⁴² In order to remove contamination from the host galaxy, we employed images acquired at $\delta t > 1$ yr, assuming that the SN contribution is negligible at this phase. This is supported by visual inspection in which we found no flux at the SN location. We subtracted the measured count rate at the location of the SN from the count rates in the SN images and corrected for point-spread-function (PSF) losses following the prescriptions of Brown et al. (2014). We also note that the *w2* filter has a known red leak (Brown et al. 2010), which could impact postpeak observations when the SN is significantly cooler.

For the total sample, optical/NIR photometry was obtained from a variety of collaborations and telescopes. Pan-STARRS telescope (PS1/2; Kaiser et al. 2002; Chambers et al. 2017) imaging in the grizy bands was obtained through YSE (Jones et al. 2021). Data storage/visualization and follow-up coordination was done through the YSE-PZ web broker (Coulter et al. 2022, 2023). The YSE photometric pipeline is based on `photpipe` (Rest et al. 2005), which relies on calibrations from Magnier et al. (2020) and Waters et al. (2020). Each image template was taken from stacked PS1 exposures, with most of the input data from the PS1 3π survey. All images and templates were resampled and astrometrically aligned to match a skycell in the PS1 sky tessellation. An image zero-point is determined by comparing PSF photometry of the stars to updated stellar catalogs of PS1 observations (Flewelling et al. 2020). The PS1 templates are convolved with a three-Gaussian kernel to match the PSF of the nightly images, and the convolved templates are subtracted from the nightly images with `HOTPANTS` (Becker 2015). Finally, a flux-weighted centroid is found for the position of the SN in each image, and PSF photometry is performed using “forced photometry”: the centroid of the PSF is forced to be at the SN position. The nightly zero-point is applied to the photometry to determine the brightness of the SN for that epoch.

We obtained *uUBVgriz* imaging with the Las Cumbres Observatory (LCO) 1 m telescopes through the Global Supernova Project (GSP) and YSE. After downloading the BANZAI-reduced images from the LCO data archive (McCully et al. 2018), we used `photpipe` (Rest et al. 2005) to perform DoPhot PSF photometry (Schechter et al. 1993). All photometry was calibrated using PS1 stellar catalogs described above with additional transformations to the SDSS *u* band derived from Finkbeiner et al. (2016). For additional details on our reductions, see Kilpatrick & Foley (2018). We also

obtained photometry using a 0.7 m Thai Robotic Telescope at Sierra Remote Observatories and the 1 m Nickel telescope at Lick Observatory in the *BVRI* bands. Images are bias subtracted and field flattened. Absolute photometry is obtained using stars in the $10' \times 10'$ field of view. We also observed objects with the Lulin 1 m telescope in *griz* bands and the Swope 1 m telescope in *uBVgriz*. Standard calibrations for bias and flat-fielding were performed on the images using `IRAF`, and we reduced the calibrated frames in `photpipe` using the methods described above for the LCO images.

Sample objects were also observed with ATLAS, a twin 0.5 m telescope system installed on Haleakala and Maunaloa in the Hawai’ian islands that robotically surveys the sky in cyan (*c*) and orange (*o*) filters (Tonry et al. 2018a). The survey images are processed as described by Tonry et al. (2018a) and photometrically and astrometrically calibrated immediately (using the RefCat2 catalog; Tonry et al. 2018b). Template generation, image-subtraction procedures, and identification of transient objects are described by Smith et al. (2020). PSF photometry is carried out on the difference images, and all detections more significant than 5σ are recorded and go through an automatic validation process that removes spurious objects (Smith et al. 2020). Photometry on the difference images (both forced and nonforced) is obtained from an automated PSF fitting as documented by Tonry et al. (2018a). The photometry presented here is derived from the weighted averages of the nightly individual 30 s exposures, carried out with forced photometry at the position of each SN. In addition to our observations, we include *gri*-band photometry from ZTF (Bellm et al. 2019; Graham et al. 2019) forced-photometry service (Masci et al. 2019).

In Figure 2, we present new Transiting Exoplanet Survey Satellite (TESS; Ricker et al. 2015) light curves of SNe 2019nvm and 2021dbg, reduced using the `TESSreduce` package (Ridden-Harper et al. 2021), compared to the previously published TESS light curve of SN 2020fqv (Tinyanont et al. 2022). These observations have been binned to a 6 hr cadence and are able to constrain the uncertainty in the time of first light to a few hours. To our knowledge, SN 2021dbg represents the first SN II with IIn-like features to have a complete TESS light curve.

For all SNe, the Milky Way (MW) *V*-band extinction and color excess along the SN line of sight are inferred using a standard Fitzpatrick (1999) reddening law ($R_V = 3.1$). In addition to the MW color excess, we estimate the contribution of host-galaxy extinction in the local SN environment using NaID absorption lines for all gold-, silver-, and comparison-sample objects. To determine if NaID is detected, we fit the continuum in a region around the transition based on the spectral resolution and calculate the residuals between the continuum fit and the spectral data. We then integrate the residual flux and confirm that it is greater than or equal to 3 times the residual flux uncertainty in order to claim a “detection.” We calculate the NaID equivalent width (EW) and use $A_V^{\text{host}} = (0.78 \pm 0.15) \text{ mag} \times (\text{EW}_{\text{NaID}}/\text{\AA})$ from Stritzinger et al. (2018) to convert these EWs to an intrinsic host-galaxy $E(B - V)$, also using the Fitzpatrick (1999) reddening law. A visualization of this method is shown in Figure A2 in the Appendix. For nondetections, we calculate an upper limit on the EW and host reddening using the fitted continuum flux. We present a detailed discussion of the host-extinction uncertainties in Appendix A. We do not apply

⁴¹ We used the calibration database (CALDB) version 20201008.

⁴² https://github.com/gtterrera/Swift_host_subtraction

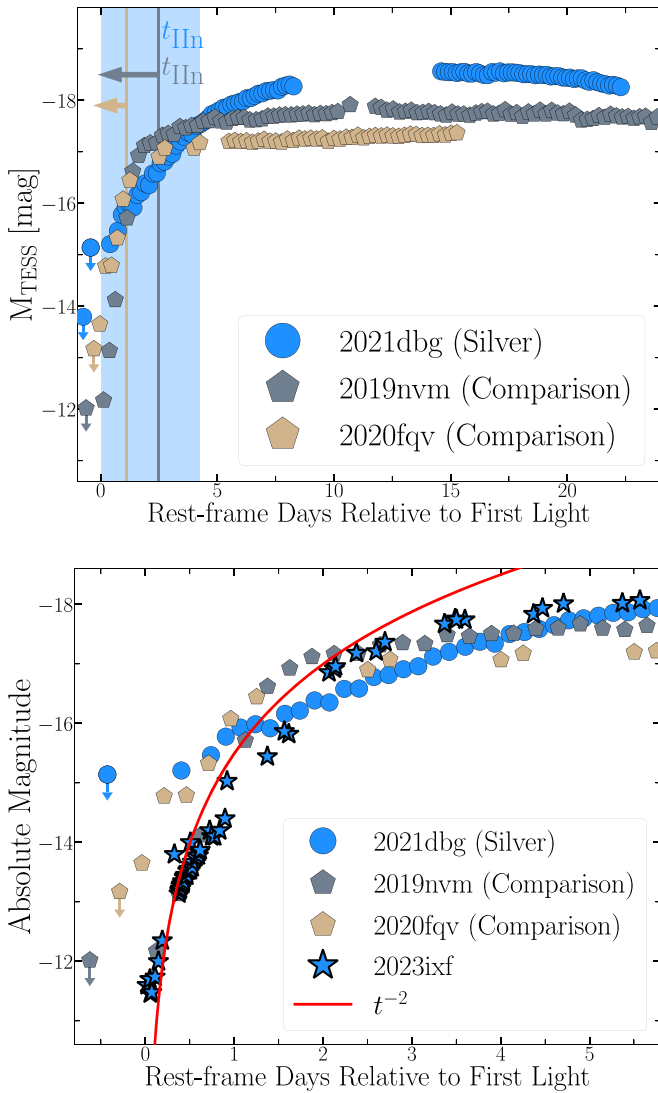


Figure 2. Top: TESS ($\lambda_{\text{eff}} = 7453 \text{ \AA}$) light curves (binned) for silver-sample object SN 2021dbg (blue circles) and comparison-sample objects SNe 2019nvm (gray polygons) and 2020fqv (tan polygons). SN 2021dbg shows IIn-like signatures for ~ 4 days after first light (blue shaded region), consistent with an increased rise time and peak absolute magnitude. Conversely, the persistence of IIn-like features in SNe 2019nvm and 2020fqv is constrained to < 2.6 and < 1.1 days, respectively. These SN light curves are likely consistent with shock-cooling emission from confined ($< 2R_s$), high-density stellar material and/or SN ejecta interaction with lower-density CSM that extends out to larger distances, neither scenario being able to form IIn-like features. Bottom: zoom-in of the first 5 days of the TESS light curves for SNe 2021dbg, 2020fqv, and 2019nvm compared to ground-based photometry in optical clear- and r -band filters of the nearby CSM-interacting SN II 2023ixf (Hosseinzadeh et al. 2023).

alternative methods for estimating the host extinction such as using the diffuse interstellar band at 5780 \AA (Phillips et al. 2013), which has been shown to yield consistent extinction values to Na I D EW for other SNe (Hosseinzadeh et al. 2022). We test whether the reddening values of the gold and comparison samples come from the sample parent distribution by applying a logrank test and finding a 35% chance probability that the gold- and comparison-sample reddening come from the same distribution. Therefore, there is no statistical evidence that the extinction correction affects the two subsamples differently and is thus not a source of differences between the luminosity distribution of each subsamples (see

Section 3.1). We present cumulative distributions of the gold-, silver-, and comparison-sample host extinction in Figure A2, and, in Appendix A, we discuss the use of colors as a metric for host-galaxy reddening.

All adopted extinction (MW and host), redshift, distance, and first-light date values are reported for gold-, silver-, and comparison-sample objects in Table A1. Complete, multiband light curves are shown in Figure 1. All photometric data and figures are publicly available in Zenodo doi:10.5281/zenodo.11154246. The same information is also available on GitHub.⁴³

2.3. Spectroscopic Observations

We obtained spectra for sample objects with the Kast spectrograph on the 3 m Shane telescope at Lick Observatory (Miller & Stone 1993) and Keck/LRIS (Oke et al. 1995). For all of these spectroscopic observations, standard CCD processing and spectrum extraction were accomplished with IRAF.⁴⁴ The data were extracted using the optimal algorithm of Horne (1986). Low-order polynomial fits to calibration-lamp spectra were used to establish the wavelength scale, and small adjustments derived from night-sky lines in the object frames were applied.

LCO optical spectra were taken with the FLOYDS spectrographs (Brown et al. 2013) mounted on the 2 m Faulkes Telescope North and South at Haleakala (USA) and Siding Spring (Australia), respectively, through the GSP. A $2''$ slit was placed on the target at the parallactic angle (Filippenko 1982). One-dimensional spectra were extracted, reduced, and calibrated following standard procedures using the FLOYDS pipeline⁴⁵ (Valenti et al. 2014).

Spectra were also obtained with the Alhambra Faint Object Spectrograph on The Nordic Optical Telescope, the Goodman spectrograph (Clemens et al. 2004) at the Southern Astrophysical Research (SOAR) telescope, Gemini Multi-Object Spectrographs, Wide-Field Spectrograph at Siding Spring, Binospec on the MMT (Fabricant et al. 2019), Lijiang 2.4 m telescope (+YFOSC; Fan et al. 2015), and SpeX (Rayner et al. 2003) at the NASA Infrared Telescope Facility. All of the spectra were reduced using standard techniques, which included correction for bias, overscan, and flat-field. Spectra of comparison lamps and standard stars acquired during the same night and with the same instrumental setting have been used for the wavelength and flux calibrations, respectively. When possible, we further removed the telluric bands using standard stars. Given the various instruments employed, the data-reduction steps described above have been applied using several instrument-specific routines. We used standard IRAF commands to extract all spectra.

Sample spectral data were also collected using EFOSC2 (Buzzoni et al. 1984) at the 3.58 m ESO New Technology Telescope through the ePESSTO+ program (Smartt et al. 2015). Standard data-reduction processes were performed using the PESSTO pipeline (Smartt et al. 2015).⁴⁶ The reduced spectrum was then extracted, and calibrated in wavelength and flux. In some instances, public classification spectra from TNS as well as published data stored in WISEREP were used in the presented sample. Early time spectra for the gold and silver samples are presented in Figure 3, with comparison-sample spectra shown in Figure A1 in the Appendix. In total, this study

⁴³ https://github.com/wynnjacobson-galan/Flash_Spectra_Sample

⁴⁴ https://github.com/msiebert1/UCSC_spectral_pipeline

⁴⁵ https://github.com/svalenti/FLOYDS_pipeline

⁴⁶ <https://github.com/svalenti/pessto>

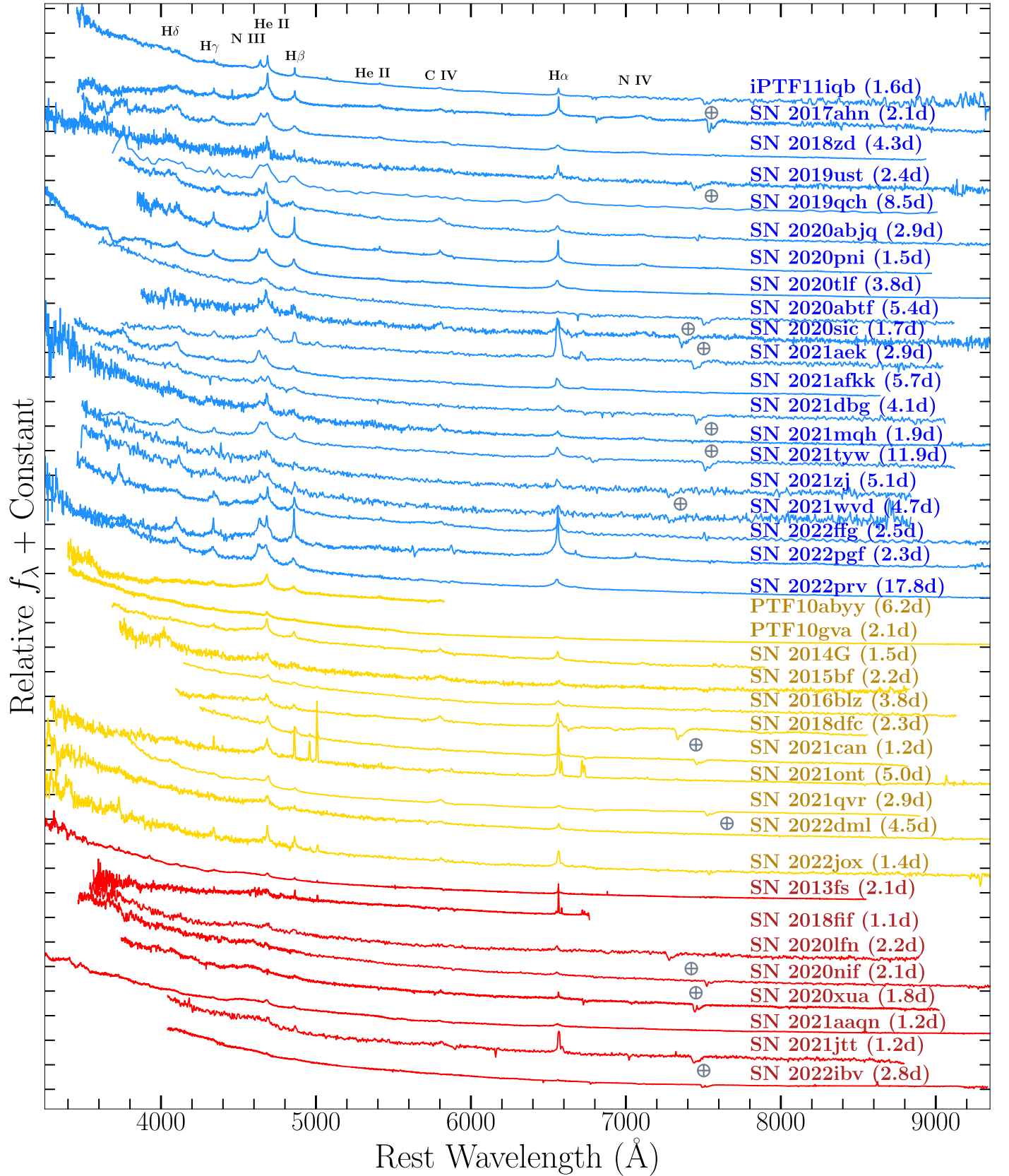


Figure 3. Early time ("flash") spectra of all gold- and silver-sample SNe II (e.g., Section 2.1); phases are relative to time of first light. All plotted SNe show transient, II-like (i.e., electron-scattering broadened) line profiles formed from persistent photoionization of dense, slow, unshocked CSM. Objects in blue ("Class 1") show prominent He II and N III emission, objects in yellow ("Class 2") exhibit only prominent He II emission, and objects in red ("Class 3") have weak He II emission. Gray circles with a plus indicate telluric absorption. We note that, because a number of spectra were obtained from public databases, there has not been a consistent flux calibration applied, and therefore, the relative continuum shapes should be interpreted with caution.

includes 491 published and 474 previously unpublished spectra of SNe II. All spectroscopic data/logs will be publicly available in an online data repository.⁴⁷

3. Analysis

3.1. Photometric Properties

We present extinction-corrected $w2$, $m2$, $w1$, u , b , v , g , r light curves of gold-, silver-, and comparison-sample objects in Figure 1. Given that the redshift/distance distributions of the gold and comparison samples are not the same, we divide sample objects based on a distance cut of $D > 40$ Mpc; this distance being the threshold when the distance distributions of both subsamples are consistent. In order to quantify the differences between the gold-sample classes and the comparison sample, we fit high-order polynomials to all light curves to derive a peak absolute magnitude and a rise time in all eight filters. These values are reported in Tables A3–A4, with the uncertainty in peak magnitude being the 1σ error from the fit, and the uncertainty in the peak phase being found from adding the uncertainties in both the time of peak magnitude and the time of first light in quadrature. We note that the prepeak evolution in the UV filters of some sample objects is unconstrained (e.g., Figure 1). For those objects with no constrained rise, we report the peak absolute magnitude and rise time as lower and upper limits, respectively.

As shown in Figure 4, we identify moderate positive trends between M_{peak} and t_{rise} in $w2$ -, $m2$ -, $w1$ -, u -band filters, and we find that, while such trends are not as significant in b , g , v , r filters, there is still a difference between gold/silver and comparison samples in optical filters. Among gold-sample SNe, Class 1 objects display the brightest peak absolute magnitudes and longest rise times compared to Class 3 and comparison-sample objects. On average, gold-sample objects are >2 mag brighter in the UV bands than comparison-sample objects (e.g., $M_{\text{avg}}^{w2} = -19.5$ mag versus $M_{\text{avg}}^{w2} = -17.1$ mag), even after a distance cut is applied, suggesting a significant luminosity boost from CSM interaction at early times. Furthermore, the $w2 - v$ and $g - r$ colors plotted in Figure 5 show that gold-sample objects, in particular Class 1 SNe, are bluer at earlier times than comparison-sample objects. Additionally, most Class 1/2 objects sustain blue colors ($g - r < 0$) longer than the comparison sample, suggesting continued interaction with more distant CSM that is at higher densities than a typical RSG wind. Similarly, the plateau luminosities of Class 1/2 objects remain higher than the control sample, also indicating long-lived interaction power.

In Figure 6, we present pseudobolometric UV/optical/NIR (UVOIR) light curves of the gold/silver- and comparison-sample objects generated using the `superbol`⁴⁸ code. For all SNe, we extrapolate between light-curve data points using a low-order polynomial spline in regions without complete color information. Repeating the analysis used for the multiband light curves, we calculate peak pseudobolometric luminosities and rise times; these values are presented in Table A3. For objects without a constrained rise to peak in all UV filters (i.e., $w2$, $m2$, $w1$), we report peak luminosities and rise times as lower and upper limits, respectively. As shown in Figure 6, we find a significant trend between peak UVOIR luminosities and

rise time to maximum light; this is similar to UV filters discussed above and indicates that the majority of the flux at early times is focused in the UV bands, especially with the presence of ejecta–CSM interaction. Furthermore, we find that gold/silver-sample objects can be more than 1 order of magnitude more luminous at peak than comparison-sample SNe (e.g., Table A5), also suggesting excess luminosity from CSM interaction.

In Figure 7, we present the cumulative distributions of maximum brightness and rise times for the pseudobolometric, $w2$ -band, and r -band light curves of the gold/silver and comparison samples that are constructed using Kaplan–Meier estimation for all objects at $D > 40$ Mpc. To test our null hypothesis of whether these sample observables come from the same parent distribution, we apply a logrank test for (i) gold versus comparison samples, (ii) gold-sample Classes 1 and 2 versus 3, and (iii) gold-sample Classes 1 versus 3. Limits on the peak luminosity and rise time are accounted for using survival statistics. For (i), the chance probability that peak-brightness values of the gold and comparison samples come from the same distribution is 0.1% for L_{max} , 80.0% for $M_{w2,\text{max}}$, and $3 \times 10^{-3}\%$ for $M_{r,\text{max}}$. We find that the pseudobolometric, UV, and r -band rise times between samples do belong to the same distribution at the 60.6%, 7.1%, and 55.6% levels, respectively. For (ii), the null-hypothesis probability for pseudobolometric, UV, and r -band peak brightness (rise time) is 23.1(1.67)%, 73.3(1.9)%, and 69.4(83.3)%, respectively. For (iii), the null-hypothesis probability for pseudobolometric, UV, and r -band peak brightness (rise time) is 17.3(0.24)%, 92.6(1.51)%, and 46.6(60.1)%, respectively. Therefore, we conclude that the gold sample is significantly more luminous than the comparison sample in bolometric and optical light curves, but luminosity differences within the classes of the gold sample are not statistically significant. Given the large number of limits present in the $w2$ -band light curves, peak UV luminosity differences between gold and comparison samples cannot be claimed as significant. Furthermore, there is evidence that the differences in bolometric and UV rise times between Classes 1 and 2 versus 3, as well as Class 1 versus 3, are statistically significant. However, differences in the rise time between all other groups are not statistically significant.

3.2. Spectroscopic Properties

We present single epoch, “flash” spectroscopy of the gold/silver and comparison samples in Figures 3 and A1, respectively, with complete spectral series shown for each object in the supplementary, online-only text. As discussed in Section 2.1, the blue (Class 1), yellow (Class 2), and red (Class 3) color delineation is based on the structure of the He II $\lambda 4686$ line, which is shown in detail for all gold/silver-sample objects in Figure 8. As illustrated in Figure 9, the II-like features of semisolated (i.e., unblended) transitions such as H α can be modeled with a two-component Lorentzian, which includes a narrow component that provides an upper limit on the CSM velocity (due to likely radiative acceleration) and a broad component that forms from electron scattering of recombination-line photons in the optically thick unshocked CSM. The physical origin of the He II $\lambda 4686$ profile is slightly more complex and can be modeled with a high-velocity, blueshifted, full width at half-maximum intensity (FWHM) $\approx 10^4$ km s $^{-1}$ component representing fast-moving material in the CDS and/or outer ejecta, plus a narrow, and possibly electron-scattering

⁴⁷ https://github.com/wynnjacobson-galan/Flash_Spectra_Sample

⁴⁸ <https://github.com/mniccholl/superbol>

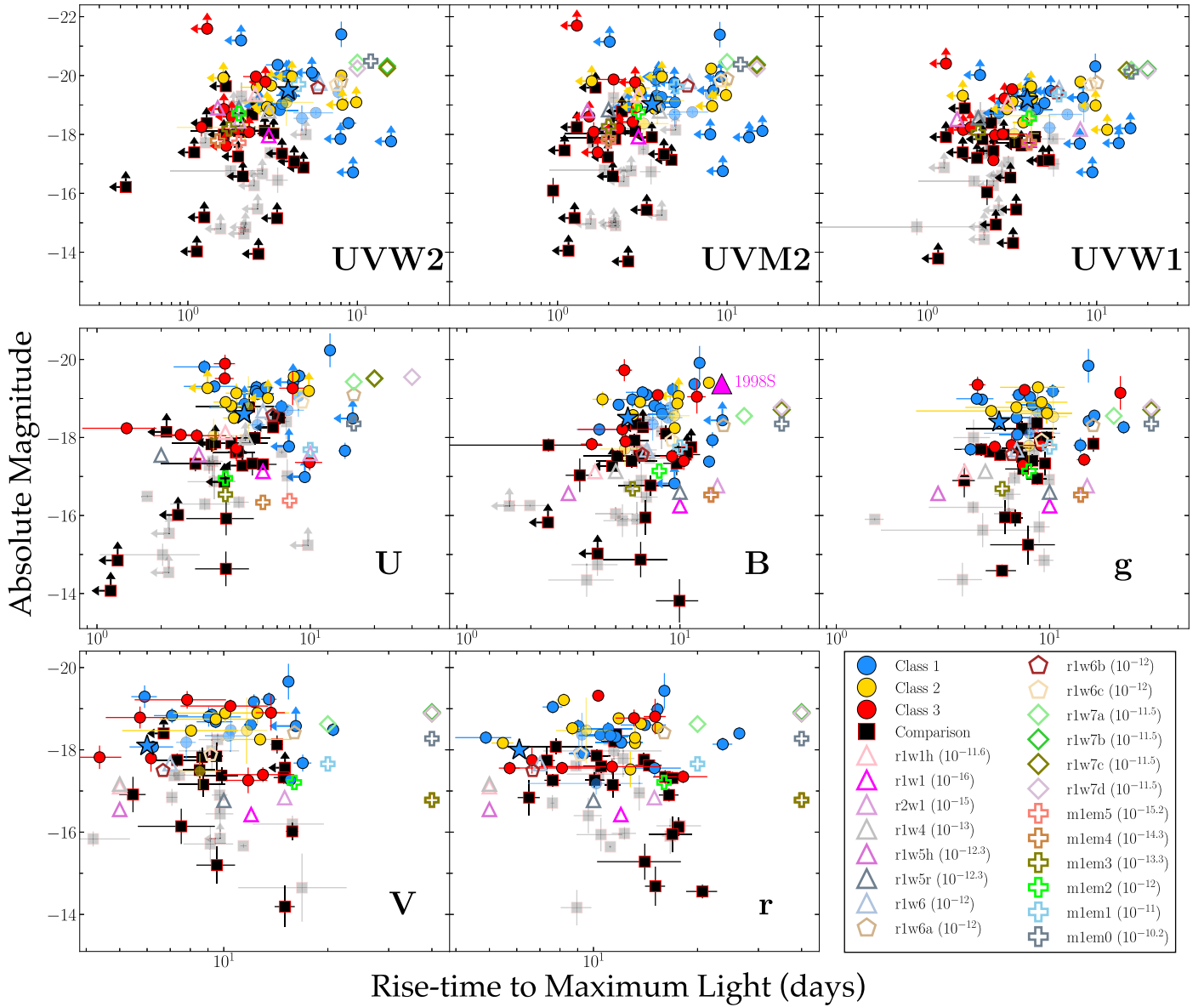


Figure 4. Left to right, top to bottom: Peak absolute magnitude vs. rise time in the $w2$, $m2$, $w1$, u , B/b , V/v , g , and r bands. Gold/silver samples shown as blue/yellow/red circles, and the comparison sample is shown as black squares. Solid colored points represent the subsample of objects at $D > 40$ Mpc. Parameters from the CMFGEN model grid (Section 4.1) are plotted as colored stars, polygons, diamonds, and plus signs with the CSM densities at 10^{14} cm (in grams per cubic centimeter) for each model displayed in parentheses. SNe 1998S and 2023ixf are shown for reference as a magenta triangle and blue star, respectively. We note that the model parameters do not cover the dynamical range of the observations, which will influence the derivation of CSM properties for some objects (Section 4). Furthermore, in the UV bands, the data show significantly larger variance than the models, which follow a well-defined trend. This likely indicates a dependence on a variable not included in the models.

broadened, emission at the central wavelength for Class 2 and 3 objects (e.g., 2014G and 2013fs; Figure 9). However, Class 1 objects (e.g., 2020pni; 9) require multiple narrow and electron-scattering emission components of He II and N III, which may be superimposed on an underlying, blueshifted He II profile, the same as Classes 2 and 3 (e.g., see Dessart et al. 2017).

As confirmed by our sample, the narrow, symmetric line profiles with Lorentzian wings caused by electron scattering (i.e., IIn-like) can persist for days after first light. After these phases, the SNe develop broad P-Cygni profiles in all Balmer transitions as a result of the escape of photons from the fast-moving ejecta and a decrease in CSM density. We therefore define the duration of the IIn-like features (i.e., t_{IIn}) as the transition point at which the unshocked CSM optical depth to electron scattering has dropped enough to see the emerging

fast-moving SN ejecta (Dessart & Jacobson-Galán 2023; Jacobson-Galán et al. 2023). This evolution is shown in Figure 10 for gold-sample SNe 2013fs, 2017ahn, and 2018zd, all of which have high enough spectral cadence to allow for a precise observation of the fading of the IIn-like features. We use this transition to calculate t_{IIn} and its uncertainty, which is derived from the cadence of the spectral observations. For gold/silver-sample objects without a sufficiently high spectral cadence to confidently estimate t_{IIn} , we use spectral comparisons to SNe 2013fs, 2017ahn, and 2018zd to derive a IIn-like feature duration timescale by extrapolating phase measurements and assuming that the spectral evolution is consistent with the SNe used for reference. The uncertainty of t_{IIn} from spectral comparison is added in quadrature with the uncertainty in the time of first light for each sample object. For

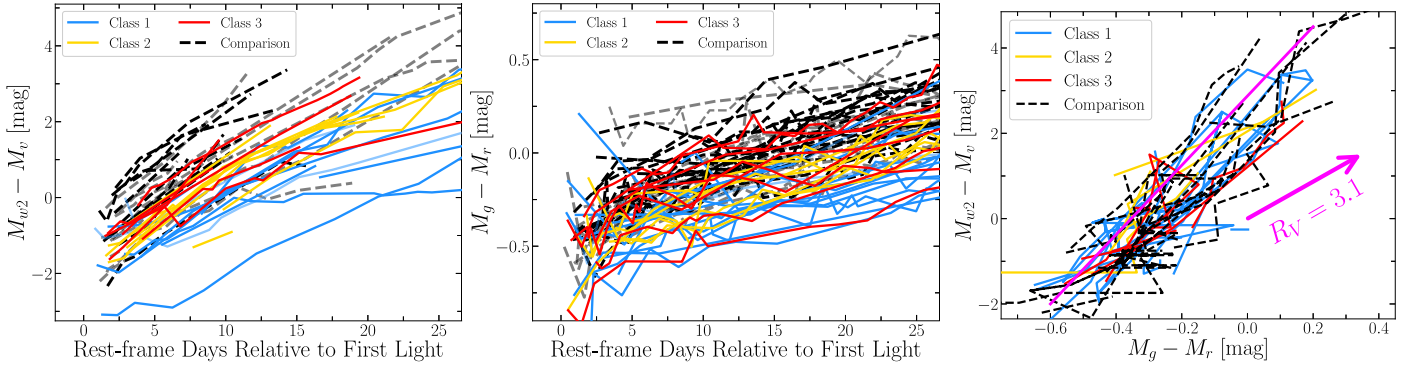


Figure 5. Left: Early time, reddening-corrected $W2 - V$ color plot for gold- and silver-sample objects (red, yellow, blue lines) compared to comparison-sample objects (black dashed lines). Solid colored curves represent the subsample of objects at $D > 40$ Mpc. Gold- and silver-sample objects, in particular the Class 1 objects, show significantly bluer colors than Class 2/3 or comparison-sample objects, which is indicative of increased temperatures from persistent CSM interaction. Middle: early time, reddening-corrected $g - r$ color plot shows a less clear delineation between objects/classes with varying signatures of CSM interaction, suggesting that the UV colors are the most sensitive metric for confirming ejecta–CSM interaction. Right: $W2 - V$ vs. $g - r$ colors for gold- and comparison-sample objects. The reddening vector for $R_V = 3.1$ using the Fitzpatrick (1999) reddening law is shown as a magenta arrow.

comparison-sample objects, which do not show IIn-like features, we take the phase of their earliest spectrum to be an upper limit on t_{IIn} . All t_{IIn} values are presented in Table A6.

In Figures 6 and 11, we plot t_{IIn} with respect to the peak luminosity for all UV, optical, and pseudobolometric light curves. We find a moderate positive trend between peak luminosity and t_{IIn} in $w2$ -, $m2$ -, $w1$ -, u -, b -band filters, which is similar to the rise-time trends shown in Figure 4. While the peak absolute magnitude in optical v -, g -, r -band filters reveals a more obvious trend with t_{IIn} than t_{rise} , their correlation can only be claimed as tentative. A similar trend is found in Bruch et al. (2023) between the duration of narrow He II emission and g -band peak magnitude. Furthermore, as shown in Figure 6, peak pseudobolometric luminosities and the duration of IIn-like features are moderately correlated. Among the gold/silver samples, Class 1 objects consistently show the highest peak luminosities across wavelengths, coupled with a longer duration of observed IIn-like features, indicating ejecta–CSM interaction with denser, and likely more extended, CSM than Class 2/3 objects (e.g., see Figures 7 and 13).

As the IIn-like features fade, all gold/silver-sample objects transition into standard SNe II with Doppler-broadened, blueshifted P Cygni features of the fast-moving, H-rich ejecta. In Figure 12, we present photospheric velocities calculated from the absorption minima of $H\alpha$ and Fe II $\lambda 5169$ transitions for gold-, silver-, and comparison-sample objects. Overall, there is some spread in $H\alpha$ velocities among gold/silver-sample objects with a few Class 1 SNe displaying slower velocities ($v \approx 5000\text{--}8000$ km s $^{-1}$) than Classes 2/3 ($v > 10^4$ km s $^{-1}$). However, in general, we find little difference in the $H\alpha$ and Fe II velocities found in the absorption minima between gold/silver and comparison sample from $\delta t \approx 10\text{--}100$ days.

4. Modeling

4.1. HERACLES/CMFGEN Model Grid

In order to quantify the CSM properties in our gold, silver, and comparison samples, we compared the spectral and photometric properties of all SNe to a model grid of radiation hydrodynamics and non-LTE, radiative-transfer simulations covering a wide range of progenitor mass-loss rates ($\dot{M} = 10^{-6}\text{--}10^0 M_{\odot} \text{yr}^{-1}$; $v_w = 50$ km s $^{-1}$), maximum radii of dense CSM ($R = 10^{14}\text{--}10^{16}$ cm), and CSM densities at 10^{14} cm ($\rho_{14} = 10^{-16}\text{--}7.3 \times 10^{-11}$ g cm $^{-3}$), all in spherical symmetry.

Simulations of the SN ejecta–CSM interaction were performed with the multigroup radiation-hydrodynamics code HERACLES (González et al. 2007; Vaytet et al. 2011; Dessart et al. 2015), which consistently computes the radiation field and hydrodynamics. Then, at selected snapshots in time postexplosion, the hydrodynamical variables are imported into the non-LTE radiative-transfer code CMFGEN (Hillier & Dessart 2012; Dessart et al. 2015) for an accurate calculation of the radiative transfer, which includes a complete model atom, $\sim 10^6$ frequency points, a proper handling of the complex, nonmonotonic velocity field, and treatment of continuum and line processes as well as electron scattering. For each model, we adopt an explosion energy of 1.2×10^{51} erg, a $15 M_{\odot}$ progenitor with a radius in the range $R_{*} \approx 500\text{--}700 R_{\odot}$, and a CSM composition set to the surface mixture of an RSG progenitor (Davies & Dessart 2019).

For the simulations presented in this work, the CSM extent is much greater than R_{*} ($\sim 500\text{--}1200 R_{\odot}$ for an RSG mass range of $\sim 10\text{--}20 M_{\odot}$), and therefore, we have found that the progenitor properties have little impact during phases of ejecta–CSM interaction. The progenitor radius plays a more significant role on the light-curve evolution during the plateau phase (e.g., see Dessart et al. 2013; Hiramatsu et al. 2021; Jacobson-Galán et al. 2022), once the interaction phase is over, and the emission from the deeper ejecta layers dominate the SN luminosity. However, in scenarios with weak CSM interaction, the explosion energy will greatly influence the total luminosity, which could be contributing to the brighter pseudobolometric and UV luminosities in comparison-sample events (e.g., Figures 1 and 6). Specific methods for each simulation are given by Dessart et al. (2016, 2017), Jacobson-Galán et al. (2022), Dessart & Jacobson-Galán (2023), and Jacobson-Galán et al. (2023); all CSM properties of each model are presented in Table A2. CSM densities for all models are shown in Figure 14, which primarily differ at radii above the stellar surface, $r > 4 \times 10^{13}$ cm.

In order to identify a best-matched \dot{M} and ρ_{14} for all sample objects, we employ three independent methods of matching observables to the model grid. (1) We use the rise times, peak absolute magnitudes, and t_{IIn} to construct a three-dimensional rms between each model for all eight UV/optical filters and the pseudobolometric light curve. We then select the best-matched model for a given filter (as well as pseudobolometric) based on the lowest resulting rms, $[(M_{\text{data}} - M_{\text{model}})/M_{\text{model}}]^2 + ((t_{r,\text{data}} - t_{r,\text{model}})/t_{r,\text{model}})^2 + ((t_{\text{IIn,data}} - t_{\text{IIn,model}})/t_{\text{IIn,model}})^2]^{0.5}$. This

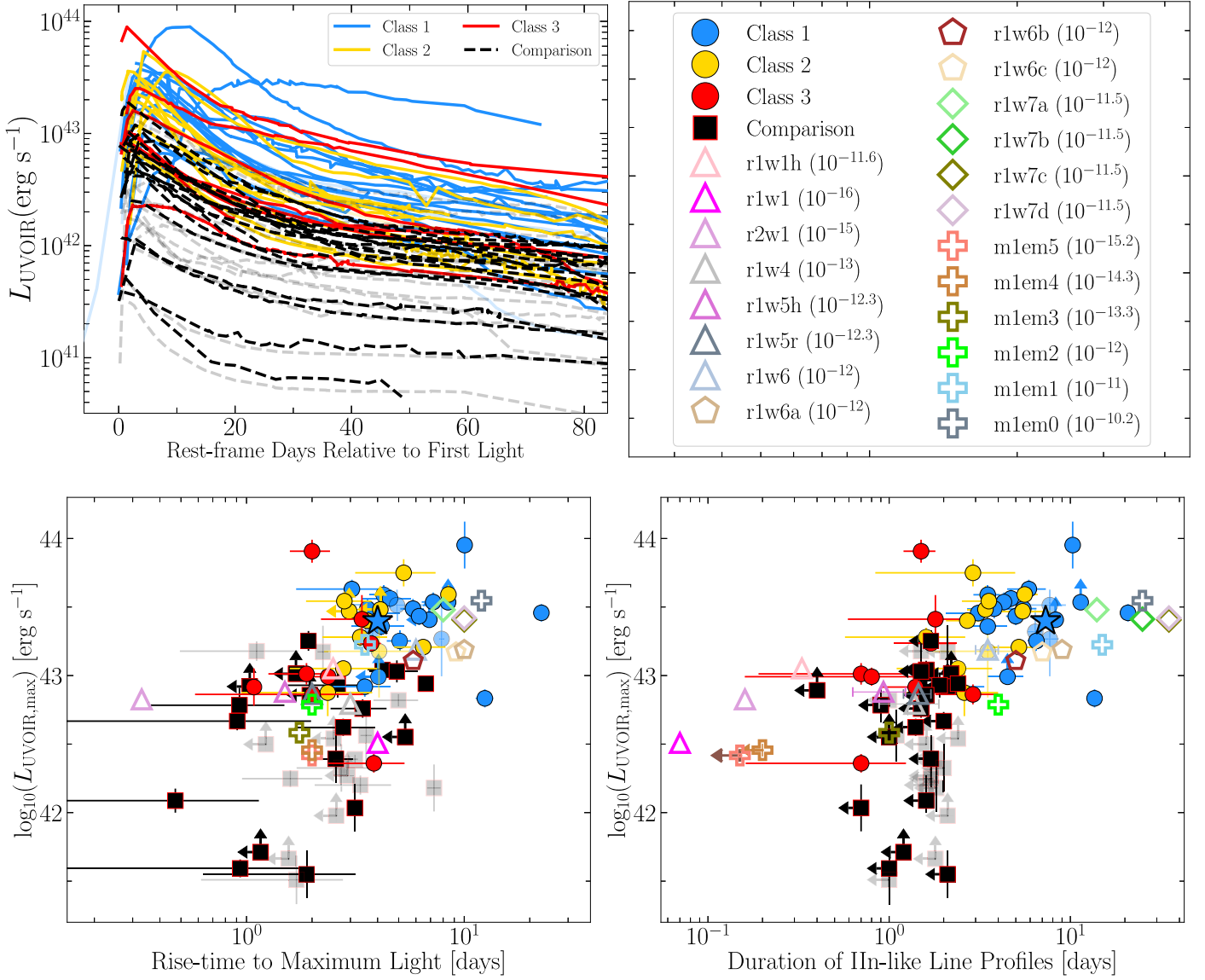


Figure 6. Top left: Pseudobolometric (i.e., UVOIR) light curves of gold/silver samples (blue/yellow/red solid lines) and the comparison sample (dashed black lines). Solid colored points/curves represent the subsample of objects at $D > 40$ Mpc. The CSM interaction present in SNe II with IIn signatures can create more than an order of magnitude luminosity excess beyond SNe II in low-density CSM. The light curve of gold-sample object SN 2020tlf (blue) extends before first light because of detected precursor emission (Jacobson-Galán et al. 2022). Top right: legend with all models. Bottom left: peak bolometric luminosity vs. rise time for gold-, silver-, and comparison-sample objects, compared to CMFGEN model grid. Bottom right: Peak bolometric luminosity vs. duration of IIn-like features (t_{IIn}) also shows a clear positive trend (Section 3.2). SN 2023ixf is shown for reference as a blue star.

method results in $N + 1$ mass-loss inferences: N filters plus the pseudobolometric light curve. The range of mass-loss rates and CSM densities for all filters are presented in Table A7 and plotted in the left panels of Figure 15. For this method, we do not incorporate the relative uncertainties in peak luminosities and rise times, but instead report the range of best-matched model parameters as the uncertainty in the derived \dot{M} and ρ_{14} . However, as discussed in Section 3.1, the peak absolute magnitude and rise times, especially in UV filters, are unconstrained in some sample objects, which will influence the best-matched model parameters. For such objects, we use upper limit or the ill-constrained peak and rise-time values reported in Table A3 in the above rms relation, but note that the output model parameters may only represent limits on the true CSM properties in these SNe. (2) We minimize the residuals between only t_{IIn} estimates for each object in order to find the best-matched model in the grid, which is plotted in the middle panels of Figure 15 with error bars on mass-loss/density estimates

coming from uncertainties in the given t_{IIn} values. (3) We perform direct spectral matching of CMFGEN synthetic spectra to gold-, silver-, and comparison-sample objects in order to estimate the most consistent mass-loss rates and CSM densities. To do this, we degrade the synthetic spectrum to the resolution of the SN spectrum and scale the average flux of each model spectrum to the observations over the wavelength range of the optical spectrum, and calculate the residuals in flux density between model and data in the wavelength ranges that cover emission lines of the H I Balmer series, He II $\lambda\lambda 4686, 5412$, N III $\lambda 4641$, N IV $\lambda 7112$, and C IV $\lambda 5801$. For each sample object, we estimate a best-matched mass-loss rate and CSM density (right panels of Figures 15) by selecting the model with the smallest average residual (i.e., $\bar{\Delta}_{\text{IIn}}$) between model and SN spectra in all IIn-like feature wavelength ranges. However, we note that the best-matched model spectrum may not reproduce the intrinsic continuum flux of the SN data despite overall consistency with the observed IIn-like features.

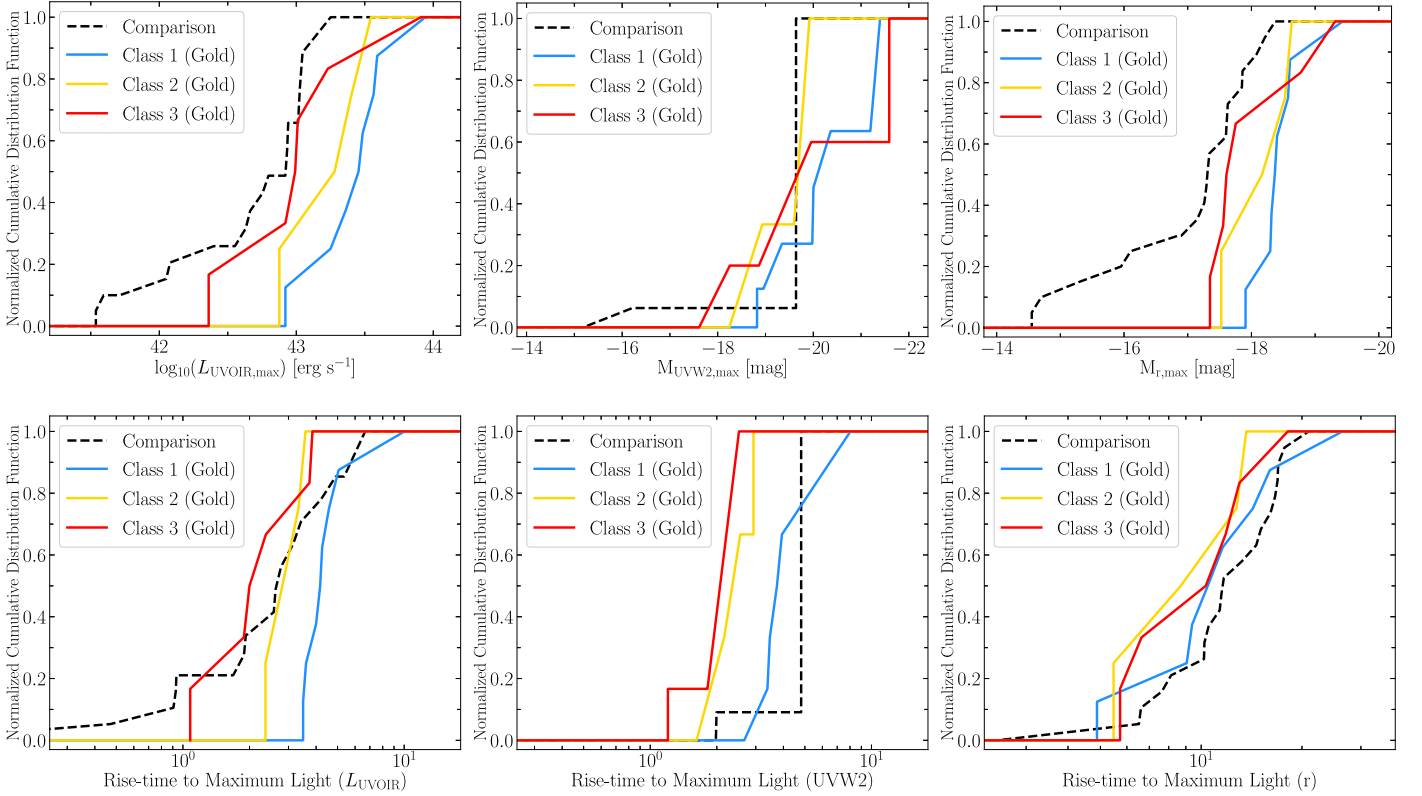


Figure 7. Left to right, top to bottom: Cumulative distributions of peak UVOIR luminosities, peak w2-band absolute magnitudes, peak r -band absolute magnitudes, UVOIR rise times, w2-band rise times, and r -band rise times for Class 1, 2, 3 gold-sample (blue, yellow, red lines) and comparison-sample (black dashed lines) objects after a distance cut ($D > 40$ Mpc) is applied. Distinct distributions are present in the peak bolometric and optical luminosities for gold-sample objects compared to the comparison-sample SNe, which is most likely due to the effects of CSM interaction on the early time light curves.

Similarly, the best-matched model using method 1 may not match the SN light-curve shape on the rise despite consistency with peak brightness and rise time. We discuss inconsistencies between model-matching methods below as well as future improvements to the grid in Section 5.2.

Below, we discuss the resulting mass-loss rates and CSM densities derived for each model-matching method. We find that gold/silver-sample objects with visible IIn-like features reside in a parameter space of progenitor CSM densities of $\sim 10^{-16}$ – 10^{-11} g cm⁻³ ($\dot{M} \approx 10^{-6}$ – 10^{-1} M_{\odot} yr⁻¹, $v_w = 50$ km s⁻¹) when comparing rise times, peak absolute magnitudes, and t_{IIn} to the model grid (i.e., methods 1 and 2). However, this parameter space becomes more constrained to $\sim 5 \times 10^{-14}$ – 10^{-11} g cm⁻³ ($\dot{M} \approx 10^{-3}$ – 10^{-1} M_{\odot} yr⁻¹, $v_w = 50$ km s⁻¹) when using a direct spectral matching method (i.e., method 3). With regards to subdivisions of the gold and silver samples, the Class 1 objects show the highest mass-loss rates of $\dot{M} \approx 5 \times 10^{-3}$ – 10^{-1} M_{\odot} yr⁻¹, Class 2 objects show low to intermediate mass-loss rates of $\dot{M} \approx 10^{-6}$ – 10^{-2} M_{\odot} yr⁻¹, and Class 3 objects display generally lower mass-loss rates of $\dot{M} \approx 10^{-6}$ – 10^{-3} M_{\odot} yr⁻¹. Furthermore, comparison-sample objects that have no detected IIn-like features at $\delta t < 2$ days are consistent with overall low mass-loss rates of $\dot{M} \approx 10^{-6}$ – 10^{-3} M_{\odot} yr⁻¹. Across all three model-matching methods, the average \dot{M} derived is consistent to within an order of magnitude (e.g., see Figure A6 in the Appendix). However, there are instances where mass-loss rates derived from some peak magnitudes or rise times in method 1 are inconsistent with what would be inferred from methods 2 and 3 involving t_{IIn} and direct spectral matching. For example, many of the

Class 3 objects have \dot{M} ranges of $\sim 10^{-6}$ – $10^{-2.3}$ M_{\odot} yr⁻¹ based on method 1, but have more constrained estimates of $\sim 10^{-3}$ – $10^{-2.3}$ M_{\odot} yr⁻¹ based on methods 2 and 3 that are inconsistent with the lower \dot{M} values. This is caused by similar peak absolute magnitudes and/or rise times across models in optical filters as well as the low resolution of the model grid in general. With future grids, the incorporation of additional explosion parameters such as a variable kinetic energy will provide more self-consistent results between model-matching methods.

As shown in Figure 15, there is a clear trend between the t_{IIn} parameter and derived mass-loss rates or CSM densities for both gold/silver- and comparison-sample objects. We then fit a linear function to the mass-loss rates and t_{IIn} from the model grid and overplot the function as black dashed lines in Figure 15. This relation between the duration of the electron-scattering line profiles and the inferred mass-loss rate, in units of M_{\odot} yr⁻¹, goes as $t_{\text{IIn}} \approx 3.8[\dot{M}/(0.01 M_{\odot} \text{ yr}^{-1})]$ days. We note that this correlation is valid for the chosen explosion and progenitor parameters.

Additionally, we calculate the velocities of the fastest moving H-rich ejecta that we can detect at $\delta t = 50$ days by examination of the bluest (reddest) edge of the absorption (emission) profiles in H α . However, we note that there is likely faster, optically thin H-rich material that we cannot detect in these spectra, and, therefore, these estimates provide a lower limit on the velocity of the fastest ejecta. We then compare to model predictions from Dessart & Jacobson-Galán (2023) for the deceleration of ejecta as a function of total mass in the CDS, which is also connected to the mass-loss rate. From a

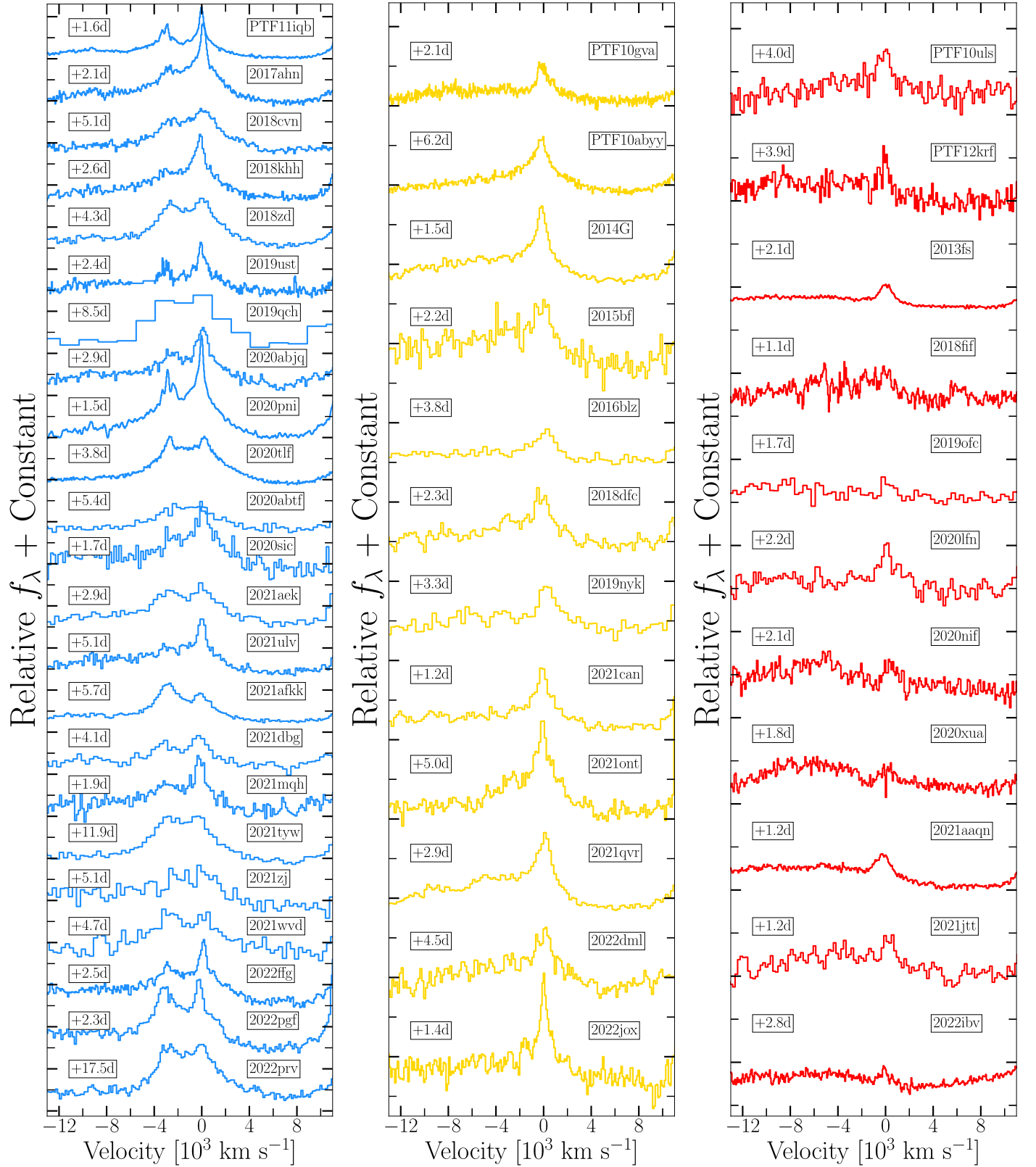


Figure 8. He II emission-line profiles for gold- and silver-sample objects. Left: SNe with visible, narrow N III emission are shown in blue (Class 1). Middle/right: objects plotted in yellow (Class 2) and red (Class 3) show only narrow He II emission lines, the latter possessing the weakest emission superimposed on top of the broad He II profile from the fastest moving SN ejecta.

comparison to the models, the slow moving ejecta of some Class 1/2 objects would indicate enhanced mass-loss rates of $\dot{M} = 10^{-3}\text{--}10^0 M_{\odot} \text{ yr}^{-1}$, while the velocities observed in other

Class 1/2 and all Class 3 objects suggest low mass-loss rates of $\dot{M} < 10^{-5} M_{\odot} \text{ yr}^{-1}$; these values are presented Figure 16. However, many of the Class 1, as well as all of the Class 2 and

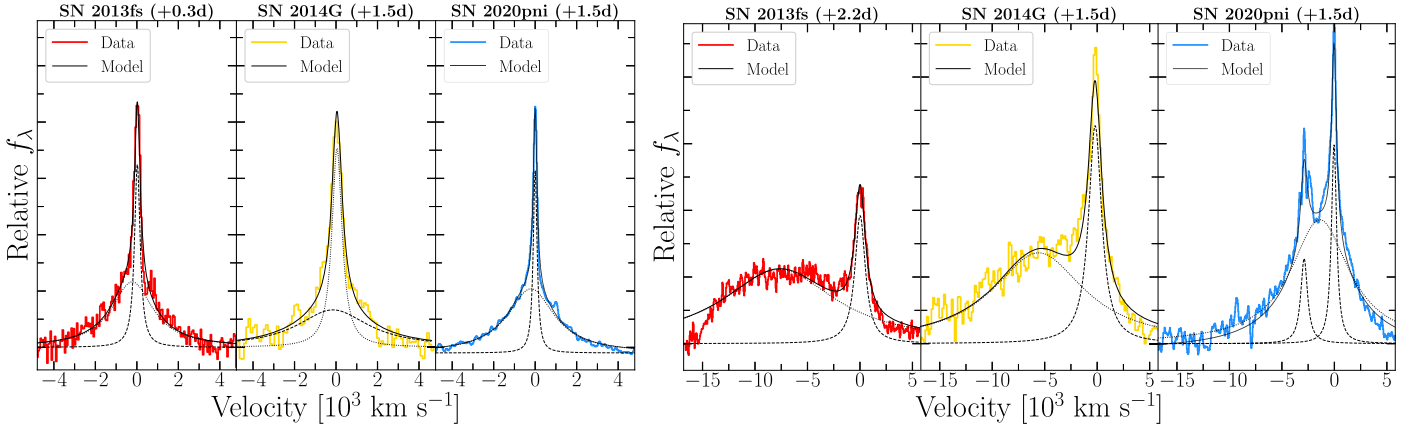


Figure 9. $H\alpha$ (left) and $\text{He II } \lambda 4686$ (right) emission lines modeled with multicomponent Lorentzian profiles during the CSM interaction phase. Class 1 objects (shown in blue) possess longer-lived (days-to-weeks) high-ionization species of He II and N III . Class 2 (shown in yellow) and Class 3 (shown in red) objects show only He II emission, with the former having stronger emission lines that last longer. Class 3 objects may represent transitional SNe between the comparison and gold/silver samples given their weak narrow He II emission superimposed on a blueshifted He II profile, the latter being seen in comparison-sample objects (e.g., Figure A1).

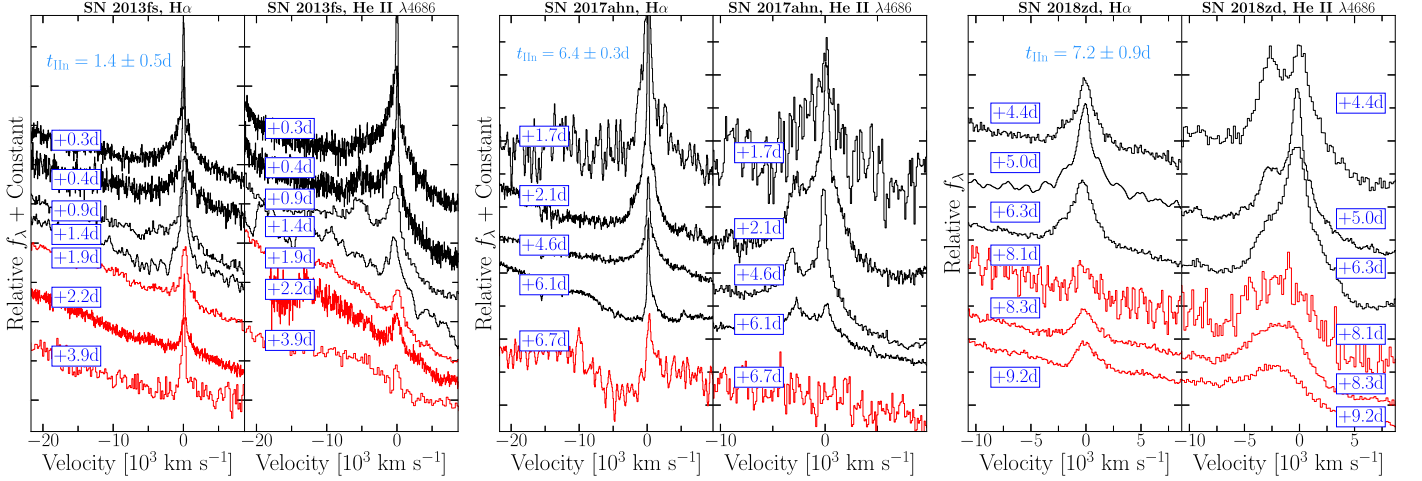


Figure 10. Left: SN 2013fs spectral series of $H\alpha$ (left panel) and $\text{He II } \lambda 4686$ (right panel) velocities during the CSM interaction phase. Spectra in black represent phases when the CSM remains optically thick to electron scattering (e.g., Lorentzian line profiles). The transition shown from black to red lines marks the emergence of broad absorption features derived from the fastest moving SN ejecta. The transition between these two phases is the basis for calculating the t_{In} parameter. Middle/right: same plot but for SNe 2017ahn and 2018zd, respectively, which show longer-lived IIn profiles.

3, mass-loss rates inferred for gold/silver-sample objects from direct spectral matching are larger than those that are estimated from the fastest moving ejecta. This potentially suggests a degree of CSM asymmetry that would keep some fraction of the ejecta from being decelerated by dense CSM at early times, as is predicted by CMFGEN models for spherically symmetric CSM.

4.2. Additional Model Grids

In order to better explore the parameter space of ejecta–CSM interaction in SNe II, we perform the same spectral matching analysis as above but with the public⁴⁹ grid of CMFGEN models presented by Boian & Groh (2020). This model grid consists of 137 synthetic spectra with varying CSM compositions (e.g., solar metallicity, CNO-enriched, He rich), mass-loss rates ($\dot{M} = 10^{-3}$ – $10^{-2} M_{\odot} \text{ yr}^{-1}$), inner radii of the interaction region ($R_{\text{in}} = 8 \times 10^{13}$ – 3.2×10^{14} cm), and SN luminosity ($L_{\text{SN}} = 1.9 \times 10^8$ – $2.5 \times 10^{10} L_{\odot}$). These models impose an optically

thick wind in radiative equilibrium, assume steady state, and have an input luminosity, CSM radius, and mass-loss rate at a given time step. Furthermore, these models contain no radiation hydrodynamics, and all of the CSM remains unshocked/unaccelerated at all phases. Similar to our presented model grid, we scale each model spectrum to the observations over the wavelength range of the optical spectrum and calculate the minimum average residual in wavelength regions of IIn-like features (i.e., Δ_{IIn}). An example of this matching process is shown for SN 2020abjq in Figure 17, and all best-matched model parameters for gold and silver samples are listed in Table A7 and plotted in Figure 17.

We find rough agreement between the mass-loss rates derived from the Boian & Groh (2020) grid and our own: 20 out of 39 objects having mass-loss rates that are consistent to within 50%. However, the Boian & Groh (2020) grid does not explore a sufficiently large range of CSM properties (e.g., $\dot{M} > 10^{-2} M_{\odot} \text{ yr}^{-1}$, $\dot{M} < 10^{-3} M_{\odot} \text{ yr}^{-1}$, $R_{\text{CSM}} > 3 \times 10^{14}$ cm), so these mass-loss estimates may be more biased by the model grid. Furthermore, the Boian & Groh (2020) model spectra only cover the phases of $\delta t = 1.0$ – 3.7 days

⁴⁹ <https://www.wiserep.org/object/14764>

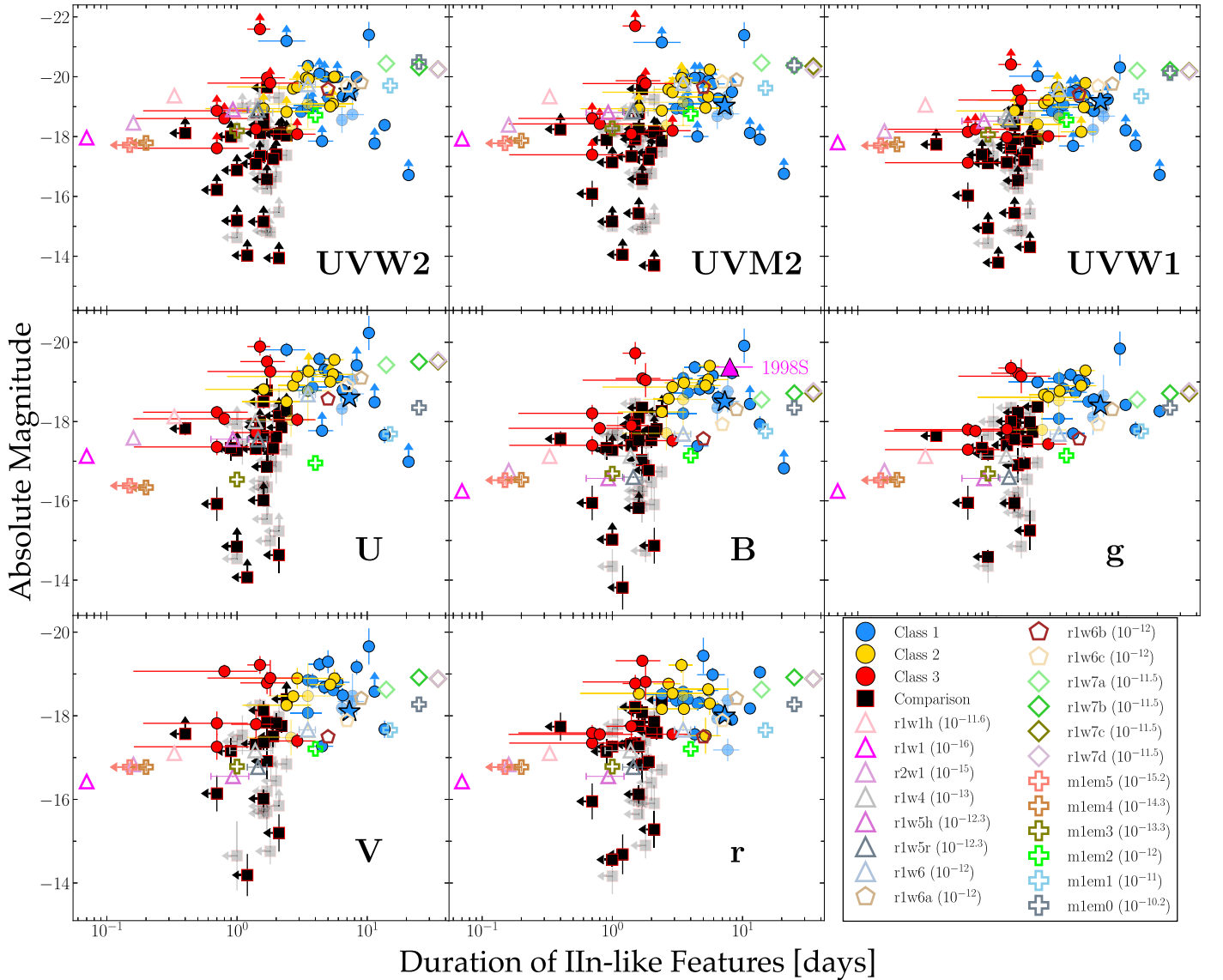


Figure 11. Left to right, top to bottom: Peak absolute magnitude in the $w2$, $m2$, $w1$, u , B/b , V/v , g , and r bands vs. duration of IIn-like features. Gold and silver samples shown as blue/yellow/red circles and comparison sample shown as black squares. Solid colored points represent the subsample of objects at $D > 40$ Mpc. Parameters from the CMFGEN model grid (Section 4.1) are plotted as colored stars, polygons, diamonds, and plus signs. SNe 1998S and 2023ixf are shown for reference as a solid magenta triangle and solid blue star, respectively.

(assuming a shock velocity of 10^4 km s^{-1}) and also do not create synthetic multiband and bolometric light curves to compare with the sample photometry. Nonetheless, the advantage of this model grid is the variety of CSM compositions explored.

In addition to the Boian & Groh (2020) spectral models, we also apply a grid of synthetic light curves for SBO from dense CSM presented by Haynie & Piro (2021). The model grid contains 168 multiband light curves created with the LTE, Lagrangian radiative-transfer code SNEC (Morozova et al. 2015) for varying mass-loading parameter $D_* = \dot{M}/(4\pi v_w) = 8 \times 10^{16} - 10^{18} \text{ g cm}^{-1}$, explosion energy ($E_k = (0.3 - 3.0) \times 10^{51} \text{ erg}$), and CSM radius ($R_{\text{CSM}} = 1500 - 2700 R_\odot$). For all objects in the gold/silver and comparison samples, we find the most consistent model by minimizing the residuals between the synthetic light curves and the observed UVOIR photometry at $\delta t < 20$ days. First light in these models is assumed to be when the synthetic absolute magnitude rises above -12 mag.

Furthermore, we note that the uncertainty in the time of first light associated with each sample object could lead to uncertainties in the model parameters derived from the best-matched model light curves. However, these uncertainties are not large enough to impact the overall model trend observed in Figure 18. An example of a best-match light-curve model to Class 2 gold-sample object SN 2022jox is shown in the left panel of Figure 18; all derived model parameters are listed in Table A7.

As shown in Figure 18, the CSM properties inferred from the best-matched SNEC light curves are inconsistent with those derived from both CMFGEN model grids. For example, the best-matched light-curve model from Haynie & Piro (2021) implies $D_* [R_{\text{CSM}}] = 10^{18} \text{ g cm}^{-1} [1900 R_\odot]$ for SN 2013fs, similar to what was found in Morozova et al. (2017), which is several orders of magnitude higher than the most consistent CMFGEN model for this SN (e.g., $D_* \approx 10^{15} \text{ g cm}^{-1}$). Similarly, the distribution of D_* values derived for the comparison sample

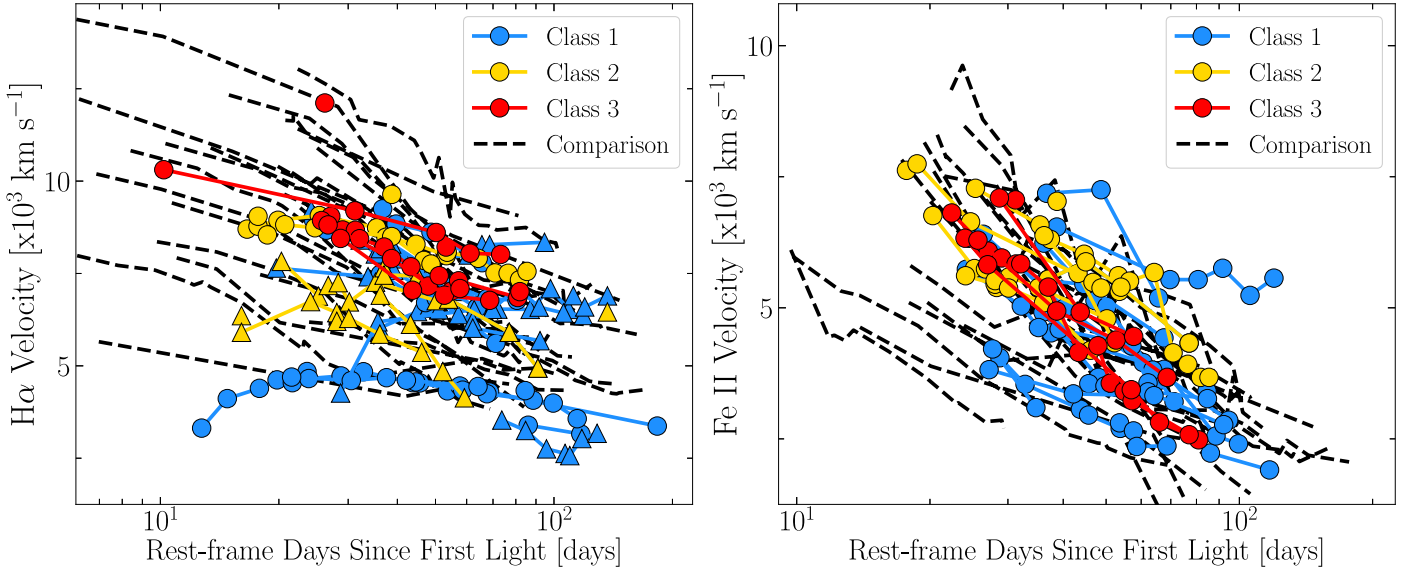


Figure 12. Photospheric-phase velocities for gold/silver- (blue, yellow, red lines) and comparison- (black dashed lines) sample objects calculated from absorption minimum (circles) or emission FWHM (triangles) of H α (left) and Fe II λ 5169 (right) line profiles. While some gold-sample objects with more persistent CSM interaction show slower ejecta velocities than the comparison sample, overall both samples possess a consistent evolution in their photospheric velocities.

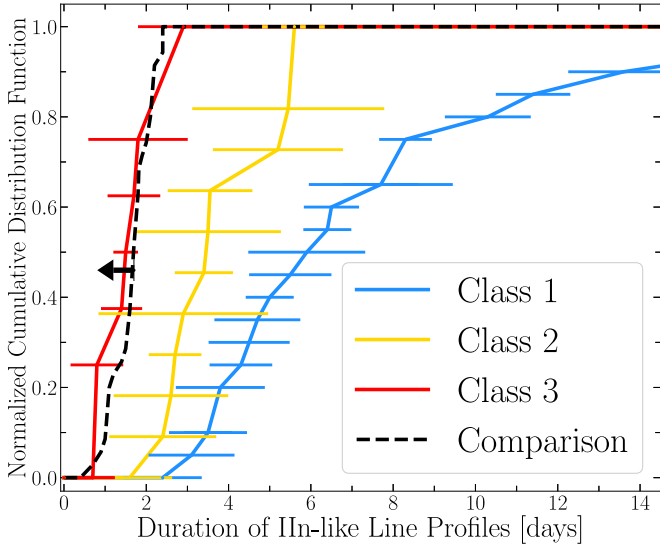


Figure 13. Cumulative distribution of t_{In} values in Class 1 (blue), 2 (yellow), and 3 (red) gold- and silver-sample objects, as well as upper limits from the comparison sample. Overall, Class 1 objects have longer durations of observed IIn-like features, indicating higher-density, and possibly more extended, CSM.

is consistent with the distribution of D_{\star} values found by Morozova et al. (2018; e.g., $\sim 10^{17-18} \text{ g cm}^{-1}$) when modeling the light curves of normal SNe II with SNEC. However, the large densities derived from SNEC models ($\rho_{14} \approx 10^{-10} \text{ g cm}^{-3}$) would imply mean free paths of $l_{\text{mfp}} \approx 3 \times 10^{10} \text{ cm}$ for close-in CSM, $\sim 2R_{\star}$. Such mean free paths are much smaller than the size of extended CSM ($\sim 10^{14-15} \text{ cm}$); therefore, electron-scattered photons created from photoionized gas would never escape the CSM to create the IIn-like features observed in the optical spectra while the shock wave is inside of this part of the CSM. Furthermore, at these densities, the ionization parameter will be >10 (i.e., $\xi = L_{\text{sh}}/nr^2$), indicating that the gas will be completely ionized (Lundqvist & Fransson 1996; Chevalier & Irwin 2012). As shown by Dessart & Jacobson-Galán (2023), SBO into CSM densities this large will trap the photons stored in

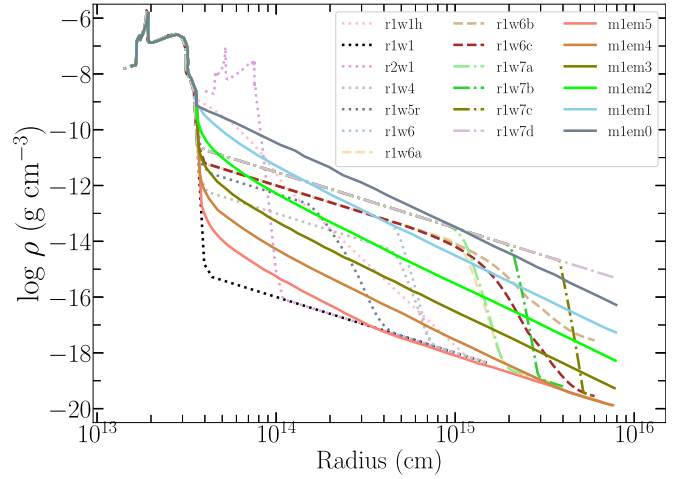


Figure 14. CSM densities and radii for complete CMFGEN model grid (e.g., Table A2) used to find the best-matched model for gold-, silver-, and comparison-sample objects. A description of the model setup is provided in Section 4.1.

the wake of the radiation-dominated shock until the shock has exited the edge of the densest material; the shock front will propagate adiabatically and will not extract kinetic energy that can be used to boost the overall luminosity, as is the case for lower-density CSM. Consequently, SBO from such high-density material may provide additional luminosity to early time light curves, but lower-density ($\rho \approx 10^{-12-14} \text{ g cm}^{-3}$) material at larger distances ($r \approx 10^{14-15} \text{ cm}$) is needed to create IIn-like features observed in gold/silver-sample objects.

5. Discussion

5.1. A Continuum of RSG Mass-loss Rates

In Section 4.1, we presented three independent model-matching methods used to derive mass-loss rates and CSM densities for 39 SNe II (gold/silver samples) with IIn-like features as well as for 35 SNe II without such spectral signatures. In the total sample, we find significant diversity among the mass-loss rates and CSM

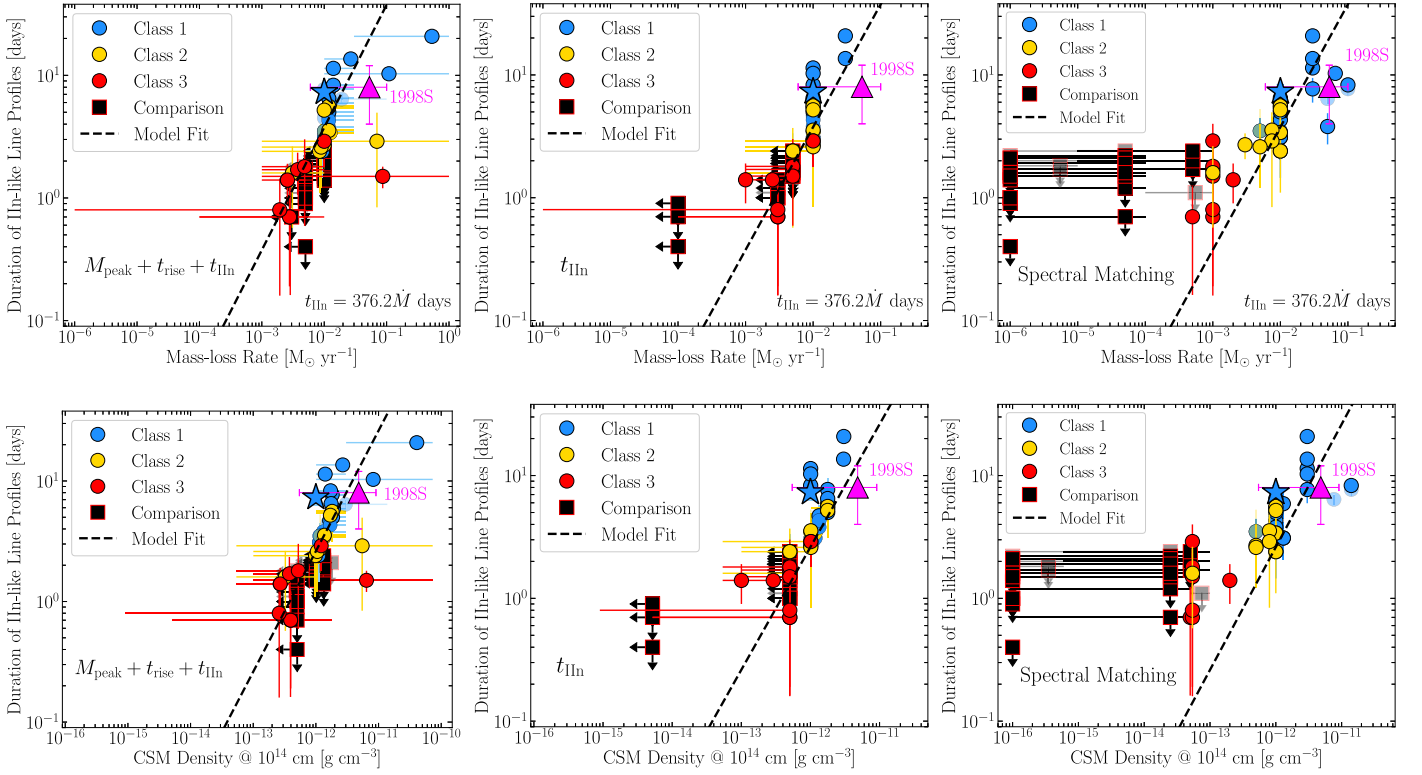


Figure 15. Duration of IIn-like features vs. best-matched mass-loss rates (top panel) and CSM densities at $r = 10^{14}$ cm (bottom panel) for all gold/silver- (blue, yellow, and red circles) and comparison- (black squares) sample objects. Solid colored points represent the subsample of objects at $D > 40$ Mpc. SNe 1998S and 2023ixf are shown for reference as a magenta triangle and blue star, respectively. Mass-loss rates were estimated for each object based on comparison of (left) multiband photometry and t_{IIn} , (middle) only t_{IIn} , and (right) early time spectra, to the CMFGEN model grid. Specifics of feature matching and selection of the best model are presented in Section 4.1. A linear relation between t_{IIn} and \dot{M} (black dashed line) is derived from fitting model parameters used in the CMFGEN grid (i.e., the correlations shown are built into our model grid).

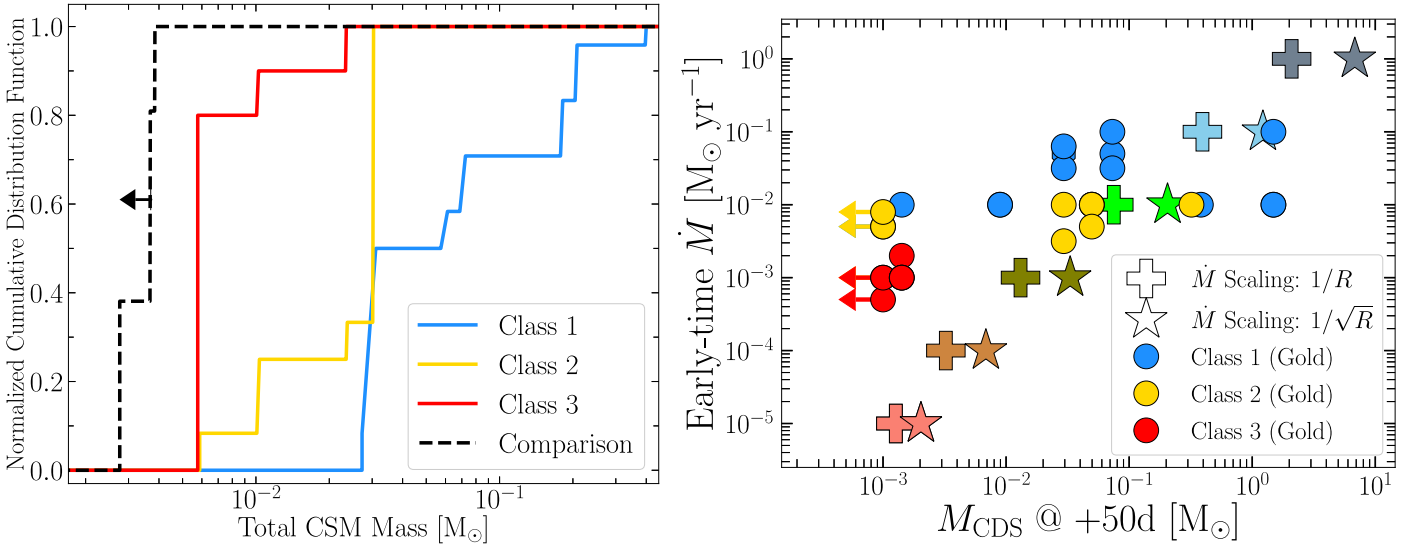


Figure 16. Left: histogram of total CSM mass derived from direct spectral matching of the CMFGEN grid to Class 1 (blue), 2 (yellow), and 3 (red) gold/silver samples, as well as comparison-sample (black) objects, after a distance cut ($D > 40$ Mpc) is applied. Right: CDS mass (abscissa) derived from the maximum velocity of gold- and silver-sample objects as measured from the bluest edge of the $\text{H}\alpha$ absorption profile at $\delta t \approx 50$ day postfirst light using the model trend found by Dessart & Jacobson-Galán (2023) for CMFGEN models of varying mass loss; models shown as plus sign and stars. CDS mass is compared to mass-loss rate (ordinate) derived from comparison of early time observations to CMFGEN model grid.

densities in SNe II, which is intrinsically tied to the distributions of observables between gold/silver and comparison samples such as peak brightness and rise times in their pseudobolometric/UV/optical light curves as well as the duration of the IIn-like features.

Assuming that all gold-, silver-, and comparison-sample objects arise from the explosion of RSGs, this suggests a continuum of mass-loss histories in the final years to months before explosion: Class 1/2 objects (e.g., SNe 201f-like, 20pni-like, 98S-like,

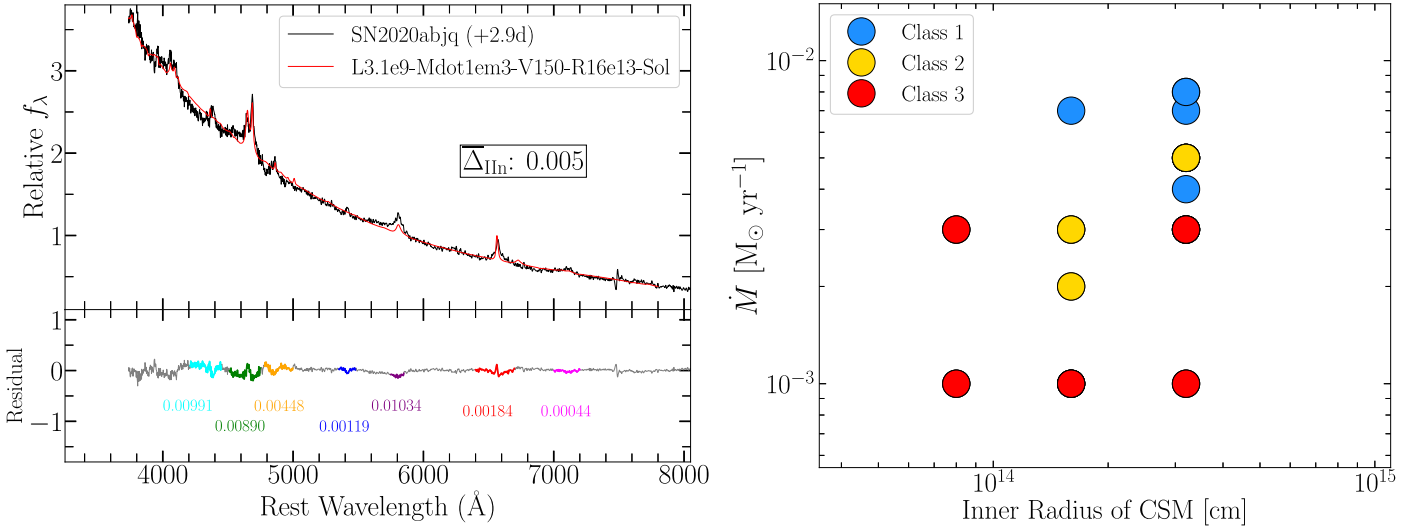


Figure 17. Left: Early time optical spectra of Class 1 gold-sample object SN 2020abjq is shown with respect to the best-matched CMFGEN model from the Boian & Groh (2020) model grid. Specifics of model matching for the complete sample are presented in Section 4.2. Numbers in the bottom panel are the residuals between data and model spectra in the wavelength ranges of IIn-like features (Δ_{IIn}). Right: Best-matching mass-loss rate and inner CSM radius calculated from direct comparison of gold- and silver-sample object spectra to the Boian & Groh (2020) CMFGEN model grid. Some key differences between this grid and that presented in this paper are the lack of spectral time series, multiband photometry, or wider coverage of CSM densities and radii in the former that are present in the latter grid.

14G-like) being associated with RSGs having enhanced mass-loss rates of $\dot{M} \approx 10^{-3}$ – $10^{-1} M_{\odot} \text{ yr}^{-1}$ and potentially extended dense CSM ($r \approx 10^{15}$ – 10^{16} cm), while Class 3 objects (e.g., SN 2013fs-like) may be the result of RSG explosions with lower-density ($\dot{M} \approx 10^{-3}$ – $10^{-4} M_{\odot} \text{ yr}^{-1}$), possibly compact ($r < 5 \times 10^{14}$ cm) CSM. Given the lack of IIn-like features at very early time phases in comparison-sample objects, these SNe need to arise from RSGs with similar or lower mass-loss rates than Class 3 objects ($\dot{M} < 10^{-4} M_{\odot} \text{ yr}^{-1}$), which may make them more consistent with the weak, steady-state mass-loss rates of Galactic RSGs (e.g., $\dot{M} < 10^{-6} M_{\odot} \text{ yr}^{-1}$; Beasor et al. 2020) or highly confined CSM (i.e., $< 10^{14}$ cm) at the time of explosion. Nonetheless, the presence of high-density material directly above the RSG surface may be a universal property of SN II progenitors in order to explain fast-rising light curves (e.g., Morozova et al. 2017).

5.2. Future Improvements to HERACLES/CMFGEN Grids

While the differences in t_{IIn} , as well as possibly UV M_{peak} , are physically linked to differences in CSM density between the gold/silver and comparison samples, the extraction of \dot{M} and ρ_{14} estimates from a comparison to the HERACLES/CMFGEN model grid comes with some assumptions about the physics of the explosion and CSM structure/origin. For the former, this present grid only explores one progenitor mass/radius and explosion energy, which could have an effect on observables such as t_{rise} and M_{peak} ; future HERACLES/CMFGEN grids will explore this parameter space in more detail. For the latter, some models in the present grid assume a homogeneous, spherically symmetric CSM with a wind-like density profile, all of which could be potential sources of uncertainty in extracting true mass-loss rates from the present sample. However, some models (e.g., from Dessart et al. 2023) have varying CSM scale heights as well as different degrees of CSM acceleration. Additionally, the present model grid uses a CSM composition typical of $15 M_{\odot}$ RSGs (Davies & Dessart 2019), which could be varied in future models.

We are also aware of CSM asymmetries from polarization measurements of SNe II during the photoionization phase

(e.g., SN 1998S, Leonard et al. 2000; SN 2023ixf, Vasylyev et al. 2023), which suggest that, there, the CSM is denser along certain lines of sight. Such a physical picture could account for discrepancies between the mass-loss rates inferred from the fastest detectable $\text{H}\alpha$ velocities (e.g., Figure 12) and those estimated from the model grid for Class 1/2 objects in the gold/silver samples. In this case, high mass-loss rates (e.g., $\sim 10^{-2} M_{\odot} \text{ yr}^{-1}$) could still be inferred from electron scattering of recombination photons in dense parts of CSM, while lower-density material along different lines of sight would still allow typical ejecta velocities of $\sim 10^4 \text{ km s}^{-1}$, with little to no deceleration by dense CSM. This physical picture may also be able to explain the discrepancies in the derived mass-loss rates between UV/optical versus X-ray/radio observations of SN 2023ixf (Berger et al. 2023; Chandra et al. 2024; Grefenstette et al. 2023; Jacobson-Galán et al. 2023; Matthews et al. 2023; Nayana et al. 2024, in prep.). Furthermore, a deviation from a steady-state CSM density profile ($\rho \propto r^{-2}$) in these models may be necessary to adequately match the early time light-curve slope (e.g., SN 2023ixf; Jacobson-Galán et al. 2023; Hiramatsu et al. 2023). For example, SBO from close-in ($r < 10^{14}$ cm) high-density CSM as in the SNEC model grid (e.g., Section 4.2) followed by interaction with lower-density material would yield both the fast-rising, luminous light curves and the observation of IIn-like features in some SNe II.

5.3. Implications of Photometry-only Modeling

As shown in Figure 18, the extraction of SN II mass-loss-rate information can yield discrepant results if photometric information is used independently from early time spectroscopic observations. Here, CSM densities inferred from light-curve matching using a grid of SNEC models (Haynie & Piro 2021) are too high to allow for the escape of recombination-line photons in the CSM and the formation of IIn-like features. Consequently, without early time spectroscopy, calculated mass-loss rates and densities close-in to the RSG progenitor (e.g., $< 10^{15}$ cm) may be inconsistent with the presence of narrow emission lines in CSM-interacting SNe II. Similarly, some studies invoke large CSM masses of

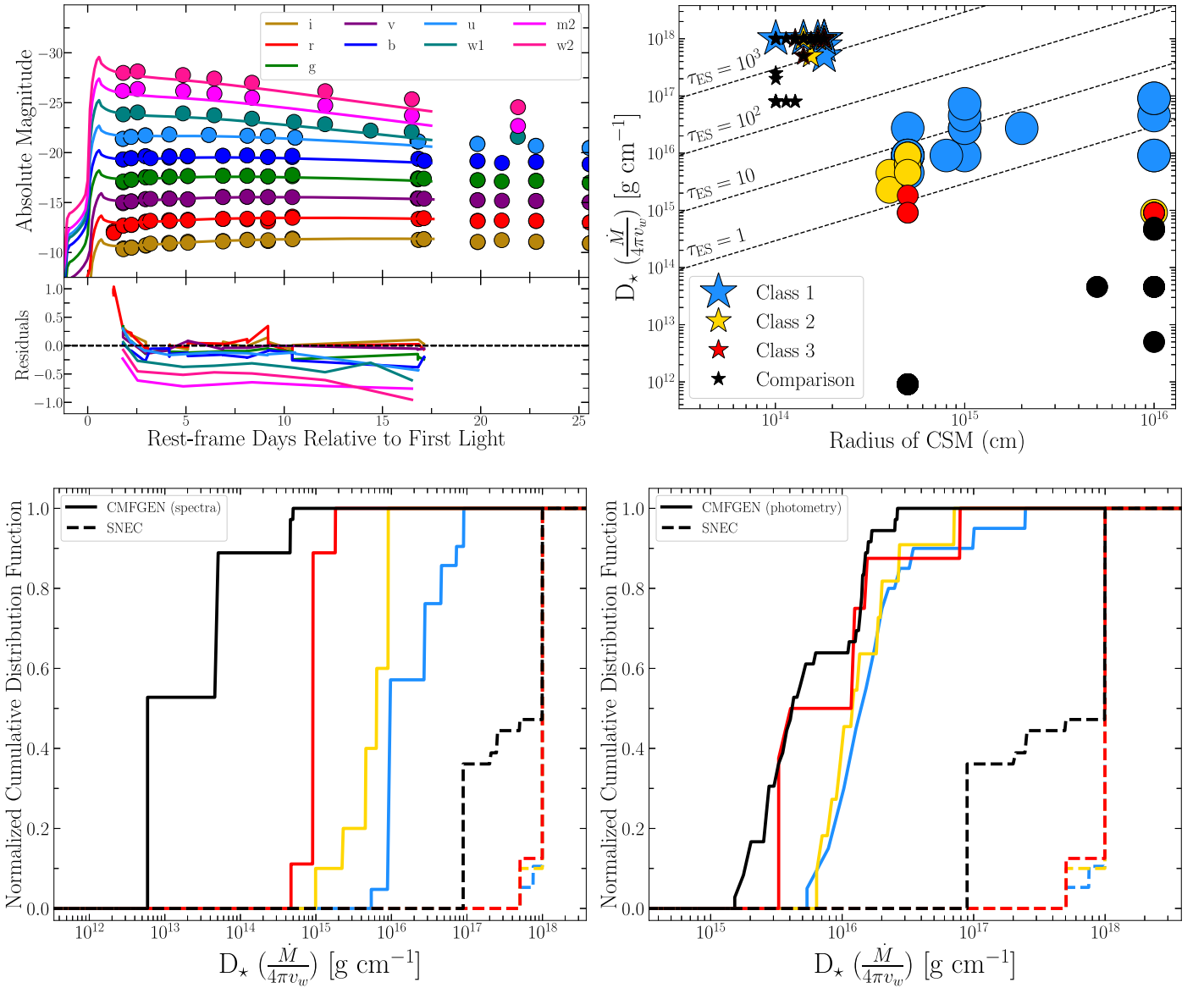


Figure 18. Top left: Multiband photometry of Class 2 gold-sample object SN 2022jox compared to the most consistent CSM interaction model from the grid presented by Haynie & Piro (2021). Despite the overall match to the photometry, the high CSM densities (e.g., $\rho_{14} \approx 10^{-10} \text{ g cm}^{-3}$) required by this model would not allow for the formation of the IIn-like features observed in SN 2022jox. Specifics of model matching for the complete sample are presented in Section 4.2. Top right: Mass-loading parameter (D_\star) vs. CSM radius from the best-matched Haynie & Piro (2021) model for all gold/silver- (blue, yellow, and red stars) and comparison- (black stars) sample objects. Shown as circles are the best-matching CMFGEN models for the gold and comparison samples, which can reproduce both the high peak luminosities and the formation of IIn-like features in the optical spectra. Electron-scattering optical depths shown as dashed lines. Bottom left: cumulative distribution of D_\star values derived from SNEC photometric (dashed lines) and CMFGEN spectral (solid lines) model matching. Bottom right: cumulative distribution of D_\star values derived from SNEC (dashed lines) and CMFGEN (solid lines) model matching to photometry only.

$\sim 0.1\text{--}0.5 M_\odot$, confined to $<10^{14}$ cm, in order to match model light curves to early time SNe II observations (Morozova et al. 2017; Tinyanont et al. 2022; Subrayan et al. 2023). However, as shown by Dessart & Jacobson-Galán (2023), reproducing the enhanced peak UV/optical luminosity in some early time SNe II light curves can also be accomplished with $\sim 10\%$ of these CSM masses. Nevertheless, the early time light curves of some SNe II may be influenced by high-density, extended mass, but such explosions can only display IIn-like features during these phases if there are also regions of lower-density material via CSM asymmetry or inhomogeneity. It is likely that there is a combination of effects present: (1) SBO from extended envelope and/or high-density CSM located at $<2R_\star$ (e.g., Haynie & Piro 2021), and (2) an interaction with lower-density CSM that results in the formation of IIn-like features and increased luminosity. A similar picture is

proposed in Irani et al. (2023) from the light-curve modeling of SNe II with and without IIn-like features, the former requiring larger breakout radii than the latter. Furthermore, it is worth noting that large amounts of spherically symmetric CSM will cause significant deceleration to the fastest moving SN ejecta; this is an observable that could confirm the existence of such CSM properties (Hillier & Dessart 2019). Overall, the combination of photometric and spectroscopic modeling is essential in order to probe both high- and low-density components of CSM in SNe II.

6. Conclusions

In this paper, we have presented UVOIR observations and modeling of the largest sample to date of SNe II with spectroscopic evidence for CSM interaction. Below, we

summarize the primary observational findings from our sample analysis.

1. Our sample consists of 39 SNe II whose early time (“flash”) spectroscopy shows transient, narrow emission lines with electron-scattering wings (i.e., IIn-like) from the photoionization of dense, confined CSM. The total gold/silver sample contains 39 SNe II, 27 of which are unpublished, and includes 501 total spectra (293 previously unpublished) and 39 UVOIR light curves (27 previously unpublished). The IIn-like features persist on a characteristic timescale (t_{In}), which signals a transition in CSM density and the emergence of Doppler-broadened features from the fast-moving SN ejecta.
2. Within the total 74 objects, the “gold” sample contains 20 SNe with both early time IIn-like features, complete UV coverage with Swift-UVOT, and spectral observations at $\delta t < 2$ days. The “silver” sample contains 19 SNe that have detectable IIn-like features, complete UV coverage with Swift-UVOT, and spectral observations only at $\delta t > 2$ days. We divide the gold/silver samples into three classes based on their early time ($t < 3$ day) spectra: Class 1 shows high-ionization lines of He II, N III, and C IV (e.g., SNe 1998S, 2020pni, 2020tlf, 2023ixf, etc), Class 2 shows high-ionization lines He II and C IV but not N III (e.g., SNe 2014G, 2022jox), and Class 3 shows only weak He II (e.g., SN 2013fs). Additionally, we include a “comparison” sample of 35 SNe II that have optical spectra at $t < 2$ days with no IIn-like features as well as a complete UV/optical light curve. Furthermore, Class 1 objects show the longest IIn-like feature timescales (i.e., $t_{\text{In}} \approx 2\text{--}14$ days), while Class 2 and 3 objects displayed shorter-lived emission lines of $t_{\text{In}} < 4$ days and $t_{\text{In}} < 2$ days, respectively. We interpret this diversity as arising from variations in CSM extent and density: Class 1 objects arise from RSGs with more extended, higher-density CSM than Class 2/3 or the comparison samples.
3. We find a significant contrast between the peak optical and pseudobolometric luminosities in the gold versus comparison samples. We also identify clear correlations between peak UV/optical luminosity and both rise time and t_{In} . Furthermore, as discussed in Section 3.1, logrank tests on these observables reveal that the peak pseudobolometric and optical luminosities of both samples are likely derived from separate distributions. The difference between subsamples remains statistically significant after a distance cut ($D > 40$ Mpc) is applied.
4. We apply a grid of ejecta/CSM interaction models, generated with the CMFGEN and HERACLES codes, to extract best-matching mass-loss rates and CSM densities for the gold, silver, and comparison samples. Based on three independent model-matching procedures, we find a continuum of RSG mass-loss rates that extends from $\sim 10^{-6}$ to $10^{-1} M_{\odot} \text{ yr}^{-1}$. From this model set, we derive an approximate relation between the duration of the electron-scattering broadened line profiles and inferred mass-loss rate: $t_{\text{In}} \approx 3.8[\dot{M}/(0.01 M_{\odot} \text{ yr}^{-1})]$ days.

Beyond the early time data presented in this work, future studies (e.g., “Final Moments III-”) will explore the progenitor and explosion properties of this sample through modeling of their late-time photometric and spectroscopic evolution, as well

as multiwavelength (e.g., X-ray/radio) observations. Now that a sample of SNe II with IIn-like features has been compiled and examined in detail, it is essential to create new, high-resolution grids of HERACLES/CMFGEN simulations that can be used together to constrain the CSM properties of such events. Future model grids will provide a more accurate coverage of the CSM interaction parameter space and uncover deficiencies in our model approach (e.g., asymmetries, multidimensional effects, etc.). Furthermore, it is important to build spectroscopically complete, volume-limited surveys that will include systematically discover and classify SNe II within days of first light, therefore reducing biases in follow-up observations and subsequent modeling of certain events. Such discovery efforts will enable volumetric rate measurements of enhanced mass loss in the final years of RSG evolution.

Acknowledgments

Research at UC Berkeley is conducted on the territory of Huichin, the ancestral and unceded land of the Chochoyeno speaking Ohlone people, the successors of the sovereign Verona Band of Alameda County. Keck I/II, ATLAS, and PS1 observations were conducted on the stolen land of the kānaka ‘ōiwi people. We stand in solidarity with the Pu‘uhonua o Pu‘uhuluhulu Maunakea in their effort to preserve these sacred spaces for native Hawai‘ians. MMT observations were conducted on the stolen land of the Tohono O‘odham and Hia-Ced O‘odham nations; the Ak-Chin Indian Community, and Hohokam people. ZTF observations were conducted on the stolen land of the Pauma and Cupeño tribes; the Kumeyaay Nation and the Payómkawichum (Luiseño) people. Shane 3 m observations were conducted on the stolen land of the Ohlone (Costanoans), Tamyen, and Muwekma Ohlone tribes.

We thank Nathan Smith, David Sand, and Avishay Gal-Yam for valuable discussions, and Viktoriya Morozova for providing the initial SNEC models. IRAF is distributed by NOAO, which is operated by AURA, Inc., under cooperative agreement with the NSF.

The Young Supernova Experiment and its research infrastructure are supported by the European Research Council under the European Union’s Horizon 2020 research and innovation programme (ERC grant agreement No. 101002652, PI K. Mandel), the Heising-Simons Foundation (2018-0913, PI R. Foley; 2018-0911, PI R. Margutti), NASA (NNG17PX03C, PI R. Foley), NSF (AST-1720756, AST-1815935, PI R. Foley), the David & Lucille Packard Foundation (PI R. Foley), VILLUM FONDEN (project No. 16599, PI J. Hjorth), and the Center for AstroPhysical Surveys (CAPS) at NCSA and the University of Illinois Urbana-Champaign.

W.J.-G. is supported by the National Science Foundation (NSF) Graduate Research Fellowship Program under grant DGE-1842165. W.J.-G. acknowledges NASA grants in support of Hubble Space Telescope programs GO-16075 and GO-16500. This research was supported in part by the NSF under grant PHY-1748958. The Margutti team at UC Berkeley is partially funded by the Heising-Simons Foundation under grants No. 2018-0911 and No. 2021-3248 (PI R. Margutti). R.C. acknowledges support from NASA Swift grant 80NSSC22K0946.

C.D.K. is partly supported by a CIERA postdoctoral fellowship. A. Haynie is supported by the USC-Carnegie Graduate Fellowship. D.L. was supported by a VILLUM FONDEN Investigator grant (project No. 16599). C.G. is supported by a VILLUM FONDEN Young Investigator grant

(project No. 25501). This work was funded by ANID, Millennium Science Initiative, ICN12_009. The work of X. W. is supported by the National Natural Science Foundation of China (NSFC grants 12288102 and 12033003) and the New Cornerstone Science Foundation through the XPLOER PRIZE. This work was granted access to the HPC resources of TGCC under the allocation 2021—A0110410554 and 2022—A0130410554 made by GENCI, France. This research was supported by the Munich Institute for Astro-, Particle and BioPhysics (MIAPbP), which is funded by the Deutsche Forschungsgemeinschaft (DFG, German Research Foundation) under Germany's Excellence Strategy - EXC-2094 - 390783311. K.A.B. is supported by an LSSTC Catalyst Fellowship; this publication was thus made possible through the support of grant 62192 from the John Templeton Foundation to LSSTC. The opinions expressed in this publication are those of the authors and do not necessarily reflect the views of LSSTC or the John Templeton Foundation.

A.V.F.'s research group at UC Berkeley acknowledges financial assistance from the Christopher R. Redlich Fund, as well as donations from Gary and Cynthia Bengier, Clark and Sharon Winslow, Alan Eustace, William Draper, Timothy and Melissa Draper, Briggs and Kathleen Wood, and Sanford Robertson (W.Z. is a Bengier-Winslow-Eustace Specialist in Astronomy, T.G.B. is a Draper-Wood-Robertson Specialist in Astronomy, and Y.Y. was a Bengier-Winslow-Robertson Fellow in Astronomy). Numerous other donors to his group and/or research at Lick Observatory include Michael and Evelyn Antin, Shawn Atkisson, Charles Baxter and Jinee Tao, Duncan and Catherine Beardsley, Marc and Cristina Bensadoun, Frank and Roberta Bliss, Ann and Gordon Brown, Tina and Greg Butler, Alan and Jane Chew, Curt Covey, Byron and Allison Deeter, Arthur and Cindy Folker, Peter and Robin Frazier, Ellen Fujikawa, Heidi Gerster, Harvey Glasser, John Gnuse, George and Allison Good, Charles and Gretchen Gooding, Thomas and Dana Grogan, Alan Gould and Diane Tokugawa, Timothy and Judi Hachman, Michael and Virginia Halloran, Robert and Tina Hinckley, Alan and Gladys Hofer, Jeff and Allison Holland, Jerry and Patti Hume, the Hugh Stuart Center Charitable Trust, James and Zem Joaquin, Joel Krajweski, Walter and Karen Loewenstern, Gregory Losito and Veronica Bayduza, Art and Rita Levinson, Jesse Levinson, Herbert Masters III, Bruce and Judith Moorad, Rand Morimoto and Ana Henderson, James and Marie O'Brien, Douglas and Emily Ogden, Jim Ostendorf, Garry Parton, Edward and Ellin Purdom, Jonathan and Susan Reiter, Margaret Renn, Paul Robinson, Catherine Rondeau, Eric Rudney, Stanley and Miriam Schiffman, Thomas and Alison Schneider, Ajay Shah and Lata Krishnan, Bruce and Debby Smith, Hans Spiller Justin and Seana Stephens, Charles and Darla Stevens, David and Joanne Turner, Rolf Weber, Gerald and Virginia Weiss, Byron and Nancy Wood, Weldon Wood, Richard Wylie, David and Angie Yancey, and Thomas Zdeblick.

The TRex team at UC Berkeley is supported in part by the NSF under grants AST-2221789 and AST-2224255, and by the Heising-Simons Foundation under grant No. 2021-3248 (PI R. Margutti).

M.R.D. acknowledges support from the NSERC through grant RGPIN-2019-06186, the Canada Research Chairs Program, and the Dunlap Institute at the University of Toronto. This research was supported by the Munich Institute for Astro-, Particle and BioPhysics (MIAPbP), which is funded by the

Deutsche Forschungsgemeinschaft (DFG, German Research Foundation) under Germany's Excellence Strategy - EXC-2094 - 390783311. V.A.V. acknowledges support by the NSF under grant AST-2108676. C.R.A. was supported by grants from VILLUM FONDEN (project Nos. 16599 and 25501). Parts of this research were supported by the Australian Research Council Centre of Excellence for All Sky Astrophysics in 3 Dimensions (ASTRO 3D), through project No. CE170100013. The UCSC team is supported in part by NASA grant 80NSSC20K0953, NSF grant AST-1815935, the Gordon & Betty Moore Foundation, the Heising-Simons Foundation, and by a fellowship from the David and Lucile Packard Foundation to R.J.F.

Based in part on observations made with the Nordic Optical Telescope, owned in collaboration by the University of Turku and Aarhus University, and operated jointly by Aarhus University, the University of Turku and the University of Oslo, representing Denmark, Finland, and Norway, the University of Iceland and Stockholm University at the Observatorio del Roque de los Muchachos, La Palma, Spain, of the Instituto de Astrofísica de Canarias. Observations were obtained under program P62-507 (PI: Angus).

This work includes data obtained with the Swope telescope at Las Campanas Observatory, Chile, as part of the Swope Time Domain Key Project (PI A. Piro; CoIs Coulter, Drout, Phillips, Holoién, French, Cowperthwaite, Burns, Madore, Foley, Kilpatrick, Rojas-Bravo, Dimitriadis, Hsiao). We thank Abdo Campillay, Yilin Kong-Riveros, Piera Soto-King, and Natalie Ulloa for observations on the Swope telescope.

Some of the data presented herein were obtained at the W.M. Keck Observatory, which is operated as a scientific partnership among the California Institute of Technology, the University of California, and NASA. The Observatory was made possible by the generous financial support of the W.M. Keck Foundation. The authors wish to recognize and acknowledge the very significant cultural role and reverence that the summit of Maunakea has always had within the indigenous Hawaiian community. We are most fortunate to have the opportunity to conduct observations from this mountain. A major upgrade of the Kast spectrograph on the Shane 3 m telescope at Lick Observatory, led by Brad Holden, was made possible through generous gifts from the Heising-Simons Foundation, William and Marina Kast, and the University of California Observatories. Research at Lick Observatory is partially supported by a generous gift from Google.

Based in part on observations obtained with the Samuel Oschin 48 inch Telescope at the Palomar Observatory as part of the Zwicky Transient Facility project. ZTF is supported by the NSF under grant AST-1440341 and a collaboration including Caltech, IPAC, the Weizmann Institute for Science, the Oskar Klein Center at Stockholm University, the University of Maryland, the University of Washington, Deutsches Elektronen-Synchrotron and Humboldt University, Los Alamos National Laboratories, the TANGO Consortium of Taiwan, the University of Wisconsin at Milwaukee, and the Lawrence Berkeley National Laboratory. Operations are conducted by the Caltech Optical Observatories (COO), the Infrared Processing and Analysis Center (IPAC), and the University of Washington (UW).

The Pan-STARRS1 Surveys (PS1) and the PS1 public science archive have been made possible through contributions by the Institute for Astronomy, the University of Hawaii, the Pan-STARRS Project Office, the Max-Planck Society and its

participating institutes, the Max Planck Institute for Astronomy, Heidelberg and the Max Planck Institute for Extraterrestrial Physics, Garching, The Johns Hopkins University, Durham University, the University of Edinburgh, the Queen’s University Belfast, the Harvard-Smithsonian Center for Astrophysics, the Las Cumbres Observatory Global Telescope Network Incorporated, the National Central University of Taiwan, STScI, NASA under grant NNX08AR22G issued through the Planetary Science Division of the NASA Science Mission Directorate, NSF grant AST-1238877, the University of Maryland, Eotvos Lorand University (ELTE), the Los Alamos National Laboratory, and the Gordon and Betty Moore Foundation.

This work makes use of observations taken by the Las Cumbres Observatory global telescope network. The Las Cumbres Observatory Group is funded by NSF grants AST-1911225 and AST-1911151. The new SALT data presented here were obtained through Rutgers University program 2022-1-MLT-004 (PI S. Jha). Funding for the Lijiang 2.4 m telescope has been provided by the CAS and the People’s Government of Yunnan Province.

We are grateful to the staffs at the various observatories where data were obtained. We thank S. Bradley Cenko, Thomas de Jaeger, Ori Fox, Melissa Graham, Goni Halevi, Michael Kandrashoff, Patrick Kelly, Io Kleiser, Jon Mauerhan, Adam Miller, Sarafina Nance, Kishore Patra, Neil Pichay, Anthony Rodriguez, Isaac Shivvers, Jeffrey Silverman, Benjamin Stahl, Erika Strasburger, Heechan Yuk, and Sameen Yunus for assistance with some of the Lick/Shane/Kast observations or reductions. The following U.C. Berkeley undergraduate students helped with the Lick/Nickel observations: Raphael Baer-Way, Sanyum Channa, Teagan Chapman, Nick Choksi, Maxime de Kouchkovsky, Nachiket Girish, Goni Halevy, Andrew Halle, Romain Hardy, Andrew Hoffman, Benjamin Jeffers, Connor Jennings, Sahana Kumar, Evelyn Liu, Emma McGinness, Jeffrey Molloy, Yukei Murakami, Andrew Rikhter, Timothy Ross, Jackson Sipple, Samantha Stegman, Haynes Stephens, James Sunseri, Kevin Tang, and Sameen Yunus.

Facility: NASA Neil Gehrels Swift Observatory Mission, Zwicky Transient Facility, ATLAS, YSE/PS1, Lick/Shane (Kast), Lick/Nickel, MMT (Binospec), Keck I/II (LRIS, DEIMOS), Las Cumbres Observatory, TESS.

Software: IRAF (Tody 1986, 1993), photpipe (Rest et al. 2005), DoPhot (Schechter et al. 1993), HOTPANTS (Becker 2015), HEASoft (v6.22), YSE-PZ (Coulter et al. 2022, 2023), CMFGEN (Hillier & Dessart 2012; Dessart et al. 2015), HERACLES (González et al. 2007; Vaytet et al. 2011; Dessart et al. 2015).

Appendix

Here, we present SN properties for all gold-, silver-, and comparison-sample objects in Table A1. Model properties for all HERACLES/CMFGEN simulations are listed in Table A2. In Tables A3 and A4, we present photometric properties of all gold- and comparison-sample objects after correcting for MW and host reddening. Table A5 gives gold- and comparison-sample peak luminosity and rise-time distributions. Spectroscopic properties of the gold sample are listed in Table A6. In Table A7, we present best-matching model parameters for all gold-, silver-, and comparison-sample objects. Logs of optical/NIR spectroscopic observations of all unpublished gold-, silver-, and comparison-sample objects are provided in Table A8. All multicolor/bolometric light curves, spectral sequences, and best-matching light-curve and spectral models are shown for each gold-, silver-, and comparison-sample object in the supplementary pages.⁵⁰

Early-time comparison-sample spectra are shown in Figure A1. In Figure A2, we present the redshift distribution and examples of extinction correction methods. In Figure A3, we present absolute magnitudes versus host extinction. In Figure A4, we present colors as a function of SN phase for the complete sample. In Figure A5, we present peak absolute magnitude as a function of SN distance. In Figure A6, we present comparisons of model matching methods.

Table A1
Gold, Silver, and Comparison-sample Objects

Name	Time of First Light (MJD)	Host Galaxy	Redshift z	Distance (Mpc)	$E(B - V)_{\text{MW}}$ (mag)	$E(B - V)_{\text{host}}$ (mag)	References
Gold Sample							
PTF10gva	55320.3 ± 0.9	SDSS J122355.39 +103448.9	0.028	114.5 ± 8.0^c	0.026	<0.007	Khazov et al. (2016)
PTF11iqb	55764.4 ± 1.0	NGC 151	0.013	50.4 ± 3.5^d	0.028	<0.003	Smith et al. (2015)
2013fs	56571.11 ± 0.02	NGC 7610	0.012	50.6 ± 0.9^c	0.035	0.02 ± 0.004	Yaron et al. (2017)
2017ahn	57791.8 ± 0.5	NGC 3318	0.0090	33.0 ± 6.5^d	0.068	0.21 ± 0.04	Tartaglia et al. (2021) ^a
2018zd	58178.4 ± 0.2	NGC 2146	0.0030	18.4 ± 4.5^d	0.085	0.17 ± 0.03	
2018fif	58350.3 ± 0.2	UGC 00085	0.017	73.8 ± 5.2^c	0.094	0.18 ± 0.04	Soumagnac et al. (2020)
2018dfc	58302.3 ± 0.9	SDSS J164807.68 +241815.4	0.037	153.5 ± 10.7^c	0.072	0.14 ± 0.03	Bruch et al. (2021b)
2019ust	58799.8 ± 0.5	UGC 00548	0.022	92.2 ± 6.5^c	0.053	0.28 ± 0.06	Bruch et al. (2019)
2020pni	59045.8 ± 0.1	UGC 09684	0.017	73.7 ± 1.3^c	0.017	0.18 ± 0.04	Terreran et al. (2022)
2020sic	59092.2 ± 0.9	NGC 6001	0.033	140.3 ± 9.8^c	0.026	0.34 ± 0.07	Schulze et al. (2020)
2020abjq	59183.4 ± 1.0	UGC 00678	0.018	75.5 ± 5.3^c	0.022	0.11 ± 0.02	Burke et al. (2020)
2020lfn	58995.8 ± 0.4		0.044	196.8 ± 4.6^c	0.061	0.08 ± 0.02	Izzo et al. (2020)

⁵⁰ https://github.com/wynnjacobson-galan/Flash_Spectra_Sample

Table A1
(Continued)

Name	Time of First Light (MJD)	Host Galaxy	Redshift z	Distance (Mpc)	$E(B - V)_{\text{MW}}$ (mag)	$E(B - V)_{\text{host}}$ (mag)	References
		SDSS J162656.94 +201447.8					
2021can	59251.8 ± 0.4	SDSS J125530.88 +300142.3	0.0207	90.1 ± 2.3^c	0.010	0.13 ± 0.03	Bruch (2021)
2021jtt	59318.7 ± 0.4	NGC 2955	0.023	109.6 ± 10.1^c	0.009	0.39 ± 0.08	Angus et al. (2021)
2021mqh	59351.3 ± 0.9	MCG-01-30-021	0.021	88.1 ± 6.2^c	0.039	<0.01	Tinyanont et al. (2021b)
2021aaqn	59492.9 ± 0.5	UGC 02119	0.028	115.5 ± 8.1^c	0.034	0.20 ± 0.04	Taggart et al. (2021b)
2022ffg	59663.8 ± 0.6	CGCG 093-074	0.012	50.7 ± 3.6^c	0.034	0.17 ± 0.03	Pellegrino et al. (2022)
2022ibv	59690.5 ± 0.4	ESO 437-G064	0.014	57.5 ± 4.1^c	0.05	0.07 ± 0.02	Siebert & Jacobson-Galan (2022)
2022jox	59706.9 ± 1.3	ESO 435-G014	0.0089	38.0 ± 7.5^d	0.08	0.09 ± 0.02	Andrews et al. (2024)
2022pgf	59782.0 ± 0.3	NGC 5894	0.0082	44.3 ± 8.8^d	0.01	0.49 ± 0.10	Tucker (2022)
		Silver Sample					
PTF10abyy	55532.0 ± 0.5	WISEA J051639.83 +064740.8	0.030	123.6 ± 8.6^c	0.150	<0.09	Khazov et al. (2016)
2014G	56669.6 ± 1.7	NGC 3448	0.0043	24.5 ± 9.0^d	0.01	0.29 ± 0.06	Terreran et al. (2016)
2015bf	57367.8 ± 1.2	NGC 7653	0.014	60.1 ± 1.4^d	0.059	0.19 ± 0.04	Lin et al. (2021)
2016blz	57485.5 ± 3.0	ECO 0866	0.012	51.4 ± 3.6^c	0.09	0.12 ± 0.024	Johansson et al. (2016)
2019qch	58739.0 ± 0.1	WISEA J182914.07 +410228.6	0.024	105.7 ± 4.5^c	0.1	<0.1	Fremling et al. (2019)
2020abtf	59184.9 ± 0.4	SDSS J075934.54 +151759.6	0.014	61.2 ± 4.4^c	0.029	0.09 ± 0.02	Anderson et al. (2020)
2020xua	59142.3 ± 1.1	UGC 12218	0.021	90.4 ± 6.3^c	0.075	0.08 ± 0.02	Terreran et al. (2020)
2020ilf	59098.7 ± 1.5^b	NGC 5731	0.0084	36.8 ± 1.3^c	0.014	0.02 ± 0.01	Jacobson-Galán et al. (2022)
2020nif	59022.3 ± 1.1	NGC 4939	0.010	43.85 ± 8.7^d	0.035	0.19 ± 0.04	Hiramatsu et al. (2020b)
2021wvd	59448.3 ± 0.5	CGCG 077-028	0.045	187.8 ± 13.1^c	0.036	<0.087	Terwel et al. (2021)
2021zj	59222.4 ± 0.6	SDSS J111632.91 +290546.5	0.046	190.5 ± 13.3^c	0.036	<0.032	Smith et al. (2021a)
2021aek	59226.5 ± 1.1	I SZ 091	0.022	90.9 ± 6.4^c	0.041	0.36 ± 0.10	Smith et al. (2021b)
2021dbg	59257.1 ± 0.7	MCG-01-24-014	0.020	83.1 ± 5.9^c	0.027	0.18 ± 0.08	Zhang et al. (2021a)
2021ont	59364.4 ± 0.1	WISE J162642.49 +390842.7	0.028	120.5 ± 8.4^c	0.008	0.14 ± 0.03	Bruch et al. (2021a)
2021qvr	59385.6 ± 1.9	NGC 7678	0.012	45.9 ± 5.3^d	0.042	0.15 ± 0.03	Pellegrino et al. (2021)
2021tyw	59413.4 ± 1.0	UGC 12354	0.013	51.5 ± 4.7^d	0.198	<0.03	Delgado et al. (2021a)
2021afkk	59540.9 ± 0.4	UGC 01971	0.014	63.6 ± 4.5^c	0.09	0.08 ± 0.02	Zhang et al. (2021b)
2022dml	59634.0 ± 1.5	WISEA J161729.19 +142507.4	0.03	132.8 ± 4.5^c	0.044	0.07 ± 0.01	Burke et al. (2022)
2022prv	59780.8 ± 1.5	IC 1132	0.015	65.7 ± 4.6^c	0.052	<0.009	Taggart et al. (2022)
		Comparison Sample					
2013ft	56546.8 ± 1.0	NGC 7732	0.0096	34.2 ± 7.1^d	0.047	<0.037	Khazov et al. (2016)
2013ab	56339.5 ± 1.0	NGC 5669	0.0046	24.0 ± 0.9^d	0.023	0.11 ± 0.020	Bose et al. (2015)
2013am	56371.5 ± 1.0	M65	0.0030	12.8 ± 2.4^d	0.02	0.49 ± 0.090	^e
2016X	57405.9 ± 0.5	UGC 08041	0.0044	15.2 ± 3.0^d	0.02	<0.007	Huang et al. (2018)
2016aqf	57443.6 ± 1.0	NGC 2101	0.004	10.8 ± 1.4^d	0.047	0.03 ± 0.006	Müller-Bravo et al. (2020)
2017eaw	57885.7 ± 0.1	NGC 6946	0.0013	6.70 ± 0.15^d	0.30	0.04 ± 0.01	^f
2017gmr	57999.1 ± 0.5	NGC 988	0.0050	19.6 ± 1.4^d	0.024	0.32 ± 0.070	^g
2018lab	58480.4 ± 0.1	IC 2163	0.0089	32.8 ± 0.4^d	0.075	0.39 ± 0.09	Pearson et al. (2023)
2018kpo	58475.96 ± 0.4	MCG-01-10-019	0.0175	70.0 ± 4.9^c	0.047	<0.009	Prentice et al. (2018)
2018cuf	58291.8 ± 0.6	IC 5092	0.011	41.8 ± 5.8^c	0.027	0.27 ± 0.06	Dong et al. (2021)
2019edo	58599.8 ± 0.5	NGC 4162	0.0086	42.1 ± 8.3^c	0.030	<0.01	Tsvetkov et al. (2022)
2019nvm	58713.7 ± 0.4	UGC 10858	0.018	79.3 ± 5.3^c	0.026	0.21 ± 0.040	Hiramatsu et al. (2019)
2019pjs	58729.7 ± 0.5	UGC 11105	0.007	34.7 ± 2.4^c	0.092	<0.029	Burke et al. (2019)
2019enr	58606.3 ± 1.0	NGC 2919	0.0082	40.7 ± 8.1^c	0.025	0.083 ± 0.016	Perley (2019)
2020ekk	58918.7 ± 1.0	UGC 10528	0.011	62.4 ± 4.4^c	0.041	<0.02	Zhang & Wang (2020)
2020fqv	58938.9 ± 0.2	NGC 4568	0.0075	17.3 ± 3.6^d	0.029	0.81 ± 0.18	Tinyanont et al. (2022)
2020jfo	58973.7 ± 0.1	M61	0.0052	14.5 ± 1.3^d	0.019	0.14 ± 0.030	^h
2020mjm	59011.3 ± 0.9	UGC 09299	0.005	29.4 ± 5.8^d	0.037	<0.008	Hiramatsu et al. (2020a)
2020dpw	58904.8 ± 0.7	NGC 6951	0.0048	16.2 ± 3.2^d	0.32	<0.036	Kawabata (2020)
2020acbm	59192.4 ± 0.5	LSBC F831-08	0.022	87.7 ± 6.1^c	0.029	0.08 ± 0.02	Pessi et al. (2020)
2021vaz	59432.2 ± 0.4	NGC 1961	0.013	57.3 ± 4.0^c	0.107	0.18 ± 0.04	Newsome et al. (2021)
2021ass	59230.7 ± 0.6	NGC 0684	0.0118	43.7 ± 4.0^d	0.072	0.12 ± 0.023	Dahiwalé & Fremling (2021)
2021gmj	59292.2 ± 1.0	NGC 3310	0.0034	18.0 ± 1.3^d	0.019	0.11 ± 0.020	ⁱ
2021rhk	59395.3 ± 1.0	ECO 01022	0.022515	94.7 ± 6.6^c	0.021	<0.06	Rojas-Bravo et al. (2021)

Table A1
(Continued)

Name	Time of First Light (MJD)	Host Galaxy	Redshift z	Distance (Mpc)	$E(B - V)_{\text{MW}}$ (mag)	$E(B - V)_{\text{host}}$ (mag)	References
2021uoy	59427.4 ± 1.0	CGCG 453-026	0.0335	139.2 ± 9.7^c	0.052	0.11 ± 0.02	Taggart et al. (2021a)
2021yja	59464.4 ± 0.1	NGC 1325	0.0057	23.4 ± 4.9^d	0.015	0.18 ± 0.040	^j
2021adly	59522.5 ± 1.0	WISEA J112841.67 +350637.6	0.042	176.7 ± 12.4^c	0.018	<0.05	Tinyanont et al. (2021a)
2021apg	59230.5 ± 0.9	UGC 08661	0.027	113.2 ± 7.9^c	0.01	<0.01	Delgado et al. (2021b)
2021gvm	59293.9 ± 0.4	NGC 5185	0.0246	121.9 ± 4.5^d	0.021	0.017 ± 0.003	Kravtsov et al. (2021)
2021ucg	59419.6 ± 0.9	UGC 12188	0.0172	73.7 ± 5.2^c	0.097	<0.0056	Srivastav et al. (2021)
2022inn	59695.3 ± 0.9	UGC 06365	0.0108	48.7 ± 3.4^c	0.013	<0.097	Irani et al. (2022)
2022fuc	59671.4 ± 0.03	NGC 4545	0.0091	33.9 ± 6.7^d	0.01	<0.008	Zimmerman et al. (2022)
2022jzc	59714.3 ± 0.9	NGC 4088	0.0029	12.8 ± 2.5^d	0.017	0.36 ± 0.08	Bruch et al. (2022)
2022ovb	59773.5 ± 0.9	UGC 12005	0.0183	78.2 ± 5.5^c	0.117	<0.014	Deckers et al. (2022)
2022frq	59670.9 ± 0.5	MCG-02-34-054	0.0226	93.3 ± 6.5^c	0.055	0.11 ± 0.022	Newsome et al. (2022)

Notes.^a Zhang et al. (2020), Hiramatsu et al. (2021), and Callis et al. (2021).^b Based on photometric detection. Time of first light used throughout is MJD 59108 based on modeling.^c Distance derived from redshift with peculiar-velocity uncertainties included.^d Redshift-independent distance.^e Zhang et al. (2014) and Tomasella et al. (2018).^f Kilpatrick & Foley (2018) and Szalai et al. (2019).^g Andrews et al. (2019) and Utrobin et al. (2021).^h Sollerman et al. (2021), Teja et al. (2022), Ailawadhi et al. (2023), and Kilpatrick et al. (2023).ⁱ Murai et al. (2024) and Meza Retamal et al. (2024).^j Hosseinzadeh et al. (2022), Vasylyev et al. (2022), and Kozyreva et al. (2022).**Table A2**
Model Properties

Name	t_{in} (days)	$\log_{10}(\dot{M})$ ($M_{\odot} \text{ yr}^{-1}$)	$\log_{10}(\rho_{\text{CSM},14})^a$ (g cm^{-3})	$\log_{10}(R_{\text{CSM}})$ (cm)	M_{CSM} (M_{\odot})	Reference
r1w1h	<0.3	-6.0	-11.6	14.5	0.016	Dessart et al. (2017)
r1w1	<0.1	-6.0	-16.0	15.0	0.0028	Dessart et al. (2017)
r2w1	<0.2	-6.0	-15.0	14.0	0.061	Dessart et al. (2017)
r1w4	1.4	-3.0	-13.0	14.7	0.0056	Dessart et al. (2017)
r1w5h	0.9	-2.5	-12.3	14.5	0.036	Dessart et al. (2017)
r1w5r	1.4	-2.3	-12.3	14.6	0.010	Dessart et al. (2017)
r1w6	3.5	-2.0	-12.0	14.7	0.030	Dessart et al. (2017)
r1w6a	5.5	-2.0	-12.0	14.8	0.044	Jacobson-Galán et al. (2023)
r1w6b	7.0	-2.0	-12.0	14.9	0.059	Jacobson-Galán et al. (2023)
r1w6c	9.0	-2.0	-12.0	15.0	0.072	Jacobson-Galán et al. (2022)
r1w7a	14.0	-1.5	-12.5	15.0	0.21	Jacobson-Galán et al. (2022)
r1w7b	25.0	-1.5	-12.5	15.3	0.40	Jacobson-Galán et al. (2022)
r1w7c	35.0	-1.5	-12.5	15.6	0.75	Jacobson-Galán et al. (2022)
r1w7d	35.0	-1.5	-12.5	15.9	1.5	Jacobson-Galán et al. (2022)
m1em5	<0.1	-5.0	-15.2	16.0	0.0037	Dessart & Jacobson-Galán (2023)
m1em4	<0.2	-4.0	-14.3	16.0	0.0039	Dessart & Jacobson-Galán (2023)
m1em3	1.0	-3.0	-13.3	16.0	0.0056	Dessart & Jacobson-Galán (2023)
m1em2	4.0	-2.0	-11.9	16.0	0.024	Dessart & Jacobson-Galán (2023)
m1em1	15.0	-1.0	-10.9	16.0	0.18	Dessart & Jacobson-Galán (2023)
m1em0	25.0	1.0	-10.1	16.0	1.21	Dessart & Jacobson-Galán (2023)

Note.^a Density at 10^{14} cm.

Table A3
Gold/silver-sample Photometric Properties

Name	$\log_{10}(L_{\text{bol,max}})$ (erg s^{-1})	$M_{W2,\text{max}}$ (mag)	$M_{M2,\text{max}}$ (mag)	$M_{W1,\text{max}}$ (mag)	$M_{U,\text{max}}$ (mag)	$M_{B,\text{max}}$ (mag)	$M_{V,\text{max}}$ (mag)	$M_{g,\text{max}}$ (mag)	$M_{r,\text{max}}$ (mag)
PTF10gva	>43.28	< -18.90	< -18.93	< -18.87	-18.81 ± 0.25	-18.53 ± 0.15
PTF10abyy	>43.49	< -19.80	< -19.96	< -19.67	-19.21 ± 0.17
PTF11iqb	43.46 ± 0.06	-18.80 ± 0.16	-18.94 ± 0.16	-18.86 ± 0.15	-18.37 ± 0.15
2013fs	42.93 ± 0.14	-18.19 ± 0.32	-18.10 ± 0.32	-17.99 ± 0.32	-17.72 ± 0.32	-17.90 ± 0.32	-17.80 ± 0.33	-17.82 ± 0.32	-17.75 ± 0.32
2014G	43.15 ± 0.32	-18.75 ± 0.80	-19.14 ± 0.80	-18.72 ± 0.80	-18.77 ± 0.80	-18.56 ± 0.80	-18.47 ± 0.80	-18.54 ± 0.80	-18.47 ± 0.80
2015bf	43.05 ± 0.02	< -18.97	< -19.29	-18.77 ± 0.08	-18.72 ± 0.08	-18.43 ± 0.09	-18.39 ± 0.10	...	-18.27 ± 0.07
2016blz	>43.47	< -19.09	< -19.33	< -18.98	< -19.19	< -19.06	-19.07 ± 0.16
2017ahn	43.33 ± 0.17	-18.23 ± 0.43	-18.68 ± 0.43	-18.30 ± 0.43	-18.32 ± 0.43	-18.35 ± 0.43	-18.18 ± 0.43	-18.11 ± 0.45	-17.94 ± 0.43
2018zd	43.28 ± 0.21	-19.15 ± 0.53	-19.35 ± 0.53	-19.01 ± 0.53	-19.06 ± 0.53	-18.76 ± 0.53	-18.48 ± 0.53	-18.65 ± 0.53	-18.37 ± 0.53
2018fif	42.36 ± 0.07	< -17.38	< -17.39	-17.19 ± 0.17	-17.38 ± 0.49	-17.41 ± 0.22	-17.23 ± 0.32	-17.29 ± 0.16	-17.35 ± 0.16
2018dfc	>43.54	< -19.69	< -19.81	< -19.37	< -19.27	-19.12 ± 0.21	...	-18.77 ± 0.15	-18.64 ± 0.15
2019ust	43.59 ± 0.06	-19.99 ± 0.15	-20.09 ± 0.16	-19.56 ± 0.16	-19.29 ± 0.17	-19.10 ± 0.15	-18.85 ± 0.15	-19.09 ± 0.15	-18.58 ± 0.15
2019qch	>43.53	< -17.65	< -18.12	< -18.24	< -18.49	-18.44 ± 0.25	-18.58 ± 0.20	-18.42 ± 0.09	-18.18 ± 0.12
2020pni	43.48 ± 0.07	-19.76 ± 0.13	-19.88 ± 0.11	-19.43 ± 0.10	-19.19 ± 0.08	-18.83 ± 0.09	-18.60 ± 0.10	-18.97 ± 0.04	-18.61 ± 0.04
2020sic	>42.92	< -20.79	< -21.15	< -20.12	-19.84 ± 0.18	-19.00 ± 0.16	-18.30 ± 0.16
2020abtf	>42.99	< -17.71	< -18.00	< -17.72	< -17.77	-17.39 ± 0.16	-17.28 ± 0.16	-17.69 ± 0.16	-17.21 ± 0.28
2020abjq	>43.56	< -20.04	< -19.96	< -19.60	-19.31 ± 0.16	-18.82 ± 0.17	-18.68 ± 0.16	-18.74 ± 0.15	-18.32 ± 0.15
2020xua	42.86 ± 0.07	< -17.91	< -18.20	-18.05 ± 0.17	-18.04 ± 0.17	-17.51 ± 0.17	-17.40 ± 0.18	-17.42 ± 0.16	-17.56 ± 0.15
2020tlf	43.52 ± 0.11	-18.70 ± 0.08	-18.76 ± 0.09	-18.69 ± 0.09	-18.70 ± 0.08	-18.51 ± 0.09	-18.34 ± 0.09	-18.19 ± 0.10	...
2020nif	>43.41	< -19.64	< -19.77	< -19.34	-19.25 ± 0.43	-19.05 ± 0.43	-18.90 ± 0.43	-19.15 ± 0.43	-18.81 ± 0.43
2020lfn	43.23 ± 0.04	-19.80 ± 0.07	-19.86 ± 0.07	-19.58 ± 0.07	-19.51 ± 0.08	-19.07 ± 0.13	-18.81 ± 0.28	-19.22 ± 0.06	-19.32 ± 0.05
2021wvd	>43.43	< -19.27	< -19.32	< -19.33	-19.28 ± 0.17	-19.00 ± 0.23	-18.94 ± 0.31	-18.97 ± 0.19	-19.04 ± 0.15
2021zj	43.50 ± 0.06	-19.02 ± 0.23	-19.09 ± 0.25	-19.07 ± 0.25	-18.86 ± 0.25	-18.71 ± 0.18	-18.81 ± 0.18	-18.83 ± 0.15	-18.35 ± 0.15
2021aek	>43.63	< -19.54	< -19.76	< -19.08	-19.11 ± 0.17	-19.15 ± 0.16	-18.77 ± 0.16	-18.50 ± 0.16	-18.50 ± 0.16
2021can	43.40 ± 0.04	-19.45 ± 0.07	-19.58 ± 0.07	-19.15 ± 0.07	-18.91 ± 0.07	-18.59 ± 0.09	-18.46 ± 0.15	-18.68 ± 0.06	-18.17 ± 0.06
2021dbg	43.53 ± 0.07	< -19.87	< -19.96	-19.53 ± 0.24	-19.59 ± 0.18	-19.42 ± 0.19	-19.27 ± 0.17	-19.18 ± 0.17	-18.97 ± 0.17
2021jtt	>43.91	< -21.14	< -21.70	< -20.52	-19.95 ± 0.33	-19.76 ± 0.36	-19.20 ± 0.32	-19.34 ± 0.21	-18.78 ± 0.21
2021mqh	>43.36	< -18.91	< -18.93	< -18.73	-18.78 ± 0.16	-18.21 ± 0.16	-18.07 ± 0.15	-18.07 ± 0.16	-17.91 ± 0.15
2021ont	43.58 ± 0.09	-19.84 ± 0.16	-20.23 ± 0.15	-19.83 ± 0.15	-19.56 ± 0.15	-19.40 ± 0.15	-18.87 ± 0.26	-19.29 ± 0.15	-18.76 ± 0.15
2021qvr	43.76 ± 0.11	< -19.51	< -19.48	-19.26 ± 0.25	-19.14 ± 0.25	-18.87 ± 0.25	-18.90 ± 0.25	-18.62 ± 0.26	-18.31 ± 0.29
2021tyw	>42.83	< -18.15	< -17.90	< -17.79	-17.67 ± 0.20	-17.94 ± 0.21	-17.68 ± 0.21	-17.80 ± 0.20	-17.56 ± 0.20
2021aaqn	>43.01	< -18.60	< -18.61	< -18.22	-18.24 ± 0.15	-18.20 ± 0.22	-17.67 ± 0.32	-17.80 ± 0.17	-17.61 ± 0.19
2021afkk	>43.41	< -19.81	< -19.49	< -19.29	< -19.41	< -19.22	-19.17 ± 0.19
2022dml	>43.20	< -18.88	< -18.96	< -18.19	-19.32 ± 0.22	-18.93 ± 0.11	-18.74 ± 0.08	-18.90 ± 0.09	-18.50 ± 0.12
2022ffg	43.25 ± 0.07	-19.11 ± 0.16	-19.27 ± 0.16	-18.90 ± 0.16	-18.79 ± 0.16	-18.61 ± 0.16	-18.48 ± 0.17	-18.56 ± 0.16	-18.40 ± 0.16
2022ibv	>42.99	< -18.47	< -18.42	< -18.28	-18.10 ± 0.22	-17.83 ± 0.16	-17.66 ± 0.16	-17.76 ± 0.15	-17.56 ± 0.15
2022jox	42.88 ± 0.17	-18.05 ± 0.43	-18.37 ± 0.43	-18.07 ± 0.43	-18.05 ± 0.43	-17.70 ± 0.43	-17.48 ± 0.44	-17.79 ± 0.44	-17.52 ± 0.43
2022pgf	43.96 ± 0.17	-20.85 ± 0.43	-21.38 ± 0.43	-20.45 ± 0.43	-20.23 ± 0.43	-19.91 ± 0.44	-19.65 ± 0.43	-19.84 ± 0.43	-19.43 ± 0.43
2022prv	43.46 ± 0.07	< -16.71	< -16.75	< -16.72	< -16.98	< -16.82	...	-18.28 ± 0.17	-18.15 ± 0.16

Name	$t_{\text{bol,rise}}$ (days)	$t_{W2,rise}$ (days)	$t_{M2,rise}$ (days)	$t_{W1,rise}$ (days)	$t_{U,rise}$ (days)	$t_{B,rise}$ (days)	$t_{V,rise}$ (days)	$t_{g,rise}$ (days)	$t_{r,rise}$ (days)
PTF10gva	<3.33	<2.93	<2.94	<2.96	2.93 ± 1.05	8.70 ± 0.90
PTF10abyy	<4.12	<4.11	<4.13	<4.10	8.21 ± 0.50
PTF11iqb	4.00 ± 1.15	3.48 ± 1.00	4.01 ± 1.00	4.49 ± 1.00	10.46 ± 1.00

Table A3
(Continued)

Name	$t_{\text{bol,rise}}$ (days)	$t_{\text{W2,rise}}$ (days)	$t_{\text{M2,rise}}$ (days)	$t_{\text{W1,rise}}$ (days)	$t_{\text{U,rise}}$ (days)	$t_{\text{B,rise}}$ (days)	$t_{\text{V,rise}}$ (days)	$t_{\text{g,rise}}$ (days)	$t_{\text{r,rise}}$ (days)
2013fs	1.08 ± 0.09	1.20 ± 0.02	1.64 ± 0.02	2.51 ± 0.02	4.51 ± 0.02	5.56 ± 0.02	6.15 ± 0.12	6.64 ± 0.02	6.64 ± 0.02
2014G	4.06 ± 2.09	3.81 ± 1.70	3.88 ± 1.70	4.10 ± 1.70	5.13 ± 1.70	9.40 ± 1.70	11.67 ± 1.70	10.40 ± 1.70	9.53 ± 1.71
2015bf	2.78 ± 1.48	<3.05	<3.75	3.69 ± 1.20	4.39 ± 1.20	9.45 ± 1.20	12.73 ± 1.20	...	13.19 ± 1.20
2016blz	<2.96	<9.86	<9.86	<9.86	<9.86	<9.86	10.48 ± 2.96
2017ahn	3.80 ± 0.58	4.70 ± 0.50	4.90 ± 0.50	5.27 ± 0.50	5.65 ± 0.50	7.45 ± 0.50	7.78 ± 0.51	7.91 ± 2.26	9.08 ± 0.50
2018zd	7.89 ± 0.20	7.72 ± 0.20	7.99 ± 0.20	8.38 ± 0.20	8.80 ± 0.20	9.00 ± 0.20	10.46 ± 0.25	8.81 ± 0.20	9.26 ± 0.20
2018fif	3.82 ± 1.54	<1.68	<1.72	2.46 ± 0.20	10.06 ± 2.40	10.39 ± 0.52	11.95 ± 1.68	7.49 ± 0.20	18.45 ± 3.74
2018dfc	<2.81	<1.62	<1.59	<1.62	3.30 ± 1.11	3.30 ± 0.97	...	7.00 ± 0.94	13.60 ± 2.10
2019ust	4.26 ± 0.55	3.39 ± 0.50	3.96 ± 0.50	4.09 ± 0.50	5.60 ± 0.51	6.98 ± 0.50	9.25 ± 0.53	7.17 ± 0.53	9.05 ± 0.50
2019qch	<8.43	<15.81	<16.16	<15.81	<15.81	15.80 ± 0.12	16.16 ± 0.10	15.25 ± 0.22	11.96 ± 1.91
2020pni	3.60 ± 0.25	3.74 ± 0.10	3.78 ± 0.10	4.03 ± 0.11	5.54 ± 0.10	5.14 ± 0.14	12.00 ± 0.50	4.82 ± 0.11	13.94 ± 2.36
2020sic	<3.49	<2.03	<2.03	<2.05	3.19 ± 0.90	4.56 ± 0.90	4.88 ± 0.90
2020abtf	<4.04	<7.95	<7.96	<7.95	<7.18	13.66 ± 0.49	15.46 ± 0.80	4.26 ± 0.40	9.73 ± 3.65
2020abjq	<4.57	<3.94	<3.95	<3.94	3.55 ± 1.00	7.51 ± 1.28	9.44 ± 1.13	9.65 ± 1.00	11.60 ± 1.00
2020xua	2.01 ± 1.12	<2.30	<2.31	2.79 ± 1.10	2.94 ± 1.10	9.17 ± 1.11	13.09 ± 3.05	14.52 ± 1.11	7.95 ± 1.92
2020tlf	4.94 ± 2.04	5.68 ± 1.50	6.24 ± 1.50	6.71 ± 1.50	7.84 ± 1.50	8.76 ± 1.50	10.35 ± 1.51	5.08 ± 1.90	...
2020nif	<3.39	<2.87	<2.87	<2.86	8.30 ± 1.12	11.95 ± 1.20	13.74 ± 1.28	21.47 ± 1.10	15.08 ± 1.10
2020lfn	3.73 ± 0.45	2.52 ± 0.40	2.14 ± 0.41	3.16 ± 0.40	3.97 ± 0.40	7.88 ± 0.40	5.73 ± 1.20	7.65 ± 0.41	10.32 ± 0.40
2021wvd	<6.21	<4.06	<3.84	<3.89	6.20 ± 0.52	6.12 ± 1.38	7.69 ± 0.55	5.91 ± 0.60	7.63 ± 0.50
2021zj	5.82 ± 0.65	3.60 ± 0.65	4.93 ± 0.77	4.92 ± 0.66	4.92 ± 0.69	8.17 ± 0.81	7.09 ± 0.82	8.21 ± 0.77	11.26 ± 2.26
2021aek	<3.05	<3.82	<4.89	<3.81	5.67 ± 1.10	6.68 ± 1.10	9.29 ± 1.59	7.00 ± 1.10	10.97 ± 1.38
2021can	3.58 ± 0.44	2.55 ± 0.40	3.01 ± 0.40	3.18 ± 0.40	4.01 ± 0.40	6.03 ± 0.42	8.19 ± 3.23	5.33 ± 0.40	5.47 ± 0.41
2021dbg	7.20 ± 0.86	<5.39	<9.20	5.36 ± 1.20	8.79 ± 1.10	12.67 ± 1.27	12.68 ± 1.36	10.43 ± 1.11	15.32 ± 1.10
2021jtt	<2.00	<1.30	<1.30	<1.29	3.61 ± 0.47	4.54 ± 0.49	8.51 ± 0.43	4.60 ± 0.40	12.94 ± 1.81
2021mqh	<4.17	<2.66	<2.63	<2.65	4.26 ± 0.90	4.18 ± 0.90	6.24 ± 0.90	6.99 ± 1.44	9.39 ± 0.90
2021ont	8.46 ± 0.12	8.05 ± 0.10	8.06 ± 0.10	8.02 ± 0.11	8.38 ± 0.13	13.68 ± 0.14	10.41 ± 0.11	8.82 ± 0.13	11.80 ± 0.86
2021qvr	5.27 ± 2.40	<3.10	<3.07	4.16 ± 1.90	4.50 ± 1.90	9.72 ± 1.90	12.51 ± 1.90	9.74 ± 1.91	13.04 ± 4.06
2021tyw	<12.44	<8.86	<13.50	<13.50	12.69 ± 1.06	14.20 ± 1.00	16.92 ± 1.00	13.95 ± 1.01	14.94 ± 2.53
2021aaqn	<1.88	<1.63	<1.54	<1.63	1.39 ± 0.53	5.09 ± 0.51	5.84 ± 0.50	9.02 ± 1.58	11.44 ± 4.72
2021afkk	<6.91	<5.57	<8.31	<8.31	<8.19	<9.26	12.22 ± 0.40
2022dml	<6.48	<8.16	<8.16	<11.54	6.33 ± 1.67	6.34 ± 1.50	9.47 ± 1.52	9.77 ± 1.85	13.11 ± 1.70
2022ffg	5.05 ± 0.68	3.94 ± 0.60	4.10 ± 0.60	4.33 ± 0.60	7.33 ± 0.60	8.38 ± 0.60	20.76 ± 0.68	16.24 ± 0.66	26.42 ± 0.61
2022ibv	<2.37	<1.81	<2.77	<1.80	2.76 ± 0.52	3.86 ± 0.44	6.47 ± 1.44	5.53 ± 0.40	5.72 ± 0.40
2022jox	2.36 ± 1.44	2.16 ± 1.30	3.22 ± 1.30	3.26 ± 1.30	3.53 ± 1.30	5.51 ± 1.30	8.52 ± 1.30	8.13 ± 1.72	12.81 ± 1.46
2022pgf	10.04 ± 0.39	8.04 ± 0.30	9.06 ± 0.30	9.82 ± 0.30	12.37 ± 0.30	12.35 ± 0.39	15.39 ± 0.32	15.21 ± 0.30	16.05 ± 0.30
2022prv	22.63 ± 1.77	>9.43	>9.44	>9.43	>9.43	>9.43	...	22.23 ± 1.53	23.61 ± 1.56

Table A4
Comparison-sample Photometric Properties

Name	$\log_{10}(L_{\text{bol,max}})$ (erg s^{-1})	$M_{\text{W2,max}}$ (mag)	$M_{\text{M2,max}}$ (mag)	$M_{\text{W1,max}}$ (mag)	$M_{\text{U,max}}$ (mag)	$M_{\text{B,max}}$ (mag)	$M_{\text{V,max}}$ (mag)	$M_{\text{g,max}}$ (mag)	$M_{\text{r,max}}$ (mag)
2013ft	>41.71	< - 14.03	< - 14.05	< - 13.79	< - 14.07	-13.78 ± 0.58	-14.22 ± 0.52	...	-14.69 ± 0.48
2013am	>42.27	< - 14.85	< - 14.90	< - 14.86	< - 15.54	-15.86 ± 0.42	-15.74 ± 0.43	-15.71 ± 0.41	-15.94 ± 0.41
2013ab	42.82 ± 0.04	< - 17.99	< - 18.15	-17.85 ± 0.09	< - 17.93	-17.68 ± 0.08	-17.39 ± 0.08	-17.66 ± 0.08	-17.61 ± 0.09
2016X	42.18 ± 0.17	-16.44 ± 0.43	-16.73 ± 0.43	-16.99 ± 0.43	-17.01 ± 0.43	-16.90 ± 0.43	-16.90 ± 0.43	-16.92 ± 0.43	-16.95 ± 0.43
2016aqf	>41.66	< - 14.79	< - 14.97	< - 14.86	-14.99 ± 0.28	-14.74 ± 0.29	-14.75 ± 0.31	-14.83 ± 0.30	-14.90 ± 0.31
2017eaw	42.39 ± 0.03	< - 18.16	-17.99 ± 0.05	-17.48 ± 0.07	-17.62 ± 0.05	-17.48 ± 0.05	-17.37 ± 0.05	-17.75 ± 0.05	-17.41 ± 0.05
2017gmr	43.18 ± 0.07	< - 19.11	< - 18.96	< - 18.53	-18.47 ± 0.16	-18.44 ± 0.18	-18.26 ± 0.17	-18.35 ± 0.16	-18.25 ± 0.16
2018lab	>42.50	< - 17.72	-17.72 ± 0.11	< - 16.87	-16.50 ± 0.04	-16.25 ± 0.04	-15.67 ± 0.06	-15.90 ± 0.04	-15.65 ± 0.04
2018kpo	>42.55	< - 16.87	< - 17.14	< - 17.10	< - 17.28	< - 17.27	...	-17.20 ± 0.19	-17.26 ± 0.15
2018cuf	42.79 ± 0.13	< - 17.99	-17.88 ± 0.31	< - 17.39	-17.34 ± 0.30	-17.34 ± 0.30	-17.16 ± 0.30	-17.34 ± 0.30	-17.15 ± 0.30
2019edo	42.40 ± 0.17	< - 16.58	< - 16.58	< - 16.53	< - 16.86	-17.03 ± 0.43	-16.91 ± 0.43	-16.90 ± 0.43	-16.84 ± 0.43
2019nvm	43.25 ± 0.07	< - 19.64	< - 19.59	< - 18.89	-18.73 ± 0.21	-18.35 ± 0.15	-17.82 ± 0.31	-18.22 ± 0.18	-18.10 ± 0.19
2019pjs	42.24 ± 0.07	< - 16.26	< - 16.40	< - 16.26	< - 16.34	-16.24 ± 0.23	-16.20 ± 0.21	-16.21 ± 0.16	-16.16 ± 0.15
2019enr	41.56 ± 0.18	< - 13.94	< - 13.69	< - 14.31	-14.64 ± 0.44	-14.88 ± 0.45	-15.20 ± 0.45	-15.27 ± 0.49	-15.28 ± 0.44
2020ekk	>43.01	< - 18.13	< - 18.11	< - 18.00	-17.86 ± 0.19	-17.81 ± 0.17	-17.76 ± 0.16	-17.73 ± 0.16	-17.60 ± 0.16
2020jfo	>42.54	-17.39 ± 0.21	-17.49 ± 0.21	-17.06 ± 0.20	-17.28 ± 0.20	-16.74 ± 0.20	-16.86 ± 0.20	-16.96 ± 0.19	-16.71 ± 0.19
2020fqv	42.57 ± 0.19	< - 18.95	< - 18.20	< - 17.35	-17.38 ± 0.48	-17.68 ± 0.47	-17.54 ± 0.48	-18.00 ± 0.46	-17.79 ± 0.45
2020mjm	42.31 ± 0.18	< - 16.66	< - 16.76	< - 16.60	-16.86 ± 0.43	-16.47 ± 0.43	-16.44 ± 0.43	-16.54 ± 0.43	-16.40 ± 0.43
2020dpw	>41.98	< - 15.47	< - 15.26	< - 15.42	< - 15.24	-15.91 ± 0.43	< - 15.85	-15.62 ± 0.44	-15.91 ± 0.43
2020acbm	43.04 ± 0.07	< - 18.67	< - 18.78	< - 18.39	-18.50 ± 0.16	-18.11 ± 0.20	-18.17 ± 0.22	-17.95 ± 0.20	-17.85 ± 0.15
2021vaz	>42.89	< - 18.11	< - 18.24	< - 17.73	-17.83 ± 0.17	< - 17.58	-17.56 ± 0.18	-17.64 ± 0.15	-17.74 ± 0.31
2021ass	42.09 ± 0.08	< - 15.16	< - 15.44	< - 15.45	< - 16.01	< - 15.82	-16.02 ± 0.21	-15.93 ± 0.21	-16.13 ± 0.22
2021gmj	42.19 ± 0.07	-16.77 ± 0.16	-16.79 ± 0.16	-16.43 ± 0.16	-16.29 ± 0.16	-16.05 ± 0.17	-15.87 ± 0.17	-16.04 ± 0.16	-15.97 ± 0.16
2021rhc	42.67 ± 0.06	< - 17.39	< - 17.46	< - 17.44	-17.61 ± 0.16	-17.53 ± 0.18	-17.83 ± 0.24	-17.50 ± 0.15	-17.63 ± 0.16
2021uoy	>42.92	< - 18.08	< - 18.16	< - 17.84	< - 18.14	< - 17.75	...	-17.98 ± 0.15	-17.86 ± 0.15
2021yja	43.20 ± 0.18	-19.30 ± 0.46	-19.24 ± 0.46	-18.64 ± 0.46	-18.40 ± 0.46	-18.16 ± 0.45	-17.98 ± 0.46	-18.21 ± 0.45	-17.98 ± 0.46
2021adly	43.03 ± 0.08	< - 17.35	< - 17.91	< - 17.62	< - 17.86	< - 17.62	...	-17.70 ± 0.15	-17.34 ± 0.17
2021apg	42.93 ± 0.09	< - 17.25	< - 17.23	< - 17.20	-17.32 ± 0.19	-16.80 ± 0.26	-17.51 ± 0.25	-16.94 ± 0.16	-16.90 ± 0.16
2021gvm	42.94 ± 0.04	< - 18.03	< - 17.85	-17.93 ± 0.11	< - 18.26	< - 18.26	< - 18.40	-18.38 ± 0.08	-18.38 ± 0.08
2021ucg	42.62 ± 0.06	< - 17.09	< - 17.33	< - 17.13	-17.31 ± 0.15	-17.40 ± 0.17	-17.32 ± 0.15	-17.40 ± 0.15	-17.31 ± 0.15
2022inn	41.59 ± 0.06	< - 15.18	< - 15.16	< - 14.94	< - 14.85	< - 15.02	...	-14.59 ± 0.16	-14.56 ± 0.17
2022fuc	42.04 ± 0.17	< - 16.22	-16.10 ± 0.43	-16.04 ± 0.43	-15.92 ± 0.43	-15.94 ± 0.44	-16.14 ± 0.43	-15.95 ± 0.43	-15.95 ± 0.43
2022jzc	41.50 ± 0.18	< - 14.63	< - 15.00	< - 14.43	< - 14.54	-14.35 ± 0.43	-14.72 ± 0.94	-14.35 ± 0.43	-14.16 ± 0.43
2022ovb	42.75 ± 0.07	-18.12 ± 0.16	-18.04 ± 0.16	-17.73 ± 0.16	-17.98 ± 0.17	-17.92 ± 0.17	...	-18.01 ± 0.15	-18.21 ± 0.15
2022frq	>42.86	< - 18.39	< - 18.25	< - 17.91	-17.63 ± 0.15	-17.52 ± 0.15	-17.37 ± 0.19	-17.56 ± 0.16	-17.27 ± 0.19

Name	$t_{\text{bol,rise}}$ (days)	$t_{\text{W2,rise}}$ (days)	$t_{\text{M2,rise}}$ (days)	$t_{\text{W1,rise}}$ (days)	$t_{\text{U,rise}}$ (days)	$t_{\text{B,rise}}$ (days)	$t_{\text{V,rise}}$ (days)	$t_{\text{g,rise}}$ (days)	$t_{\text{r,rise}}$ (days)
2013ft	<1.16	<1.13	<1.16	<1.16	<1.16	9.70 ± 2.43	15.06 ± 1.01	...	15.10 ± 1.01
2013am	<2.90	<2.19	<2.20	<2.17	<2.18	5.38 ± 1.00	9.00 ± 1.03	8.95 ± 1.05	10.55 ± 1.57
2013ab	4.98 ± 1.24	<4.97	<4.97	5.52 ± 1.00	<4.97	6.79 ± 1.00	7.44 ± 1.00	8.46 ± 1.00	8.89 ± 1.01
2016X	7.27 ± 0.56	3.39 ± 0.50	3.56 ± 0.50	5.56 ± 0.50	7.80 ± 0.50	6.59 ± 0.51	9.73 ± 0.50	9.96 ± 0.52	13.56 ± 0.51
2016aqf	<1.56	<1.56	<1.57	<0.87	2.03 ± 1.00	4.10 ± 1.00	62.54 ± 1.00	9.43 ± 1.00	60.49 ± 1.00
2017eaw	3.15 ± 0.11	<1.89	2.13 ± 0.10	2.37 ± 0.10	7.36 ± 0.18	6.80 ± 2.29	7.18 ± 0.11	6.92 ± 0.12	10.65 ± 2.15
2017gmr	1.11 ± 0.57	<2.54	<2.52	<2.53	6.58 ± 0.50	6.71 ± 0.90	9.53 ± 0.51	8.35 ± 0.50	11.08 ± 0.53

Table A4
(Continued)

Name	$t_{\text{bol,rise}}$ (days)	$t_{\text{W2,rise}}$ (days)	$t_{\text{M2,rise}}$ (days)	$t_{\text{W1,rise}}$ (days)	$t_{\text{U,rise}}$ (days)	$t_{\text{B,rise}}$ (days)	$t_{\text{V,rise}}$ (days)	$t_{\text{g,rise}}$ (days)	$t_{\text{r,rise}}$ (days)
2018lab	<1.23	<1.27	1.62 ± 0.10	<1.26	1.72 ± 0.10	1.96 ± 0.33	11.43 ± 0.23	1.52 ± 0.15	11.18 ± 0.11
2018kpo	<5.36	<4.81	<4.70	<4.81	<4.81	4.81 ± 0.46	...	7.53 ± 1.30	7.63 ± 0.41
2018cuf	0.93 ± 0.71	<1.63	1.61 ± 0.56	<1.62	5.36 ± 0.57	9.73 ± 1.39	8.70 ± 1.26	9.54 ± 0.59	11.33 ± 0.59
2019edo	2.57 ± 0.52	<2.11	<2.12	<3.10	<3.96	3.39 ± 0.48	5.46 ± 0.48	3.98 ± 0.48	6.51 ± 0.48
2019nvm	1.92 ± 0.48	<0.85	<0.85	<0.84	4.85 ± 1.41	5.39 ± 0.40	8.66 ± 0.54	7.07 ± 2.99	7.23 ± 2.19
2019pjs	1.59 ± 0.57	<2.46	<2.46	<2.46	4.62 ± 0.52	1.59 ± 0.57	15.72 ± 3.65	4.22 ± 1.86	17.62 ± 3.16
2019enr	1.89 ± 1.20	<2.61	<2.61	<3.21	3.99 ± 1.15	6.72 ± 2.27	9.51 ± 1.03	7.67 ± 2.26	14.02 ± 3.84
2020ekk	<1.69	<2.84	<2.87	<2.83	4.53 ± 1.80	2.33 ± 1.97	7.30 ± 1.15	7.09 ± 1.12	10.51 ± 1.13
2020jfo	<2.51	3.06 ± 0.10	3.21 ± 0.10	3.01 ± 0.10	3.37 ± 0.10	5.77 ± 0.21	7.13 ± 0.26	6.86 ± 0.10	7.61 ± 0.10
2020fqv	3.55 ± 0.20	<1.86	<2.85	<2.24	3.43 ± 0.48	6.31 ± 0.41	8.52 ± 0.23	4.53 ± 0.77	12.13 ± 0.64
2020mjm	2.72 ± 1.03	<2.75	<2.72	<2.75	3.56 ± 0.90	6.97 ± 0.90	9.76 ± 0.90	6.41 ± 0.90	9.66 ± 0.90
2020dpw	<2.58	<2.58	<4.12	<2.64	<9.76	6.22 ± 1.10	<9.76	5.00 ± 3.14	16.61 ± 0.96
2020acbm	4.22 ± 0.50	<2.40	<2.40	<2.39	7.16 ± 0.50	8.62 ± 0.61	14.18 ± 0.63	9.94 ± 0.86	7.81 ± 1.43
2021vaz	<0.06	<0.06	<0.07	<0.06	3.43 ± 0.39	10.41 ± 1.79	<15.03	5.25 ± 0.42	7.34 ± 0.41
2021ass	0.47 ± 0.62	<3.36	<3.36	<3.35	<2.40	2.41 ± 0.64	15.79 ± 0.63	6.91 ± 0.56	17.61 ± 0.68
2021gmj	3.33 ± 0.56	1.21 ± 0.50	1.31 ± 0.50	1.31 ± 0.50	2.06 ± 0.50	4.82 ± 0.71	10.42 ± 1.86	5.89 ± 0.50	11.71 ± 0.50
2021rhk	0.91 ± 1.03	<1.09	<1.10	<2.46	4.48 ± 1.00	6.26 ± 2.71	8.67 ± 1.02	7.43 ± 1.00	14.61 ± 1.26
2021uoy	<1.04	<2.12	<2.13	<2.12	<2.12	11.29 ± 1.17	...	9.00 ± 0.98	10.21 ± 0.98
2021yja	2.24 ± 0.12	2.07 ± 0.10	2.14 ± 0.10	2.05 ± 0.10	7.66 ± 0.28	8.23 ± 0.53	9.58 ± 1.94	8.36 ± 1.32	12.07 ± 4.54
2021adly	4.90 ± 1.09	<3.59	<3.60	<3.59	<3.59	10.81 ± 1.02	...	4.78 ± 1.00	16.11 ± 1.03
2021apg	2.62 ± 1.10	<1.98	<1.98	<1.97	2.89 ± 0.90	7.05 ± 2.17	8.51 ± 0.90	8.75 ± 0.93	16.59 ± 1.11
2021gvm	6.66 ± 0.47	<3.21	<2.19	4.34 ± 0.39	<6.70	6.70 ± 0.40	<6.70	8.74 ± 0.39	11.65 ± 0.42
2021ucg	2.78 ± 1.02	<4.24	<4.24	<5.23	5.99 ± 0.95	5.86 ± 1.97	14.87 ± 0.97	8.31 ± 0.95	16.92 ± 0.96
2022inn	0.94 ± 1.17	<1.25	<1.26	<2.54	<1.25	4.11 ± 1.10	...	6.02 ± 0.97	20.68 ± 2.14
2022fuc	3.15 ± 0.04	<0.43	0.94 ± 0.05	2.26 ± 0.04	4.16 ± 1.37	6.87 ± 0.35	7.56 ± 1.93	6.16 ± 0.17	16.57 ± 2.47
2022jzc	1.70 ± 0.96	<2.14	<2.15	<2.17	<2.17	3.51 ± 1.30	17.15 ± 5.32	3.91 ± 0.92	8.95 ± 0.91
2022ovb	3.42 ± 1.22	1.99 ± 0.96	2.06 ± 0.96	3.31 ± 0.96	5.50 ± 0.96	6.13 ± 0.96	...	9.67 ± 0.96	11.50 ± 0.96
2022frq	<1.95	<1.29	<1.30	<1.29	4.57 ± 0.46	5.10 ± 0.46	9.90 ± 1.10	5.86 ± 0.46	10.10 ± 0.70

Table A5
Gold/comparison-sample Peak Luminosity and Rise-time Distribution

Class	$L_{\text{avg}} [L_{\text{min}}, L_{\text{max}}]$ (erg s^{-1})	$L_{\text{avg}} [L_{\text{min}}, L_{\text{max}}]$ (days)	$M_{\text{avg}}^{\text{W2}} [M_{\text{min}}^{\text{W2}}, M_{\text{max}}^{\text{W2}}]$ (mag)	$M_{\text{avg}}^{\text{W2}} [M_{\text{min}}^{\text{W2}}, M_{\text{max}}^{\text{W2}}]$ (days)	$M_{\text{avg}}^r [M_{\text{min}}^r, M_{\text{max}}^r]$ (mag)	$M_{\text{avg}}^r [M_{\text{min}}^r, M_{\text{max}}^r]$ (days)
1	$3.1[0.83, 9.0] \times 10^{43}$	5.1[3.5, 10.0]	-19.8[-18.5, -21.4]	4.4[2.1, 8.0]	-18.4[-17.9, -19.4]	12.0[4.9, 26.4]
2	$2.2[0.77, 3.5] \times 10^{43}$	3.0[2.4, 3.6]	-19.2[-18.2, -19.9]	2.3[1.6, 2.9]	-18.2[-17.5, -18.6]	10.2[5.5, 13.6]
3	$2.2[0.23, 8.2] \times 10^{43}$	2.5[1.1, 3.8]	-19.1[-17.6, -21.6]	1.7[1.2, 2.5]	-18.1[-17.3, -19.3]	10.9[5.7, 18.1]
Comparison	$3.8[0.36, 17.9] \times 10^{42}$	2.4[0.1, 6.7]	-17.1[-13.9, -19.6]	2.2[0.1, 4.8]	-17.0[-14.5, -18.4]	12.9[6.5, 21.1]

Table A6
Gold/silver-sample Spectroscopic Properties

Name	t_{In} (days)	In Phase (days)	H I	He I	He II	C III	C IV	N III	N IV	V_{max}^a (10^4 km s^{-1})	M_{CDS}^b (M_{\odot})
PTF11iqb ¹	3.1 ± 1.0	1.6	Y	N	Y	N	Y	Y	N	1.1	0.005
2017ahn ¹	6.4 ± 0.3	2.1	Y	Y	Y	N	Y	Y	Y	0.9	0.04
2018zd ¹	7.7 ± 0.9	3.8	Y	N	Y	N	Y	Y	N	0.5	1.5
2019ust ¹	3.5 ± 0.6	1.7	Y	N	Y	N	Y	Y	...	1.0	0.02
2019qch ¹	11.4 ± 0.9	8.5	Y	Y ^c	Y	N	Y	Y
2020pni ¹	5.5 ± 1.0	1.5	Y	N	Y	Y	Y	Y	Y	1.0	0.01
2020sic ¹	2.4 ± 0.9	1.7	Y	N	Y	N	Y	Y	Y ^c
2020abtf ¹	4.5 ± 1.0	5.4	Y	N	Y	N	N	Y	N	0.6	4.2
2020abjq ¹	4.7 ± 1.0	2.9	Y	N	Y	N	Y	Y	Y	0.9	0.04
2020tlf ¹	7.7 ± 1.7	3.8	Y	Y	Y	Y	N	Y	N
2021wvd ¹	5.0 ± 0.6	1.9	Y	N	Y	N	N	Y	N
2021zj ¹	3.8 ± 1.1	4.7	Y	N	Y	N	N	Y	N	0.8	0.1
2021aek ¹	5.9 ± 1.4	2.5	Y	Y ^c	Y	N	N	Y	N	0.5	2.6
2021dbg ¹	4.3 ± 0.8	4.1	Y	N	Y	N	N	Y	N	1.3	<0.001
2021mqh ¹	3.5 ± 0.9	1.7	Y	N	Y	N	N	Y	N	0.8	0.1
2021tyw ¹	13.6 ± 1.3	8.7	Y	Y ^c	Y	Y ^c	Y ^c	Y	N	0.5	2.6
2021afkk ¹	8.3 ± 0.6	3.7	Y	Y ^c	Y	N	N	Y	N	0.8	0.1
2022ffg ¹	6.5 ± 0.7	2.2	Y	Y ^c	Y	Y ^c	Y	Y	Y ^c	0.85	0.05
2022pgf ¹	10.3 ± 1.0	1.3	Y	Y	Y	N	N	Y	N	0.9	0.04
2022prv ¹	20.8 ± 1.8	17.5	Y	Y	Y	N	N	Y	N
PTF10gva ²	1.6 ± 1.0	2.1	Y	N	Y	N	N	N	N	1.3	<0.001
PTF10aby ²	3.4 ± 0.7	2.7	Y	...	Y	...	Y ^c	N	...	0.85	0.05
2014G ²	3.5 ± 1.8	1.5	Y	N	Y	N	Y ^c	N	Y ^c	1.2	<0.001
2015bf ²	2.4 ± 1.3	2.2	Y	N	Y	N	Y	N	N	0.85	0.05
2016blz ²	5.5 ± 2.3	3.8	Y	N	Y	N	N	N	N
2018dfc ²	3.6 ± 1.0	2.3	Y	N	Y	N	Y	N	N
2021can ²	2.7 ± 0.6	1.2	Y	N	Y	N	Y ^c	N	Y ^c	0.9	0.04
2021ont ²	5.6 ± 1.1	5.0	Y	N	Y	N	Y ^c	N	N	0.65	0.4
2021qvr ²	3.2 ± 2.1	2.7	Y	N	Y	N	Y	N	N	1.2	<0.001
2021aaqn ²	0.7 ± 0.5	1.2	Y	N	Y	N	Y	N	N	1.1	0.005
2022dml ²	5.2 ± 1.6	4.6	Y	N	Y	N	N	N	N	0.9	0.04
2022jox ²	2.6 ± 1.4	1.1	Y	N	Y	N	Y	N	Y ^c	0.85	0.05
2013fs ³	1.4 ± 0.5	1.4	Y	N	Y	N	N	N	N	1.1	5.0×10^{-3}
2018fit ³	0.7 ± 0.5	1.1	Y	N	Y	N	N	N	N	1.2	< 10^{-3}
2020xua ³	2.9 ± 1.1	1.7	Y	N	Y	N	Y ^c	N	N	1.2	< 10^{-3}
2020nif ³	1.8 ± 1.2	2.1	Y	N	Y	N	N	N	N
2020fn ³	1.7 ± 0.6	2.2	Y	N	Y	N	N	N	N	1.1	5.0×10^{-3}
2021jtt ³	1.5 ± 0.3	1.2	Y	N	Y	N	Y ^c	N	N	1.1	5.0×10^{-3}
2022ibv ³	0.8 ± 0.6	2.5	Y	N	Y	N	N	N	N

Notes.^a Approximate maximum velocity measured in H α profile during phases of $\delta t = 50 \pm 10$ days.^b Calculated using trend in Dessart & Jacobson-Galán (2023).^c Marginal signal above continuum noise.

Table A7
Best-matched Model Parameters

Name	$\log_{10}(\dot{M})^a$ ($M_{\odot} \text{ yr}^{-1}$)	$\log_{10}(\rho_{14})^a$ (g cm^{-3})	$\log_{10}(\dot{M})^b$ ($M_{\odot} \text{ yr}^{-1}$)	$\log_{10}(\rho_{14})^b$ (g cm^{-3})	$\log_{10}(\dot{M})^c$ ($M_{\odot} \text{ yr}^{-1}$)	$\log_{10}(\rho_{14})^c$ (g cm^{-3})	$\log_{10}(\dot{M}[R_{\text{in}}])^d$ ($M_{\odot} \text{ yr}^{-1}(\text{cm})$)	$\log_{10}(D_{\ast})[R_{\text{CSM}}]^e$ ($\text{g cm}^{-1}(R_{\odot})$)	$\log_{10}(\rho_{14})^e$ (g cm^{-3})
PTF11iqb ¹	-2.0	-12.0	-2.0	-12.0	-2.0	-11.9	-3.0[14.5]	18.0[2700]	-10.0
2017ahn ¹	-2.0	-11.8	-2.0	-11.8	-1.3	-11.1	-2.4[14.2]	18.0[1500]	-10.0
	-1.0	-10.9							
2018zd ¹	-2.0	-11.8	-2.0	-11.8	-1.0	-10.9	-2.5[14.5]	18.0[2700]	-10.0
2019ust ¹	-2.0	-12.0	-2.0	-12.0	-2.0	-12.0	-3.0[14.2]	18.0[2700]	-10.0
	-1.5	-11.5							
2019qch ¹	-2.0	-12.0	-2.0	-12.0	-1.5	-11.5	-3.0[14.5]	18.0[2700]	-10.0
	-1.5	-11.5							
2020pni ¹	-2.0	-11.9	-2.0	-11.8	-2.0	-12.0	-3.0[14.2]	18.0[2500]	-10.0
	-1.5	-11.5							
2020sic ¹	-2.3	-12.3	-2.3	-12.3	-2.0	-12.0	-2.3[14.5]	18.0[2100]	-10.0
	-2.0	-11.9							
2020abtf ¹	-2.0	-11.9	-2.0	-11.9	-2.0	-12.0	-2.5[14.5]	17.9[2700]	-10.1
2020abjq ¹	-2.0	-11.9	-2.0	-11.9	-1.5	-11.5	-2.1[14.5]	18.0[2700]	-10.0
	-1.5	-11.5							
2020tlf ¹	-2.0	-12.0	-2.0	-12.0	-2.0	-12.0	-3.0[14.2]	18.0[2700]	-10.0
	-1.5	-11.5							
2021wvd ¹	-2.0	-11.9	-2.0	-11.8	-2.0	-11.9	-2.3[14.5]	18.0[2700]	-10.0
	-1.5	-11.5							
2021zj ¹	-2.0	-12.0	-2.0	-12.0	-1.0	-10.9	-2.5[14.5]	18.0[2100]	-10.0
	-1.5	-11.5							
2021aek ¹	-2.0	-11.8	-2.0	-11.8	-2.0	-12.0	-2.5[14.5]	18.0[2700]	-10.0
	-1.5	-11.5							
2021dbg ¹	-2.0	-11.9	-2.0	-11.9	-2.3	-12.3	-2.5[14.2]	18.0[2700]	-10.0
	-1.5	-11.5							
2021mqh ¹	-2.0	-12.0	-2.0	-12.0	-1.5	-11.5	-2.2[14.5]	18.0[2700]	-10.0
2021tyw ¹	-2.0	-12.0	-1.5	-11.5	-2.0	-12.0	-2.3[14.5]	18.0[2700]	-10.0
	-1.5	-11.5							
2021afkk ¹	-2.0	-12.0	-2.0	-12.0	-1.3	-12.0	-2.3[14.5]	17.7[2700]	-10.3
	-1.5	-11.5							
2022ffg ¹	-2.0	-12.0	-2.0	-11.8	-2.0	-12.0	-2.1[14.5]	18.0[2700]	-10.0
	-1.5	-11.5							
2022pgf ¹	-2.0 - 0.0	-12.0	-2.0	-12.0	-1.2	-11.5	-2.2[14.2]	18.0[2700]	-10.0
		-10.1							
2022prv ¹	-1.5 - 0.0	-11.5	-1.5	-11.5	-1.5	-11.5	-2.2[14.2]	16.9[1500]	-11.1
		-10.1							
PTF10abyy ²	-2.0	-12.0	-2.0	-12.0	-2.0	-12.0	-2.3[14.5]	18.0[2700]	-10.0
	-1.5	-11.5							
PTF10gva ²	-3.0	-13.3	-3.0	-13.3	-3.0	-13.3	-2.5[14.5]	18.0[2100]	-10.0
	-2.0	-12.0	-2.3	-12.3					
2014G ²	-2.0	-12.0	-2.0	-12.0	-2.3	-12.3	-2.5[14.2]	18.0[2700]	-10.0
2015bf ²	-3.0	-13.0	-3.0	-13.0	-2.0	-12.0	-2.5[14.2]	18.0[2700]	-10.0
	-2.0	-11.9	-2.0	-12.0					
2016blz ²	-2.0	-12.0	-2.0	-12.0	-2.0	-12.0	-2.5[14.2]	18.0[2700]	-10.0
	-1.5	-11.5		-12.0					
2018dfc ²	-2.0	-12.0	-2.0	-12.0	-2.1	-12.1	-2.7[14.2]	18.0[2700]	-10.0
	-1.5	-11.5							
2021can ²	-2.0	-12.0	-2.0	-12.0	-2.5	-12.3	-2.5[13.9]	17.7[2300]	-10.3
2021ont ²	-2.0	-12.0	-2.0	-11.8	-2.0	-12.0	-2.3[14.5]	18.0[2700]	-10.0
	-1.5	-11.5							
2021qvr ²	-3.0 - 0.0	-13.3	-3.0	-13.3	-2.1	-12.1	-2.7[14.2]	18.0[2500]	-10.0
		-10.1	-2.0	-11.9					
2022dml ²	-2.0	-11.9	-2.0	-11.9	-2.0	-12.0	-2.5[14.5]	18.0[2500]	-10.0
2022jox ²	-3.0	-13.0	-3.0	-13.0	-2.3	-12.3	-2.5[13.9]	18.0[2500]	-10.0
	-2.0	-11.9	-2.0	-12.0					
2013fs ³	-3.0	-13.3	-3.0	-13.3	-2.7	-12.7	-2.5[13.9]	18.0[1900]	-10.0
	-2.3	-12.3	-2.3	-12.3					
2018fif ³	-4.0 - -2.0	-14.3	-4.0 - -2.5	-14.3	-3.3	-13.3	-3.0[13.9]	18.0[2500]	-10.0
		-11.8		-12.3					
2020lfn ³	-3.0	-13.3	-3.0	-13.3	-3.0	-13.3	-3.0[13.9]	18.0[2700]	-10.0
	-2.0	-12.0	-2.3	-12.3					

Table A7
(Continued)

Name	$\log_{10}(\dot{M})^a$ ($M_{\odot} \text{ yr}^{-1}$)	$\log_{10}(\rho_{14})^a$ (g cm^{-3})	$\log_{10}(\dot{M})^b$ ($M_{\odot} \text{ yr}^{-1}$)	$\log_{10}(\rho_{14})^b$ (g cm^{-3})	$\log_{10}(\dot{M})^c$ ($M_{\odot} \text{ yr}^{-1}$)	$\log_{10}(\rho_{14})^c$ (g cm^{-3})	$\log_{10}(\dot{M}[R_{\text{in}}])^d$ ($M_{\odot} \text{ yr}^{-1}(\text{cm})$)	$\log_{10}(D_{*}[R_{\text{CSM}}])^e$ ($\text{g cm}^{-1}(R_{\odot})$)	$\log_{10}(\rho_{14})^e$ (g cm^{-3})
2020nif ³	-3.0 - -2.0	-13.3 - -12.0	-3.0 - -2.3	-13.3 - -12.3	-3.0	-13.3	-3.0[13.9]	18.0[2700]	-10.0
2020xua ³	-2.0	-12.0	-2.0	-12.0	-3.0	-13.3	-3.0[14.5]	18.0[2700]	-10.0
2021aaqn ³	-4.0 - -2.3	-14.3 - -12.3	-4.0 - -2.5	-14.3 - -12.3	-3.0	-13.3	-3.0[14.2]	18.0[2500]	-10.0
2021jtt ³	-3.0 - 0.0	-13.3 - -10.1	-3.0 - -2.3	-13.3 - -12.3	-3.0	-13.3	-2.5[14.5]	18.0[2700]	-10.0
2022ibv ³	-6.0 - -2.3	-15.0 - -12.3	-6.0 - -2.5	-15.0 - -12.3	-3.0	-13.3	-3.0[14.2]	17.7[2100]	-10.3
2013ft	<-2.3	<-12.3	<-2.5	<-12.3	-4.3	-13.6	...	16.9[1500]	-11.1
2013am	<-2.3	<-12.3	<-2.3	<-12.3	-5.3	-15.5	...	17.4[1500]	-10.6
2013ab	<-2.3	<-12.3	<-2.5	<-12.3	-6.0	-16.0	...	18.0[2100]	-10.0
2016X	<-2.0	<-12.0	<-2.3	<-12.3	-5.3	-15.5	...	17.7[2100]	-10.3
2016aqf	<-2.3	<-12.3	<-2.3	<-12.3	-6.0	-16.0	...	16.9[1500]	-11.1
2017eaw	<-2.0	<-12.0	<-2.3	<-12.3	-6.0	-16.0	...	18.0[2500]	-10.0
2017gmr	<-2.0	<-12.0	<-2.3	<-12.3	-6.0	-16.0	...	17.4[1500]	-10.6
2018lab	<-2.3	<-12.3	<-2.3	<-12.3	-4.3	-13.6	...	16.9[1500]	-11.1
2018kpo	<-2.3	<-12.3	<-2.5	<-12.3	-6.0	-16.0	...	18.0[2700]	-10.0
2018cuf	<-2.3	<-12.3	<-4.0	<-14.3	-6.0	-16.0	...	18.0[2100]	-10.0
2019edo	<-2.3	<-12.3	<-2.3	<-12.3	-4.3	-13.6	...	16.9[1700]	-11.1
2019nvm	<-2.0	<-12.0	<-2.3	<-12.3	-3.3	-13.3	...	18.0[2300]	-10.0
2019pjs	<-2.0	<-11.9	<-2.3	<-12.3	-6.0	-16.0	...	18.0[1500]	-10.0
2019enr	<-2.0	<-11.9	<-2.3	<-12.3	-6.0	-16.0	...	16.9[1500]	-11.1
2020ekk	<-2.0	<-11.9	<-2.3	<-12.3	-4.3	-13.6	...	18.0[2300]	-10.0
2020jfo	<-2.0	<-11.9	<-2.3	<-12.3	-4.3	-13.6	...	18.0[1700]	-10.0
2020fqv	<-2.3	<-12.3	<-2.5	<-12.3	-3.3	-13.1	...	16.9[1500]	-11.1
2020mjm	<-2.0	<-11.9	<-2.3	<-12.3	-4.3	-13.6	...	18.0[1500]	-10.0
2020dpw	<-2.0	<-11.8	<-2.3	<-12.3	-6.0	-16.0	...	16.9[1500]	-11.1
2020acbm	<-2.0	<-12.0	<-2.3	<-12.3	-4.3	-13.6	...	18.0[1900]	-10.0
2021vaz	<-2.3	<-12.3	<-4.0	<-14.3	-6.0	-16.0	...	16.9[1500]	-11.1
2021ass	<-2.0	<-11.9	<-2.3	<-12.3	-6.0	-16.0	...	17.3[1500]	-10.7
2021gmj	<-2.3	<-12.3	<-2.3	<-12.3	-6.0	-16.0	...	16.9[1900]	-11.1
2021rhk	<-2.0	<-11.9	<-2.3	<-12.3	-3.3	-13.3	...	18.0[1500]	-10.0
2021uoy	<-2.0	<-11.9	<-2.3	<-12.3	-4.3	-13.6	...	18.0[2300]	-10.0
2021yja	<-2.0	<-12.0	<-2.3	<-12.3	-4.3	-13.6	...	18.0[2300]	-10.0
2021adly	<-2.0	<-12.0	<-2.3	<-12.3	-4.3	-13.6	...	18.0[1900]	-10.0
2021apg	<-2.0	<-11.9	<-2.3	<-12.3	-4.3	-13.6	...	18.0[1500]	-10.0
2021gvm	<-2.0	<-11.9	<-2.3	<-12.3	-3.3	-13.3	...	18.0[1500]	-10.0
2021ucg	<-2.0	<-11.9	<-2.5	<-12.3	-6.0	-16.0	...	18.0[2300]	-10.0
2022inn	<-2.3	<-12.3	<-2.5	<-12.3	-6.0	-16.0	...	16.9[1500]	-11.1
2022fuc	<-2.3	<-12.3	<-4.0	<-14.3	-4.3	-13.6	...	16.9[1900]	-11.1
2022jzc	<-2.3	<-12.3	<-2.5	<-12.3	-6.0	-16.0	...	16.9[1500]	-11.1
2022ovb	<-2.3	<-12.3	<-2.3	<-12.3	-6.0	-16.0	...	18.0[2700]	-10.0
2022frq	<-2.3	<-12.3	<-2.3	<-12.3	-4.3	-13.6	...	18.0[2500]	-10.0

Notes.^a Calculated using multicolor photometry and t_{In} .^b Calculated using only t_{In} .^c Calculated using spectral comparison.^d Calculated using spectral models from Boian & Groh (2020).^e Calculated using multicolor models from Haynie & Piro (2021).

Table A8
Optical/NIR Spectroscopy

SN Name	UT Date	MJD	Phase ^a (days)	Telescope	Instrument	Wavelength Range (Å)	Data Source
2018cvn	2018-06-29T09:21:36	58298.4	5.1	SOAR	Goodman	4057–8021	Cartier
2018cvn	2018-12-22T02:38:24	58474.1	180.8	SOAR	Goodman	3833–7779	Cartier
2018cvn	2019-01-14T01:40:48	58497.1	203.8	SOAR	Goodman	3899–7765	Cartier
2018khh	2018-12-21T02:09:36	58473.1	2.6	SOAR	Goodman	3892–7760	Cartier
2018khh	2018-12-22T01:26:24	58474.1	3.6	SOAR	Goodman	3331–9000	Cartier

Note. Table A8 is published in its entirety in the electronic table.

^a Relative to first-light edition of the *Astrophysical Journal*.

(This table is available in its entirety in machine-readable form in the [online article](#).)

Appendix A

Host-galaxy Extinction Uncertainty

The host-galaxy extinction for sample objects is estimated by measuring the EW of the Na I D line and converting it to a host $E(B - V)$ using the relation derived by Stritzinger et al. (2018). We also test the relations between EW and host extinction from Poznanski et al. (2012) and find that, for the total sample, that relation returns average [min,max] $E(B - V)_{\text{host}}$ values of 2.3[0.014, 87.0] compared to 0.19[0.018, 0.81] when using Stritzinger et al. (2018). We choose to adopt the Stritzinger et al. (2018) relation given the large scatter associated with the Poznanski et al. (2012) relations (e.g., see Phillips et al. 2013) and inaccuracy of the latter at large EWs due to limited number of objects used in their fitting procedure. In Figure A2, we present the cumulative distributions of the host $E(B - V)$ values as well as the observed $g - r$ color versus Na I D EW. For the latter, we note that there is a large scatter relative to the Stritzinger et al. (2018) relation, i.e., gold/silver-sample objects are bluer than comparison-sample objects for similar E.W. Consequently, it appears that Na I D and/or colors are likely limited measures of reddening in SNe II, especially for large EWs and reddened colors. Additionally, in the top panel of Figure A3, we compare peak UV/optical magnitudes to the host extinction derived from Na I D for all subsamples. We note that there is clearly a lack of highly reddened objects in the sample (e.g., lower right panel of Figure A2). Also, there appears to be a correlation present in this host-extinction correction method that traces the reddening vector at larger reddening values (e.g., >0.3 mag) indicating inaccuracy in using Na I D as a tracer of reddening. Nonetheless, when looking at the distribution of peak UV magnitudes for objects without large host reddening, there remains a contrast in absolute magnitude between gold- and comparison-sample objects, most likely the result of CSM interaction. Furthermore, we note that using Na I D absorption as a probe of host extinction is dependent on the resolution of the spectrograph used to observe each SN in our sample. However, most of the spectra obtained for this study have resolutions of $R > 500$, which corresponds to $\Delta\lambda \lesssim 12$ Å for a combination of both the Na I D1 and D2 transitions. Reliable detections of this transition only become problematic with very low-resolution (e.g., $R < 100$, $\Delta\lambda > 60$ Å) spectrographs for the typical signal-to-noise ratio of our SN spectra.

In Figure A2, we compare our host reddening distribution to SN II samples from Anderson et al. (2014) and Irani et al. (2023), where the former derives host extinction from the Na I D EW using Poznanski et al. (2012), and the latter derives it using shock-cooling modeling. Overall, our host reddening distributions contain larger values than both the Anderson et al. (2014) and Irani et al. (2023) samples. We note that, for some objects that are in both our sample and that of Irani et al. (2023; e.g., SNe 2020pni, 2019nvm, 2018dfc, 2019ust), the derived host-galaxy $E(B - V)$ is larger by ~ 0.1 – 0.2 mag when using the Na I D EW. However, Irani et al. (2023) also fit for an R_V value while we apply a consistent $R_V = 3.1$ with a Fitzpatrick (1999) reddening law; the choice of both the R_V and the reddening law could lead to bias in the host-extinction correction.

We test whether the enhanced UV/optical luminosities observed in the gold sample are a product of the explosion and not uncertainty in the host extinction by first comparing the reddening vector for $R_V = 3.1$ in the Fitzpatrick (1999) reddening law to the $w_2 - v$ versus $g - r$ color evolution, as shown in Figure 5. The reddening vector has a slope of ~ 4.3 , which is inconsistent with a slope of ~ 8.1 measured in the color-color evolution of the gold and comparison samples. This implies that extinction correction alone is not able to make all of these SNe have the sample peak absolute magnitude. Additionally, we apply a synthetic host-extinction correction to the $g - r$ colors of the gold/comparison samples until the colors of each object are consistent with the bluest object in the sample at $\delta t = 5$ days, prior to any host reddening correction (e.g., see Figures 5 and A4). We find that an average of 0.21 mag of host reddening is needed, which translates to ~ 1.9 mag of UV extinction. However, even this amount of reddening cannot account for an average difference >3 mag observed between gold- and comparison-sample UV luminosities, further indicating that this observed phenomenon is not a result of host-galaxy extinction. Furthermore, even after this relative host reddening is applied based on colors, there remains a difference between the peak UV/optical luminosities of many comparison objects relative to those in the gold sample (e.g., see Figure A3).

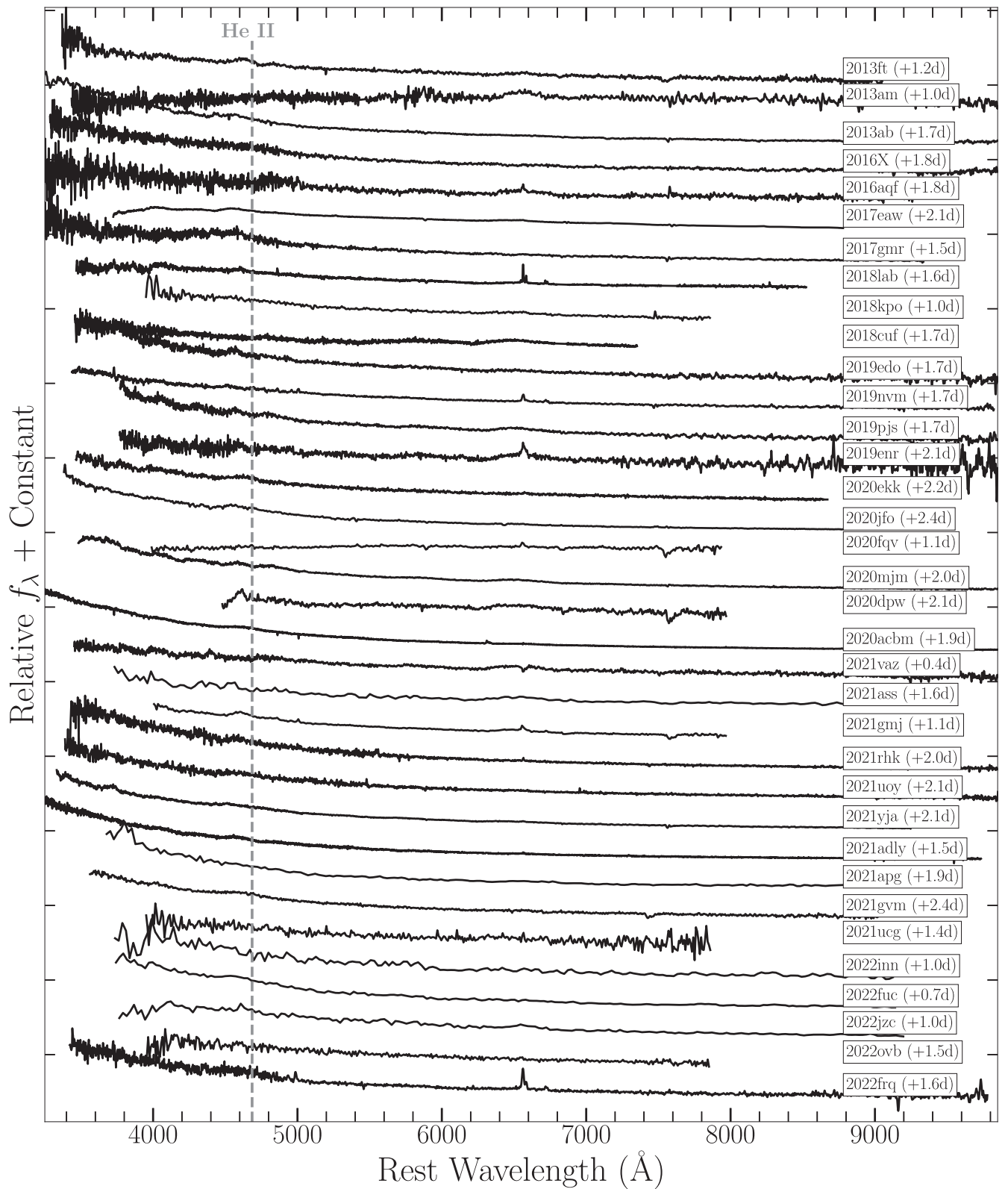


Figure A1. Comparison-sample spectra obtained at $t \lesssim 2$ day postfirst light. These SNe II do not show prominent spectroscopic evidence for CSM interaction but do have complete UV photometry for comparison to the gold-sample objects.

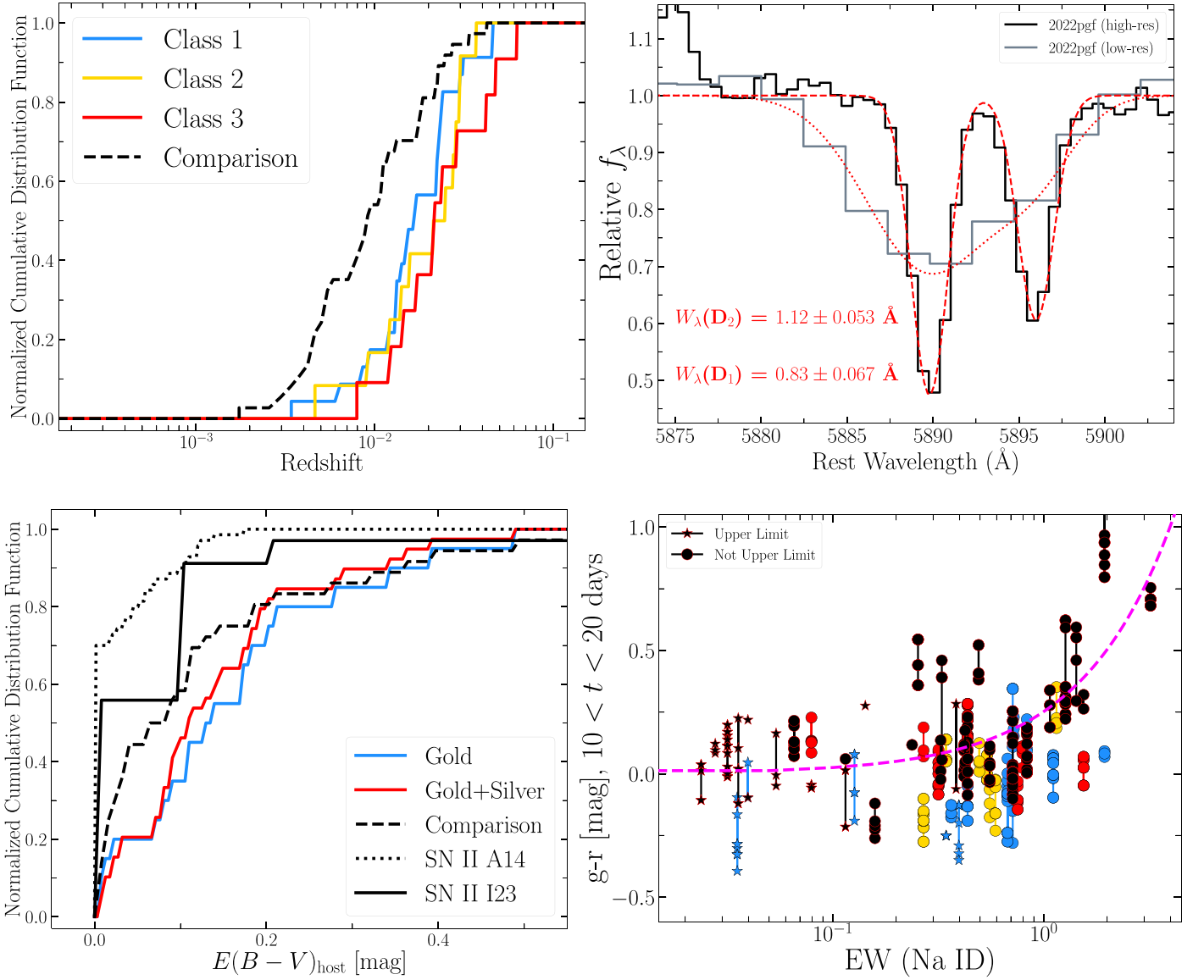


Figure A2. Top left: redshift distribution of gold/silver Class 1 (blue), 2 (yellow), 3 (red) sample compared to comparison sample (black dashed lines). Top right: visualization of host-galaxy extinction calculation using EWs of Na I D1 and D2 transitions and applying the relation from Stritzinger et al. (2018). Bottom left: Cumulative distribution of host-galaxy extinction for gold-, silver-, and comparison-sample objects. Host-galaxy extinction distribution from SN II sample by Anderson et al. (2014) shown as a black dotted line and by Irani et al. (2023) as a black solid line. Bottom right: Observed $g - r$ colors at $10 < \delta t < 20$ days vs. equivalent width of Na I D. Relation from Stritzinger et al. (2018) shown as dashed magenta line. Notably, gold-sample objects tend to reside below the reddening relation, implying that they are intrinsically bluer than the inferred host extinction.

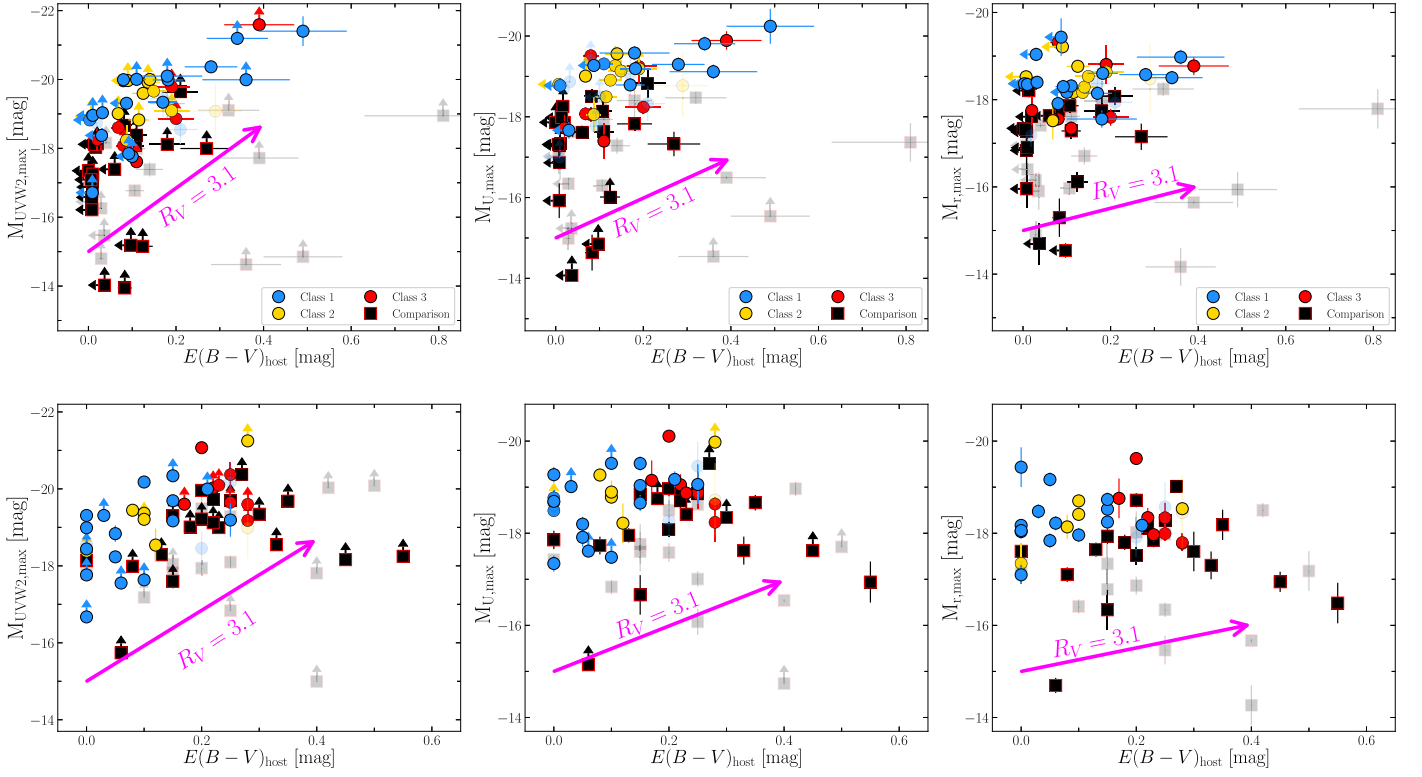


Figure A3. Top panel: Comparison of host-galaxy extinction vs. extinction-corrected peak $w2$ -, u -, and r -band absolute magnitudes for all of the sample objects. Host-extinction correction based on Na I D EW. Solid colored points represent the subsample of objects at $D > 40$ Mpc. We note that the highest luminosity objects ($M_{w2} < -21$ mag) also have some of the largest host-extinction values, suggesting that Na I D is a limited measure of host reddening. This is further supported by the lack of objects with similarly high luminosities at low $E(B - V)_{\text{host}}$ values. Bottom panel: peak $w2$ -, u -, and r -band absolute magnitudes vs. host-extinction correction using $g - r$ colors.

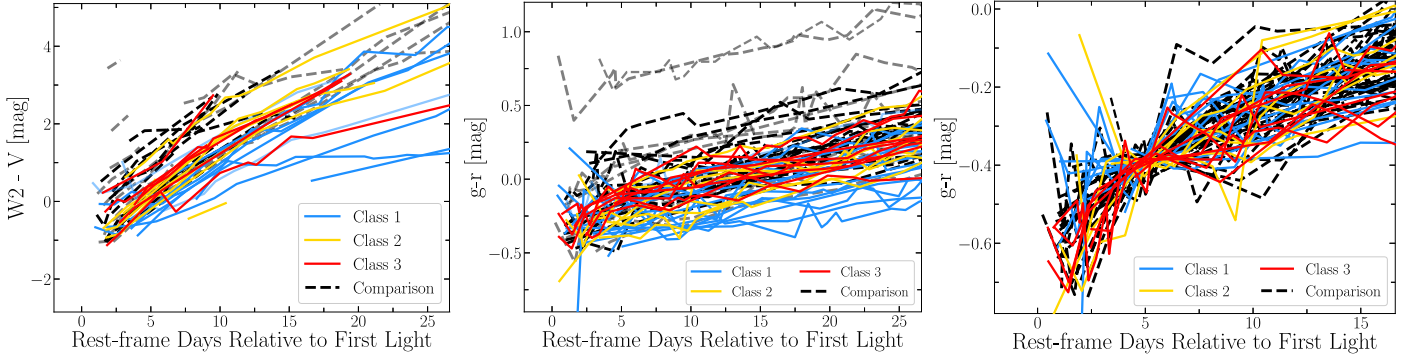


Figure A4. Observed $W2 - V$ (left) and $g - r$ (middle) colors before host-extinction correction is applied. The reddest objects are comparison-sample objects 2013am and 2020fqv. As discussed in Appendix A, host reddening is unlikely to cause the contrast observed between the gold and comparison samples. Class 1 objects remain the bluest objects for all phases, suggesting continued CSM interaction. Right: $g - r$ colors after applying synthetic host-extinction correction until all objects have the same color as the bluest object in the sample at $\delta t = 5$ days.

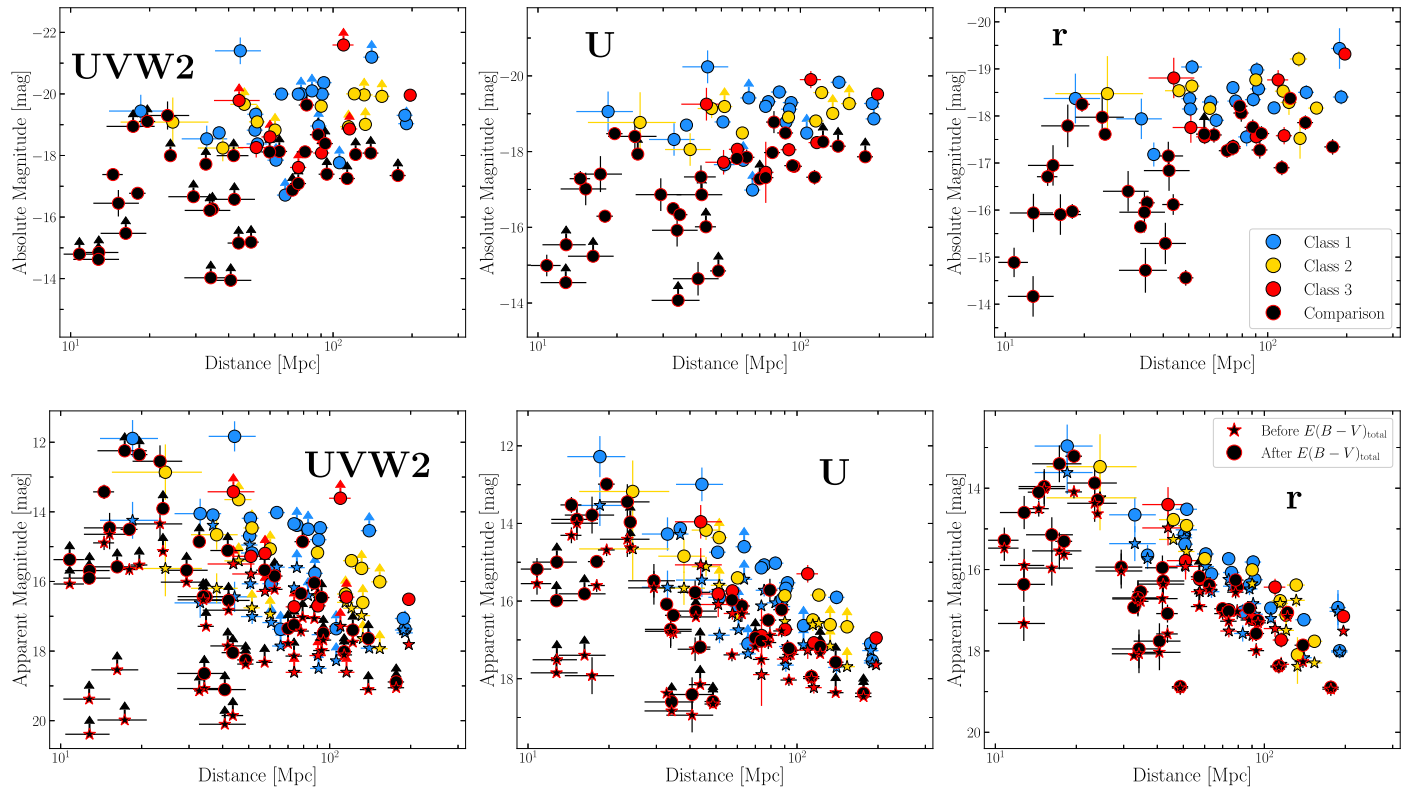


Figure A5. Top: Peak $w2$ - (left), u - (middle), and r -band (right) absolute magnitudes vs. distance for gold/silver (blue, yellow, red circles/stars) and comparison (black circles/stars) samples. Plotted stars (circles) represent peak magnitudes before (after) host extinction is applied using the Na I DEW. Bottom: peak $w2$ - (left), u - (middle), and r -band (right) apparent magnitude vs. distance.

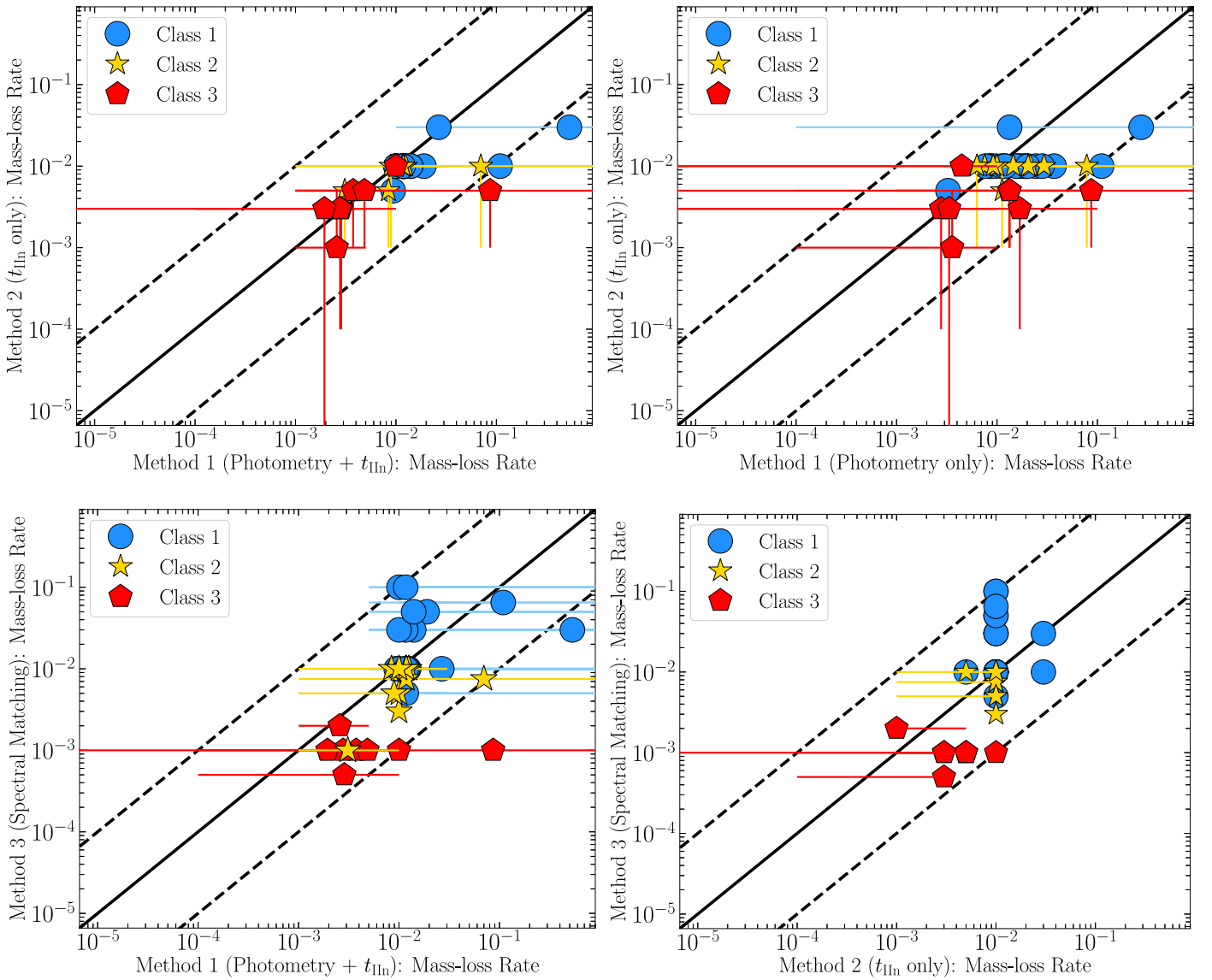



















Figure A6. Comparison of model-matching methods (Section 4.1). Top left: multicolor/bolometric light-curve properties plus t_{lin} vs. t_{lin} only. Top right: multicolor/bolometric light-curve properties vs. t_{lin} . Bottom left: multicolor/bolometric light-curve properties plus t_{lin} vs. direct spectral matching. Bottom right: t_{lin} vs. direct spectral matching. The plotted points represent the average mass-loss rates derived from each method, and the error bars represent the range of model parameters that are consistent with the observations (e.g., see Section 4.1).

ORCID iDs

W. V. Jacobson-Galán <https://orcid.org/0000-0003-1103-3409>
 L. Dessart <https://orcid.org/0000-0003-0599-8407>
 K. W. Davis <https://orcid.org/0000-0002-5680-4660>
 C. D. Kilpatrick <https://orcid.org/0000-0002-5740-7747>
 R. Margutti <https://orcid.org/0000-0003-4768-7586>
 R. J. Foley <https://orcid.org/0000-0002-2445-5275>
 R. Chornock <https://orcid.org/0000-0002-7706-5668>
 G. Terreran <https://orcid.org/0000-0003-0794-5982>
 D. Hiramatsu <https://orcid.org/0000-0002-1125-9187>
 M. Newsome <https://orcid.org/0000-0001-9570-0584>
 E. Padilla Gonzalez <https://orcid.org/0000-0003-0209-9246>
 C. Pellegrino <https://orcid.org/0000-0002-7472-1279>
 D. A. Howell <https://orcid.org/0000-0003-4253-656X>
 A. V. Filippenko <https://orcid.org/0000-0003-3460-0103>
 J. P. Anderson <https://orcid.org/0000-0003-0227-3451>
 C. R. Angus <https://orcid.org/0000-0002-4269-7999>
 K. Auchettl <https://orcid.org/0000-0002-4449-9152>

K. A. Bostroem <https://orcid.org/0000-0002-4924-444X>
 T. G. Brink <https://orcid.org/0000-0001-5955-2502>
 R. Cartier <https://orcid.org/0000-0003-4553-4033>
 D. A. Coulter <https://orcid.org/0000-0003-4263-2228>
 T. de Boer <https://orcid.org/0000-0001-5486-2747>
 M. R. Drouot <https://orcid.org/0000-0001-7081-0082>
 N. Earl <https://orcid.org/0000-0003-1714-7415>
 K. Ertini <https://orcid.org/0000-0001-7251-8368>
 J. R. Farah <https://orcid.org/0000-0003-4914-5625>
 D. Farias <https://orcid.org/0000-0002-6886-269X>
 C. Gall <https://orcid.org/0000-0002-8526-3963>
 H. Gao <https://orcid.org/0000-0003-1015-5367>
 A. Haynie <https://orcid.org/0000-0003-4287-4577>
 G. Hosseinzadeh <https://orcid.org/0000-0002-0832-2974>
 A. L. Ibbik <https://orcid.org/0000-0003-2405-2967>
 S. W. Jha <https://orcid.org/0000-0001-8738-6011>
 D. O. Jones <https://orcid.org/0000-0002-6230-0151>
 D. Langeroodi <https://orcid.org/0000-0001-5710-8395>
 N. LeBaron <https://orcid.org/0000-0002-2249-0595>

E. A. Magnier  <https://orcid.org/0000-0002-7965-2815>
 A. L. Piro  <https://orcid.org/0000-0001-6806-0673>
 S. I. Raimundo  <https://orcid.org/0000-0002-6248-398X>
 A. Rest  <https://orcid.org/0000-0002-4410-5387>
 S. Rest  <https://orcid.org/0000-0002-3825-0553>
 R. Michael Rich  <https://orcid.org/0000-0003-0427-8387>
 C. Rojas-Bravo  <https://orcid.org/0000-0002-7559-315X>
 H. Sears  <https://orcid.org/0000-0001-8023-4912>
 K. Taggart  <https://orcid.org/0000-0002-5748-4558>
 V. A. Villar  <https://orcid.org/0000-0002-5814-4061>
 R. J. Wainscoat  <https://orcid.org/0000-0002-1341-0952>
 X-F. Wang  <https://orcid.org/0000-0002-7334-2357>
 A. R. Wasserman  <https://orcid.org/0000-0002-4186-6164>
 S. Yan  <https://orcid.org/0009-0004-4256-1209>
 Y. Yang  <https://orcid.org/0000-0002-6535-8500>
 J. Zhang  <https://orcid.org/0000-0002-8296-2590>
 W. Zheng  <https://orcid.org/0000-0002-2636-6508>

References

- Ailawadhi, B., Dastidar, R., Misra, K., et al. 2023, *MNRAS*, 519, 248
 Anderson, J., Pessi, P., Galbany, L., et al. 2020, *TNSAN*, 244, 1
 Anderson, J. P., González-Gaitán, S., Hamuy, M., et al. 2014, *ApJ*, 786, 67
 Andrews, J. E., Sand, D. J., Valenti, S., et al. 2019, *ApJ*, 885, 43
 Andrews, J. E., Pearson, J., Hosseinzadeh, G., et al. 2024, *ApJ*, 965, 85
 Angus, C., Rojas-Bravo, C., DeMarchi, L., & Jacobson-Galan, W. 2021, *TNSCR*, 2021-1233, 1
 Beasar, E. R., Davies, B., Smith, N., et al. 2020, *MNRAS*, 492, 5994
 Becker, A. 2015, HOTPANTS: High Order Transform of PSF ANd Template Subtraction, Astrophysics Source Code Library, ascl:1504.004
 Bellm, E. C., Kulkarni, S. R., Graham, M. J., et al. 2019, *PASP*, 131, 018002
 Berger, E., Keating, G. K., Margutti, R., et al. 2023, *ApJL*, 951, L31
 Boian, I., & Groh, J. H. 2020, *MNRAS*, 496, 1325
 Bose, S., Valenti, S., Misra, K., et al. 2015, *MNRAS*, 450, 2373
 Bostroem, K. A., Pearson, J., Shrestha, M., et al. 2023, arXiv:2306.10119
 Brethauer, D., Margutti, R., Milisavljevic, D., et al. 2022, *ApJ*, 939, 105
 Brown, P. J., Breeveld, A. A., Holland, S., Kuin, P., & Pritchard, T. 2014, *Ap&SS*, 354, 89
 Brown, P. J., Roming, P. W. A., Milne, P., et al. 2010, *ApJ*, 721, 1608
 Brown, T. M., Baliber, N., Bianco, F. B., et al. 2013, *PASP*, 125, 1031
 Bruch, R. 2021, *TNSCR*, 2021-407, 1
 Bruch, R., Schulze, S., Yaron, O., et al. 2019, *TNSCR*, 2019-2378, 1
 Bruch, R., Sollerman, J., Zimmerman, E., et al. 2022, *TNSCR*, 2022-1323, 1
 Bruch, R., Strotjohann, N., Gal-Yam, A., et al. 2021a, *TNSAN*, 200, 1
 Bruch, R. J., Gal-Yam, A., Schulze, S., et al. 2021b, *ApJ*, 912, 46
 Bruch, R. J., Gal-Yam, A., Yaron, O., et al. 2023, *ApJ*, 952, 119
 Burke, J., Hiramatsu, D., Howell, D. A., et al. 2020, *TNSCR*, 2020-3650, 1
 Burke, J., Hiramatsu, D., Howell, D. A., McCully, C., & Pellegrino, C. 2019, *TNSCR*, 2019-1748, 1
 Burke, J., Li, W., Howell, D. A., et al. 2022, *TNSCR*, 2022-567, 1
 Buzzoni, B., Delabre, B., Dekker, H., et al. 1984, *Msngr*, 38, 9
 Callis, E., Fraser, M., Pastorello, A., et al. 2021, arXiv:2109.12943
 Chambers, K. C., Huber, M. E., Flewelling, H., et al. 2017, *TNSCR*, 2017-324, 1
 Chandra, P., Chevalier, R. A., Maeda, K., Ray, A. K., & Nayana, A. J. 2024, *ApJL*, 963, L4
 Chevalier, R. A. 1998, *ApJ*, 499, 810
 Chevalier, R. A., & Fransson, C. 1994, *ApJ*, 420, 268
 Chevalier, R. A., & Fransson, C. 2017, in *Handbook of Supernovae*, ed. A. W. Alsabti & P. Murdin (Berlin: Springer), 875
 Chevalier, R. A., Fransson, C., & Nymark, T. K. 2006, *ApJ*, 641, 1029
 Chevalier, R. A., & Irwin, C. M. 2011, *ApJL*, 729, L6
 Chevalier, R. A., & Irwin, C. M. 2012, *ApJL*, 747, L17
 Chugai, N. N. 2001, *MNRAS*, 326, 1448
 Chugai, N. N. 2022, *AstL*, 48, 163
 Clemens, J. C., Crain, J. A., & Anderson, R. 2004, *Proc. SPIE*, 5492, 331
 Coulter, D. A., Jones, D. O., McGill, P., et al. 2022, YSE-PZ: An Open-source Target and Observation Management System, v0.3.0, Zenodo doi:10.5281/zenodo.7278430
 Coulter, D. A., Jones, D. O., McGill, P., et al. 2023, *PASP*, 135, 064501
 Dahiwal, A., & Fremling, C. 2021, *TNSCR*, 2021-223, 1
 Davies, B., & Dessart, L. 2019, *MNRAS*, 483, 887
 Davis, K. W., Taggart, K., Tinyanont, S., et al. 2023, *MNRAS*, 523, 2530
 Deckers, M., Burgaz, U., Dimitriadis, G., et al. 2022, *TNSCR*, 2022-1986, 1
 Delgado, M., González, R., Muñoz, S., et al. 2021a, *TNSAN*, 206, 1
 Delgado, M., Galbany, L., González, R., et al. 2021b, *TNSAN*, 21, 1
 DeMarchi, L., Margutti, R., Dittman, J., et al. 2022, *ApJ*, 938, 84
 Dessart, L., Audit, E., & Hillier, D. J. 2015, *MNRAS*, 449, 4304
 Dessart, L., Gutiérrez, C. P., Kuncarayakti, H., Fox, O. D., & Filippenko, A. V. 2023, *A&A*, 675, A33
 Dessart, L., Hillier, D. J., Audit, E., Livne, E., & Waldman, R. 2016, *MNRAS*, 458, 2094
 Dessart, L., Hillier, D. J., Gezari, S., Basa, S., & Matheson, T. 2009, *MNRAS*, 394, 21
 Dessart, L., Hillier, D. J., Waldman, R., & Livne, E. 2013, *MNRAS*, 433, 1745
 Dessart, L., & Jacobson-Galán, W. V. 2023, *A&A*, 677, A105
 Dessart, L., John Hillier, D., & Audit, E. 2017, *A&A*, 605, A83
 Dong, Y., Valenti, S., Bostroem, K. A., et al. 2021, *ApJ*, 906, 56
 Fabricant, D., Fata, R., Epps, H., et al. 2019, *PASP*, 131, 075004
 Fan, Y.-F., Bai, J.-M., Zhang, J.-J., et al. 2015, *RAA*, 15, 918
 Fassia, A., Meikle, W. P. S., Vacca, W. D., et al. 2000, *MNRAS*, 318, 1093
 Filippenko, A. V. 1982, *PASP*, 94, 715
 Finkbeiner, D. P., Schlafly, E. F., Schlegel, D. J., et al. 2016, *ApJ*, 822, 66
 Fitzpatrick, E. L. 1999, *PASP*, 111, 63
 Flewelling, H. A., Magnier, E. A., Chambers, K. C., et al. 2020, *ApJS*, 251, 7
 Fransson, C., Ergon, M., Challis, P. J., et al. 2014, *ApJ*, 797, 118
 Fransson, C., Lundqvist, P., & Chevalier, R. A. 1996, *ApJ*, 461, 993
 Fremling, C., Dahiwal, A., & Dugas, A. 2019, *TNSCR*, 2019-1923, 1
 Gal-Yam, A., Arcavi, I., Ofek, E. O., et al. 2014, *Natur*, 509, 471
 Gall, C., Hjorth, J., Watson, D., et al. 2014, *Natur*, 511, 326
 Gehrels, N., Chincarini, G., Giommi, P., et al. 2004, *ApJ*, 611, 1005
 Goldberg, J. A., Jiang, Y.-F., & Bildsten, L. 2022, *ApJ*, 933, 164
 González, M., Audit, E., & Huynh, P. 2007, *A&A*, 464, 429
 Graham, M. J., Kulkarni, S. R., Bellm, E. C., et al. 2019, *PASP*, 131, 078001
 Grefenstette, B. W., Brightman, M., Earnshaw, H. P., Harrison, F. A., & Margutti, R. 2023, *ApJL*, 952, L3
 Haynie, A., & Piro, A. L. 2021, *ApJ*, 910, 128
 Hillier, D. J., & Dessart, L. 2012, *MNRAS*, 424, 252
 Hillier, D. J., & Dessart, L. 2019, *A&A*, 631, A8
 Hiramatsu, D., Arcavi, I., Zimmerman, E., et al. 2020b, *TNSCR*, 2020-1922, 1
 Hiramatsu, D., Arcavi, I., Burke, J., et al. 2019, *TNSCR*, 2019-1557, 1
 Hiramatsu, D., Burke, J., Arcavi, I., et al. 2020a, *TNSCR*, 2020-1789, 1
 Hiramatsu, D., Howell, D. A., Van Dyk, S. D., et al. 2021, *NatAs*, 5, 903
 Hiramatsu, D., Tsuna, D., Berger, E., et al. 2023, *ApJL*, 955, L8
 Horne, K. 1986, *PASP*, 98, 609
 Hosseinzadeh, G., Farah, J., Shrestha, M., et al. 2023, *ApJL*, 953, L16
 Hosseinzadeh, G., Kilpatrick, C. D., Dong, Y., et al. 2022, *ApJ*, 935, 31
 Hosseinzadeh, G., Valenti, S., McCully, C., et al. 2018, *ApJ*, 861, 63
 Huang, C., & Chevalier, R. A. 2018, *MNRAS*, 475, 1261
 Huang, F., Wang, X. F., Hosseinzadeh, G., et al. 2018, *MNRAS*, 475, 3959
 Irani, I., Morag, J., Gal-Yam, A., et al. 2023, arXiv:2310.16885
 Irani, I., Zimmerman, E., Nordin, J., et al. 2022, *TNSCR*, 2022-1107, 1
 Izzo, L., Angus, C., Hjorth, J., & Gall, C. 2020, *TNSCR*, 2020-1621, 1
 Jacobson-Galán, W. V., Dessart, L., Jones, D. O., et al. 2022, *ApJ*, 924, 15
 Jacobson-Galán, W. V., Dessart, L., Margutti, R., et al. 2023, *ApJL*, 954, L42
 Jacobson-Galán, W. V., Margutti, R., Kilpatrick, C. D., et al. 2020, *ApJ*, 898, 166
 Jencson, J. E., Kasliwal, M. M., Adams, S. M., et al. 2019, *ApJ*, 886, 40
 Johansson, J., Magee, M., Bar, I., & Yaron, O. 2016, *TNSCR*, 2016-283, 1
 Jones, D. O., Foley, R. J., Narayan, G., et al. 2021, *ApJ*, 908, 143
 Kaiser, N., Aussel, H., Burke, B. E., et al. 2002, *Proc. SPIE*, 4836, 154
 Kawabata, M. 2020, *TNSCR*, 2020-657, 1
 Khazov, D., Yaron, O., Gal-Yam, A., et al. 2016, *ApJ*, 818, 3
 Kilpatrick, C. D., & Foley, R. J. 2018, *MNRAS*, 481, 2536
 Kilpatrick, C. D., Izzo, L., Bentley, R. O., et al. 2023, *MNRAS*, 524, 2161
 Kochanek, C. S., Fraser, M., Adams, S. M., et al. 2017, *MNRAS*, 467, 3347
 Kozyreva, A., Klencki, J., Filippenko, A. V., et al. 2022, *ApJL*, 934, L31
 Kravtsov, T., Gutiérrez, C., Williams, S. C., et al. 2021, *TNSAN*, 100, 1
 Leonard, D. C., Filippenko, A. V., Barth, A. J., & Matheson, T. 2000, *ApJ*, 536, 239
 Lin, H., Wang, X., Zhang, J., et al. 2021, *MNRAS*, 505, 4890
 Lundqvist, P., & Fransson, C. 1996, *ApJ*, 464, 924
 Magnier, E. A., Schlafly, E. F., Finkbeiner, D. P., et al. 2020, *ApJS*, 251, 6
 Margutti, R., Kamble, A., Milisavljevic, D., et al. 2017, *ApJ*, 835, 140
 Masci, F. J., Laher, R. R., Rusholme, B., et al. 2019, *PASP*, 131, 018003
 Matthews, D., Margutti, R., Alexander, K. D., et al. 2023, *TNSAN*, 146, 1
 McCully, C., Volgenau, N. H., Harbeck, D.-R., et al. 2018, *Proc. SPIE*, 10707, 107070K
 Meza Retamal, N., Dong, Y., Bostroem, K. A., et al. 2024, arXiv:2401.04027

- Milisavljevic, D., Margutti, R., Kamble, A., et al. 2015, *ApJ*, **815**, 120
- Miller, J. S., & Stone, R. P. S. 1993, The Kast Double Spectrograph, Lick Observatory Technical Reports 66, Univ. of California, <https://mthamilton.ucolick.org/techdocs/instruments/kast/Tech%20Report%2066%20KAST%20Miller%20Stone.pdf>
- Morozova, V., Ott, C. D., & Piro, A. L. 2015, SNEC: SuperNova Explosion Code, Astrophysics Source Code Library, ascl:1505.033
- Morozova, V., Piro, A. L., & Valenti, S. 2017, *ApJ*, **838**, 28
- Morozova, V., Piro, A. L., & Valenti, S. 2018, *ApJ*, **858**, 15
- Müller-Bravo, T. E., Gutiérrez, C. P., Sullivan, M., et al. 2020, *MNRAS*, **497**, 361
- Murai, Y., Tanaka, M., Kawabata, M., et al. 2024, *MNRAS*, **528**, 4209
- Nakaoka, T., Kawabata, K. S., Maeda, K., et al. 2018, *ApJ*, **859**, 78
- Newsome, M., Burke, J., Howell, D. A., et al. 2022, TNSCR, **2022-902**, 1
- Newsome, M., Gonzalez, E. P., Burke, J., et al. 2021, TNSCR, **2021-2711**, 1
- Niemela, V. S., Ruiz, M. T., & Phillips, M. M. 1985, *ApJ*, **289**, 52
- Oke, J. B., Cohen, J. G., Carr, M., et al. 1995, *PASP*, **107**, 375
- Panjkov, S., Auchettl, K., Shappee, B. J., et al. 2023, arXiv:2308.13101
- Pastorello, A., Benetti, S., Brown, P. J., et al. 2015, *MNRAS*, **449**, 1921
- Pearson, J., Hosseinzadeh, G., Sand, D. J., et al. 2023, *ApJ*, **945**, 107
- Pellegrino, C., Hiramatsu, D., Burke, J., et al. 2021, TNSCR, **2021-2178**, 1
- Pellegrino, C., Howell, D. A., Burke, J., et al. 2022, TNSCR, **2022-808**, 1
- Perley, D. 2019, TNSCR, **2019-713**, 1
- Pessi, P., Anderson, J., Gutierrez, C., et al. 2020, TNSAN, **256**, 1
- Phillips, M. M., Simon, J. D., Morrell, N., et al. 2013, *ApJ*, **779**, 38
- Poznanski, D., Prochaska, J. X., & Bloom, J. S. 2012, *MNRAS*, **426**, 1465
- Prentice, S., Smartt, S., & Maguire, K. 2018, TNSCR, **2018-1985**, 1
- Rayner, J. T., Toomey, D. W., Onaka, P. M., et al. 2003, *PASP*, **115**, 362
- Rest, A., Stubbs, C., Becker, A. C., et al. 2005, *ApJ*, **634**, 1103
- Ricker, G. R., Winn, J. N., Vanderspek, R., et al. 2015, *JATIS*, **1**, 014003
- Ridden-Harper, R., Rest, A., Hounsell, R., et al. 2021, arXiv:2111.15006
- Rojas-Bravo, C., Taggart, K., & Foley, R. J. 2021, TNSCR, **2021-2290**, 1
- Roming, P. W. A., Kennedy, T. E., Mason, K. O., et al. 2005, *SSRv*, **120**, 95
- Schechter, P. L., Mateo, M., & Saha, A. 1993, *PASP*, **105**, 1342
- Schulze, S., Sollerman, J., Perley, D. A., & Zimmerman, E. 2020, TNSAN, **170**, 1
- Shahbandeh, M., Sarangi, A., Temim, T., et al. 2023, *MNRAS*, **523**, 6048
- Shivvers, I., Groh, J. H., Mauerhan, J. C., et al. 2015, *ApJ*, **806**, 213
- Siebert, M. R., & Jacobson-Galan, R. J. F. W. 2022, ATel, **15345**, 1
- Smartt, S. J., Valenti, S., Fraser, M., et al. 2015, *A&A*, **579**, A40
- Smith, K. W., Fulton, M., Gillanders, J., et al. 2021a, TNSAN, **14**, 1
- Smith, K. W., Fulton, M., Gillanders, J., et al. 2021b, TNSAN, **18**, 1
- Smith, K. W., Smartt, S. J., Young, D. R., et al. 2020, arXiv:2003.09052
- Smith, N., Mauerhan, J. C., Cenko, S. B., et al. 2015, *MNRAS*, **449**, 1876
- Smith, N., Pearson, J., Sand, D. J., et al. 2023, arXiv:2306.07964
- Smith, N., Silverman, J. M., Chornock, R., et al. 2009, *ApJ*, **695**, 1334
- Sollerman, J., Yang, S., Schulze, S., et al. 2021, *A&A*, **655**, A105
- Soumagnac, M. T., Ganot, N., Irani, I., et al. 2020, *ApJ*, **902**, 6
- Srivastav, S., Smartt, S. J., Fulton, M., et al. 2021, TNSCR, **2021-2568**, 1
- Stritzinger, M. D., Taddia, F., Burns, C. R., et al. 2018, *A&A*, **609**, A135
- Stroh, M. C., Terreran, G., Coppejans, D. L., et al. 2021, *ApJL*, **923**, L24
- Subrayan, B. M., Milisavljevic, D., Moriya, T. J., et al. 2023, *ApJ*, **945**, 46
- Szalai, T., Vinkó, J., Könyves-Tóth, R., et al. 2019, *ApJ*, **876**, 19
- Taddia, F., Stritzinger, M. D., Sollerman, J., et al. 2013, *A&A*, **555**, A10
- Taggart, K., Couch, C. D., Tinyanont, S., Foley, R. J., & Jacobson-Galán, W. 2021a, TNSCR, **2021-2671**, 1
- Taggart, K., Tinyanont, S., Davis, K., & Foley, R. 2022, TNSCR, **2022-2130**, 1
- Taggart, K., Tinyanont, S., Foley, R. J., & Gagliano, A. 2021b, ATel, **14959**, 1
- Tartaglia, L., Sand, D. J., Groh, J. H., et al. 2021, *ApJ*, **907**, 52
- Teja, R. S., Singh, A., Sahu, D. K., et al. 2022, *ApJ*, **930**, 34
- Terreran, G., Jacobson-Galan, W., & Blanchard, P. K. 2020, ATel, **14115**, 1
- Terreran, G., Jacobson-Galán, W. V., Groh, J. H., et al. 2022, *ApJ*, **926**, 20
- Terreran, G., Jerkstrand, A., Benetti, S., et al. 2016, *MNRAS*, **462**, 137
- Terwel, J., Deckers, M., Dimitriadis, G., et al. 2021, TNSAN, **227**, 1
- Tinyanont, S., Taggart, K., Davis, K., & Foley, R. 2021a, TNSCR, **2021-3791**, 1
- Tinyanont, S., Taggart, K., & Foley, R. J. 2021b, TNSCR, **2021-1720**, 1
- Tinyanont, S., Ridden-Harper, R., Foley, R. J., et al. 2022, *MNRAS*, **512**, 2777
- Tody, D. 1986, *Proc. SPIE*, **627**, 733
- Tody, D. 1993, in ASP Conf. Ser. 52, Astronomical Data Analysis Software and Systems II, ed. R. J. Hanisch, R. J. V. Brissenden, & J. Barnes (San Francisco, CA: ASP), 173
- Tomasella, L., Cappellaro, E., Pumo, M. L., et al. 2018, *MNRAS*, **475**, 1937
- Tonry, J. L., Denneau, L., Flewelling, H., et al. 2018b, *ApJ*, **867**, 105
- Tonry, J. L., Denneau, L., Heinze, A. N., et al. 2018a, *PASP*, **130**, 064505
- Tsvetkov, D. Y., Belinsky, A. A., Ikonnikova, N. P., et al. 2022, *AstL*, **48**, 209
- Tucker, M. A. 2022, TNSCR, **2022-2083**, 1
- Utrobin, V. P., Chugai, N. N., Andrews, J. E., et al. 2021, *MNRAS*, **505**, 116
- Valenti, S., Sand, D., Pastorello, A., et al. 2014, *MNRAS*, **438**, L101
- Vasylyev, S. S., Filippenko, A. V., Vogl, C., et al. 2022, *ApJ*, **934**, 134
- Vasylyev, S. S., Yang, Y., Filippenko, A. V., et al. 2023, *ApJL*, **955**, L37
- Vaytet, N. M. H., Audit, E., Dubroca, B., & Delahaye, F. 2011, *JQSRT*, **112**, 1323
- Wang, Q., Goel, A., Dessart, L., et al. 2024, *MNRAS*, **530**, 3906
- Waters, C. Z., Magnier, E. A., Price, P. A., et al. 2020, *ApJS*, **251**, 4
- Waxman, E., & Katz, B. 2017, in Handbook of Supernovae, ed. A. W. Alsabti & P. Murdin (Berlin: Springer), 967
- Weiler, K. W., Panagia, N., Montes, M. J., & Sramek, R. A. 2002, *ARA&A*, **40**, 387
- Wellons, S., Soderberg, A. M., & Chevalier, R. A. 2012, *ApJ*, **752**, 17
- Yaron, O., Perley, D. A., Gal-Yam, A., et al. 2017, *NatPh*, **13**, 510
- Zhang, J., Zhai, Q., & Wang, X. 2021a, ATel, **14398**, 1
- Zhang, J., Zhai, Q., & Wang, X. 2021b, ATel, **15070**, 1
- Zhang, J., & Wang, X. 2020, TNSCR, **2020-788**, 1
- Zhang, J., Wang, X., Mazzali, P. A., et al. 2014, *ApJ*, **797**, 5
- Zhang, J., Wang, X., József, V., et al. 2020, *MNRAS*, **498**, 84
- Zimmerman, E., Sollerman, J., Schulze, S., et al. 2022, TNSCR, **2022-874**, 1
- Zimmerman, E. A., Irani, I., Chen, P., et al. 2024, *Natur*, **627**, 759